Imperial College
London

Characterisation of semi-solid deformation behaviour of aluminium-copper alloys via combined x-ray microtomography and finite element modelling

Devashish Fuloria

Department of Materials

Imperial College London

A thesis submitted for the degree of

Doctor of Philosophy

January 2009

I would like to dedicate this thesis to my loving grandparents.

Acknowledgements

I gratefully acknowledge the provision of funding for the research described in this dissertation by the Engineering and Physical Sciences Research Council (EPSRC) and ALCOA, especially the people at ALCOA including Joanne Murray, Jaako Sunni, Wei Wang and Weiland Hasso.

I would particularly like to thank my supervisor, Prof. Peter Lee for his guidance and encouragement throughout my research, and for ensuring that the RSM 101 is a friendly and enjoyable place to work. Special thanks to Peter Rockett for his tremendous help during the development of infrared heating and grip design on the tensile/compression rig for *in situ* x-ray radiography. Special thanks to Richard Hamilton for making sure that the Phoenix and everything else in LG56 was always running.

The labmates at RSM101 deserve a special mention for ensuring that the time spent as a PhD always remained enjoyable. Dylan Ness for losing a million snooker games on a trot, Magnus Lekstrom for never being able to say NO, Pavel Ramirez Lopez, Lang Yuan and Stefano Angioletti-Uberti for conspiring to kill me with an overdose of alcohol, Farid Tariq and Alessandro Mottura for bringing up interesting discussions about world politics. Not to forget, a big thanks to Dr. Ludovic Thuinet, Junsheng Wang, Randhir Singh, Dr. Judith Roether, Dr. Muthiah Ganesan, Dr. Robert Atwood, Dr. Andre Phillion and Gowsh.

The London experience was further enriched with the time spent with Mattia Gazzola and Theodorous Koundorellis, my flatmates at Clayponds who have since been the closest friends. A special thanks to

Sharad Prakash for opening my eyes to the financial world which have helped me appreciate the present mess.

The completion of the work has not only been a test of patience for me, but also for my family who have always supported and encouraged my efforts. Lastly, a special thanks to Swati who has always been there with me in good times and more importantly, in tough times.

Abstract

The production of aluminium sheet is expensive and energy intensive despite the reduced environmental impact during use. Twin roll casting is a method of directly producing aluminium alloys in near net shape directly to sheet at a fraction of the energy costs of conventional DC casting / hot rolling. It also requires a fraction of the capital cost. Although sheet can be produced, defects (segregates, surface bleeds, buckling, etc.) can arise which limit the range of alloys which can be cast. This project aims to elucidate the complex mechanisms causing these defects through a combined experimental and computational study of semi-solid deformation in aluminium alloys.

Columnar dendritic structures were generated for Al-Cu alloys through directional solidification experiments and quantified in three dimensions (3D) using x-ray microtomography (XMT). The α-Al and the Cu-rich interdendritic liquid were segmented using image analysis. These 3D datasets were exported as meshes to be used in control volume and finite element codes. Firstly, the flow between the dendrites was simulated by solving the Stokes equation and permeability tensor was calculated as a function of the fraction solid. The size of representative volume element was estimated to be 4-6 times the characteristic length scale in the microstructure. Secondly, finite element simulations were performed on 3D columnar dendritic structures to estimate their mechanical properties and derive constitutive behaviour as a function of temperature, strain-rate and fraction solid. Temperature and strain-rate dependent compression tests were performed in the Gleeble on alloys with dendritic composition to determine the

mechanical properties of the monolithic Al-dendrites. The fraction solid dependency term in the constitutive equation was determined as a purely geometric factor which could be easily replicated in other alloys systems. Lastly, hot tearing was directly observed in an Al-12 wt.%Cu alloy by combining x-ray/synchrotron radiography with a new tensile/compression apparatus capable of measuring strain, load and quantifying the microstructure during controlled solidification of Al alloy specimen. Using this new apparatus, the deformation of primary dendrites and the concomitant flow of Cu-rich interdendritic fluid was observed during isothermal and constant cooling rate conditions. Initially, strain was observed to be accommodated by liquid flow, but as the load is increased, void formation combined with liquid necking between grains was prevalent.

This PhD project was generously supported by ALCOA and EPSRC.

Contents

Acknowledgement **3**

Abstract **5**

Contents **7**

List of Figures **10**

List of Tables **16**

Nomenclature **17**

1 Introduction **20**
1.1 Background - aluminium industry 20
1.2 Twin roll casting 21
1.3 Thesis outline 22

2 Literature review **25**
2.1 Twin roll casting process 25
2.1.1 Microstructure and associated defects 27
2.1.2 Laboratory simulation of TRC 31
2.2 Flow of interdendritic liquid 34
2.2.1 Experimental measurement of permeability 35
2.2.2 Numerical models for permeability measurement 37
2.2.3 Flow simulations on real structures 41
2.2.4 Permeability simulations/experimental results 42
2.3 Deformation of semi-solid alloys 44

2.3.1 Experimental/numerical approaches to study deformation in semi-solids . . . 46
2.3.2 Direct finite element modelling . . . 50
2.3.3 Summary . . . 52
2.4 X-ray microtomography . . . 53
2.4.1 Limitations of XMT . . . 55
2.4.2 Summary . . . 56

3 Permeability measurements and viability of combining XMT/FEM to estimate flow stress in semi-solids 57
3.1 Introduction . . . 57
3.1.1 Flow of interdendritic liquid . . . 58
3.1.2 Deformation of dendrite . . . 59
3.2 Methods . . . 61
3.2.1 Direction solidification experiments - XTGS . . . 61
3.2.2 Directional solidification experiments - QDS . . . 63
3.2.3 XMT and image analysis . . . 66
3.2.4 Permeability . . . 68
3.2.5 FE modelling for deformation . . . 70
3.3 Results and discussion . . . 72
3.3.1 Permeability . . . 72
3.3.2 Flow stress . . . 77
3.4 Summary . . . 80

4 Derivation of a constitutive equation for the compressive behaviour of Al-Cu alloys 81
4.1 Experimental methods . . . 83
4.1.1 Sample Preparation . . . 83
4.1.2 XMT and image analysis . . . 83
4.1.3 Meshing of the 3D dendritic structure . . . 84
4.1.4 Gleeble: Thermo-mechanical testing . . . 86
4.2 Simulation methodology . . . 90
4.3 Results and discussion . . . 92
4.3.1 Monolithic behaviour . . . 92

4.3.2 FEM simulation results 96
4.3.3 Macromodel of a twin roll caster 104
4.4 Summary 107

5 *In-situ* synchrotron and x-ray observation semi-solid deformation of Al-Cu alloys 108
5.1 Introduction 108
5.2 Experimental setup 111
5.2.1 Design of the tensile/compression rig 111
5.2.2 Motion control 113
5.2.3 Heating 113
5.2.4 Experiments 114
5.3 Results 117
5.3.1 Compression tests 117
5.3.2 Tensile tests 117
5.4 Summary 126

6 Conclusions and Future Work 127
6.1 Conclusions 127
6.2 Suggestion for further work 128

A FEM simulation input parameters 130

B Compositional variation in dendritic microstructures 134

References 136

List of Figures

1.1 A timeline for aluminium product development. After Sanders [2]. 21

2.1 Continuously cast strip exiting a twin roll caster. After Sanders *et al.* [2]. 26
2.2 Illustration of the solidification and rolling process during TRC. After Sun *et al.* [15]. 26
2.3 An example of macroscopic buckling on twin roll cast Al-alloy. After Yun *et al.* [3]. 28
2.4 Surface bleed on the surface of TRC alloy. After Gras *et al.* [4]. . . 29
2.5 Optical Micrograph of centreline segregation. After Sun *et al.* [15]. 29
2.6 Back scattered (a and b) SEM images of segregates (eutectic structure) in the centreline of high speed TRC cast AA3105. After Gras *et al.* [5]. 30
2.7 Defect map for a twin roll cast AA3105 sample ("B: bleeds, Seg: central segregates and DF: defect free"). After Gras *et al.* [4]. . . . 31
2.8 Isotherms (25 °C apart), phase-change front positions, streamlines ($5 \times 10^{-6}\, m^2/s$ apart) and high pressure zone location using a laminar and non-newtonian model without gravity and buoyancy effects during for modelling TRC. After Cruchaga *et al.* [18]. . . . 33
2.9 Al-Cu phase diagram. Source: DoITPoMS micrograph library. . . 35
2.10 Experimental setup to calculate permeability as used by (a) Poirier [46] and (b) Nielsen *et al.* [37]. 36
2.11 Numerical modelling routes to understand the permeability problem. 37

2.12 Cross-sectional area of an interdendritic channel for liquid flow (a) parallel and (b) normal to primary dendritic arms. After Santos *et al.* [51]. 41
2.13 The evolution of the diagonal terms of the calculated permeability tensors along with the solid fraction as a function of the size of the cubical calculation volume. After Bernard *et al.* [34]. 42
2.14 The figure shows the evolution of triangular avalanche in a granular media. An avalanche is generally a two-phase (snow and water) deformation and requires the same understanding of granular material behaviour as in any semi-solid alloy. After Daerr and Douady [57]. 45
2.15 Post-deformation microstructure of an Mg alloy after complete solidification in a sample deformed at f_S=0.19. After Gourlay and Dahle [63]. 46
2.16 X-ray tomographic images of a sample before and after straining followed by a schematic. After Bart-Smith *et al.* [20]. 47
2.17 Stress-deformation curves of a 2024 and Al-4 wt.%Cu alloys under same temperature and strain-rate conditions. After Ferrante *et al.* [70]. 49
2.18 Segmentation and meshing: (a) original tomogram, (b) segmented data, (c) meshed data, and (d) close-up of mesh at interface in case of a metal matrix composite. After Watson *et al.* [81]. 51
2.19 Schematic of tomography technique with (a) pencil-beam, (b) fan-beam, (c) parallel beam and (d) cone-beam [115]. 54
2.20 Attenuation coefficients of aluminium, copper and silicon as a function of photon energy and the range of energies which can be effectively used for Al-Cu alloys in tomography [118]. 55

3.1 Schematic showing the cylinders used for dendrite shape approximation. 59

3.2 Schematic of the XTGS apparatus. Liquid alloy is directionally solidified and the growth of solidification front is captured on digital detector. The motion of the boron nitride container is controlled so as to track the solidification front at all times. 62
3.3 XTGS radiography image showing the growth of columnar dendritic front and the presence of porosity and bubbles. 64
3.4 Schematic diagram of the solidification rig used for the quenched directionally solidified samples of Al-12 wt.%Cu. 65
3.5 (a) A 3D tomogram of the directionally solidified Al-12 wt.%Cu sample with key microstructural features (Z is the direction of solidification) (b) Histogram showing the frequency of gray values for the 3D volume shown above and a distinct peak for the α-Al dendrite. 67
3.6 A segmented and 3D rendered image of the columnar dendritic structure derived from XMT. 68
3.7 Schematic illustrating RVE selection for permeability calculation along the direction of primary dendrites. 69
3.8 Schematic showing the meshing of the dendrite and the boundary conditions for FE simulations. 70
3.9 Plastic deformation curve for aluminium as used in simulations by Watson [81]. 71
3.10 Moving average value of local permeability at (a) parallel to the dendrite arms, (b) perpendicular to the dendrite arms (Figure 3.7). Note secondary arm spacing is approximately 72 µm. 73
3.11 (a) Flow channels in a direction parallel to primary dendrites. (b) Permeability values from the simulations as a function of edge length of the cubic volume and number of secondary dendrite arms. 75
3.12 Simulation results for deformation of dendrite near the tip. 78
3.13 Load-displacement curve comparison for a dendritic geometry with other simple approximations as derived using FEM simulations. . 79

4.1 Slices of directionally solidified columnar dendritic structure of Al-12 wt.%Cu from (a) close to the tips; (b) deeper in the mush. Both figures show one axial and one sagittal slice as obtained from XMT scans. 84
4.2 (a) SEM micrograph showing the columnar dendritic structure for Al-3 wt.%Cu were used to determine the composition of the dendrites. (b) XMT images are rendered in 3D to segment the phases (solid dendrites and interdendritic liquid) from each other. (c) Close-up of a meshed dendrite tip. Sample RVEs with different fraction solids are selected from similar 3D volumes. Figure (d) shows the structure of the dendrite near the tips where the fraction solid is below 0.2. Figure (e) and (f) show the RVEs with an average fraction solid of 0.60 and 0.77 respectively. 87
4.3 Homogenisation plan for Al-Cu wedges before extracting the samples for compression testing. 88
4.4 True stress - true strain relationship in (a) Al-1 wt.%Cu, (b) Al-3 wt.%Cu measured during compression experiments at $\dot{\epsilon} = 0.01$. The empirical model based results are shown as dashed lines. . . . 93
4.5 Strain rate dependent properties at T = 500 °C for (a) Al-1 wt.%Cu, (b) Al-3 wt.%Cu. The dashed lines show the modelled results for the respective strain rates. 94
4.6 Comparison between the predicted *vs.* experiments stress values for Al-1 wt.%Cu and Al-3 wt.%Cu. Multiple points at a particular temperature represent stress values at different strain rates. The region bounded by the dashed lines represents the ± 10% error. . 96
4.7 True stress - true strain curves for Al-1 wt.%Cu and Al-3 wt.%Cu at three different f_s values (0.13, 0.67 and 1.0) as determined from the FE simulations in ABAQUS. 98

4.8 Normalised flow stress for dendrites of varying f_s from FE computations on Al-1 wt.%Cu and Al-3 wt.%Cu at 1% strain. The dashed line shows the regression fit which is then used as an f_s dependency term in Equation 4.2. These have been compared to the flow stress on other alloys (solid symbols) experimentally tested by prior authors [135, 136]. 99
4.9 Stress distribution in a columnar dendrite ($f_s = 0.2$) for uniaxial deformation illustrates that the complex response of the dendrite shape cannot be modelled with simplified structures. 101
4.10 Schematic of the model with dimensions. 103
4.11 Assumed temperature profile in the 2D model of twin roll caster. . 104
4.12 Stress distribution comparison in a twin roll cast alloy when three different cases for material property are used: (a) Inner bounding cylinder approximation (see Figure 3.13), (b) Equation 4.2 and (c) f_s multiplication factor case (see Figure 3.13). 105

5.1 (a) Tensile/compression rig with compression sample; (b) Schematic of the equipment. 112
5.2 The omega emitter 114
5.3 Actual sample within the boron nitride boat. 115
5.4 X-ray radiography images of the compression experiment at (a) $t = 0$ s, (b) $t = 6$ s, (c) $t = 18$ s, (d) $t = 30$ s, (e) $t = 41$ s and (f) $t = 60$ s. The dark band on top of the frames is the heater. Maximum compression occurs till frame (d) after which the structure becomes highly rigid. 118
5.5 Load response and temperature variation as a function of time during the compression test. 119

5.6 X-ray radiography images for the tensile experiment in the laboratory x-ray source at (a) $t = 67\,\mathrm{s}$, $T = 594\,^{\circ}\mathrm{C}$ and $f_{\mathtt{s}} = 0.56$; (b) $t = 95\,\mathrm{s}$, $T = 587\,^{\circ}\mathrm{C}$ and $f_{\mathtt{s}} = 0.66$; and (c) $t = 141\,\mathrm{s}$, $T = 544\,^{\circ}\mathrm{C}$ and $f_{\mathtt{s}} = 0.8$. The bottom half of each image is a schematic highlighting the key microstructural features. A histogram is also overlayed on each micrograph showing the variation of gray values along the specimen length. 120

5.7 X-ray radiography images of the tensile experiment in the synchrotron x-ray source at (a) $t = 70\,\mathrm{s}$, $T = 589\,^{\circ}\mathrm{C}$ and $f_{\mathtt{s}} = 0.6$; (b) $t = 90\,\mathrm{s}$, $T = 590\,^{\circ}\mathrm{C}$ and $f_{\mathtt{s}} = 0.62$; and (c) $t = 190\,\mathrm{s}$, $T = 601\,^{\circ}\mathrm{C}$ and $f_{\mathtt{s}} = 0.54$. A histogram is also overlaid on each micrograph, showing the variation of gray values along the specimen length. . 122

5.8 Load response and temperature variation as a function of time during the tensile test. The locations marked on the curve correspond to the respective images in Figure 5.6. 124

B.1 SEM image of the columnar structure in directionally solidified Al-12 wt.%Cu alloy. EDX analysis points are marked in the image. 134

List of Tables

2.1 Comparison between morphology parameters measured from 2D sections [37] and 3D tomograms [34], and calculated and experimentally determined equivalent permeability. 43

3.1 Permeability values from present study as compared to other numerical models and to the experimental data 76

4.1 Gleeble experimental conditions for compression tests on Al-1 wt.%Cu and Al-3 wt.%Cu. 88
4.2 Experimentally derived coefficients for Al-Cu alloys for 450 °C < T < 600 °C. 92
4.3 Comparison of flow stress in AA5182 [131] and Al-3 wt.%Cu (Equation 4.1) at $\dot{\epsilon} = 0.0015$. 95
4.4 Comparison of the present results on Al-3 wt.%Cu with Al-4 wt.%Cu by Tzimas *et al.* [95] and Ferrante *et al.* [70]. 101

B.1 EDX analysis of an Al-12 wt.%Cu directionally solidified alloy in Figure B.1 (All elements normalised). 135

Nomenclature

Roman Symbols

$\mathbf{g}$	Gravitational acceleration
$\mathbf{q}$	Flux (discharge per unit area)
$\mathbf{V}$	Apparent velocity through a porous medium
K	Permeability tensor
k	Constant
m	Strain hardening factor
N	Number of photons
n	Strain rate sensitivity factor
P	Pressure
p	Constant
Q	Activation energy
R	Gas constant
T	Temperature
t	Time
W	Atomic number

Z	Direction of columnar growth

Greek Symbols

α	Constant
β	Constant
ϵ	Strain
μ	Viscosity
ρ	Density
σ	Stress
υ	Poisson's ratio

Other Symbols

$\dot{\epsilon}$	Strain rate
$f_{\mathtt{L}}$	Fraction liquid
$f_{\mathtt{S}}$	Fraction solid
λ_1	Primary dendrite arm spacing
λ_2	Secondary dendrite arm spacing
μ_0	Attenuation coefficient
$\rho_{\mathtt{L}}$	Density of the interdendritic liquid
A_1	Constant
A_2	Constant
C_0	Initial solute concentration in the alloy
$C_{\mathtt{eut}}$	Eutectic composition
$C_{\mathtt{l}}$	Solute concentration in the liquid

$C_{\mathtt{s}}$	Solute concentration in the solid
K_0	Flow stress coefficient
k_p	Partition coefficient
L	Characteristic length in macro-scale
l_l	Characteristic length in liquid phase
l_s	Characteristic length in solid phase
m'	Constant
r_0	Characteristic length in RVE
$S_{\mathtt{v}}$	Solid/liquid interfacial area per unit volume

Acronyms

DFEM	Direct finite element modelling
FEM	Finite element modelling
QDS	Quenching directional solidification
RVE	Representative volume element
XMT	X-ray microtomography
XTGS	X-ray temperature gradient stage

Chapter 1

Introduction

1.1 Background - aluminium industry

The development of aluminium alloys over the last century has been driven by the demand for a material which can cover a range of applications. What started as a limited production material has now evolved into a high-volume manufacturing business (Figure 1.1). The applicability of aluminium products has increased manifold with development of newer alloys and continuous improvements in manufacturing technology. Top markets for aluminium products are: automotive and aerospace industries, building and construction, beverage cans and other packaging industries.

Aluminium has emerged as the leading material because of a number of advantages over other competitive materials, including:

- Relatively high tensile, compression and shear strengths;
- Relative light weight;
- High strength to weight ratio;
- High corrosion resistance;
- Ease of fabrication; and
- Recyclable.

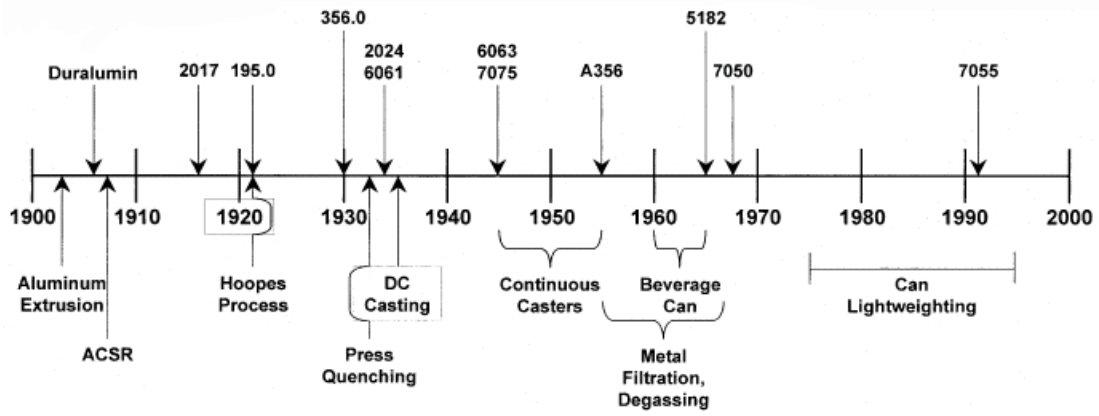


Figure 1.1: A timeline for aluminium product development. After Sanders [2].

The processing of aluminium starts with the extraction from ore mainly using the Hall-Heroult process. Aluminium fabricated products can be divided into two major categories - cast products and wrought products. Castings have played an integral role in the growth of the aluminium industry. But in this thesis, the emphasis will be on wrought products, which occupy the other half of aluminium application spectrum. They are products that have been subjected to plastic deformation by hot / cold working (rolling, extrusion, forging etc.) to transform cast product into a desired shape or form. The microstructural changes associated with deformation and thermal treatments are used to control the properties of the final product. Therefore, a range of properties can be obtained in wrought products by controlling the chemistry, processing and thermal treatments [1].

1.2 Twin roll casting

The fabrication of aluminium into rolled products is an expensive and energy intensive process. It requires the casting of alloys into slabs and a combination of hot and cold rolling to achieve the desired property in the final sheet. Twin roll casting is a proven method for the economical production of thin aluminium sheet (10 - 0.5 mm thick, more than 2 m in width), directly from the melt. The process has numerous advantages:

- reduced capital costs;
- reduced energy costs;
- reduced operating costs; and
- reduced scrap rate.

Despite its large potential, twin roll casting is difficult to control. In many cases, the high productivity regimes lead to the formation of macro-defects (e.g. buckling [3]) as well as micro-defects (centreline segregation [4, 5]).

During twin roll casting, the application of pressure during solidification results in the deformation of the semi-solid and induced flow of the interdendritic liquid. One of the microstructural defects associated with the deformation of the semi-solid is the appearance of segregates formed from the rapid solidification of the solute enriched interdendritic liquid in the centreline. These defects affect the mechanical properties of the sheet severely, which translates into problems during subsequent rolling as well as in the finished product. To understand and predict the formation of segregates at the centreline, both deformation and flow need to be simulated. For accurate prediction of properties at macro-scale, the properties at micro-scale need to modelled precisely. A multi-scale model can then not only help predict semi-solid deformation in roll casting or forming methods but also during the solidification of large castings, e.g. formation of hot tears during direct chill (DC) casting.

1.3 Thesis outline

The present work aims to increase our understanding of the phenomena involved during the semi-solid deformation of Al-alloys by using a novel combination of experimental and computational techniques. Columnar dendritic structures were experimentally generated for Al-12wt.%Cu using a quenching directional solidification setup and an x-ray temperature gradient stage (XTGS) [6–9]. The Al-Cu columnar structure was later characterised in 3D using x-ray microtomography

(XMT). XMT offers unique advantages for the analysis of internal structures of alloys non-destructively and has already been applied in a number of studies within material science. However, its the first time that XMT generated 3D microstructures were used to study micro-scale behaviour of semi-solid alloys. The 3D microstructures were segmented into two phases - the solid dendrite (α-Al), and the Cu-rich interdendritic liquid. These 3D datasets were exported as finite element meshes for control volume simulations.

In Chapter 3, the viability of combining XMT and FEM in a semi-solid regime was investigated through fluid flow and semi-solid deformation studies in 3D microstructures. Firstly , control volume simulations were performed to study the propensity of interdendritic fluid flow in a columnar dendritic network. Fluid flow was simulated using a stokes flow solver developed by Bernard *et al.* [10]. The solution was used to estimate permeability of the structure and anisotropy in flow of the interdendritic liquid in a columnar dendritic structure. These simulations were also performed on different sized volumes to establish the minimum microstructure size which had the properties of the macrostructure. This volume is termed as the representative volume element (RVE). Through this study, a relationship between the characteristic microstructure size and the RVE was established. Secondly, 3D columnar dendritic structures were meshed and deformed using commercial FEM codes to illustrate the feasibility of performing a detailed study where such structures could be used as a representation of a semi-solid alloy.

A second set of simulations was performed on 3D volumes of different fraction solid derived from the quenched columnar dendritic structure of Al-Cu alloy. A commercial finite element package was used to study the deformation behaviour of the structure as a function of strain rate, fraction solid and temperature. Accurate material properties for the dendrite phase were measured by performing high temperature compression experiments on alloys with dendritic compositions. Results from these simulations were used to derive a constitutive equation for the high temperature deformation behaviour of Al-Cu alloy as presented in Chapter 4.

On the experimental side, an existing tensile/compression rig was adapted to perform semi-solid deformation experiments on Al-alloys *in-situ* an x-ray source for real-time image recording while measuring the load response of the semi-solid. In Chapter 5, a set of tension and compression experiment results have been presented which provide new insights into the strength of the semi-solid. However, due to limited time, only preliminary analysis has been presented here.

The study has provided a novel methodology to understand the semi-solid deformation process in Al-alloys which has its direct implications not only to the problem in hand (twin roll casting) but also to a wider range of processes and alloys. For example, the fraction solid dependency during deformation can be easily applied to other alloy systems. The experimental setup was also successfully designed to blend in semi-solid tensile/compression tests with x-ray radiography tools to directly correlate microstructural changes with application in loads.

Chapter 2

Literature review

2.1 Twin roll casting process

Twin roll casting (TRC) has emerged as a proven technology for economical production of thin aluminium sheet directly from the melt. The advantages of this casting technique are numerous-reduced capital costs, energy consumption, operating costs and scrap rate compared with a conventional DC casting route.

Though continuous casting technology had been developed in the 19^{th} century, its application on the commerical production of aluminium products started 50 years ago by Properzi [11]. Rigamonti started slab casting of aluminium alloys into narrow strips (100 mm) of 20 mm thickness. Other casters in the 1950s (Alcan, Pechiney and Hunter) also manufactured products with limited widths [12]. The development of aluminium casters with wider products in the late 1950s was a critical breakthrough which allowed the process to be competitive with rolling mills. One of the initial casters installed at Alcan was developed by Hazelett was a twin-belt caster with steel belts [2, 13]. Another caster, developed by Hunter which was commercialised in 1950s used water-cooled steel rolls to produce continuously cast aluminium strips [14].

Roll cast products have typically, a thickness of 5-10 mm. But more importantly, with continuous improvements, the width of these products have increased to more than 2 m which has made twin-roll casters, the largest producers of

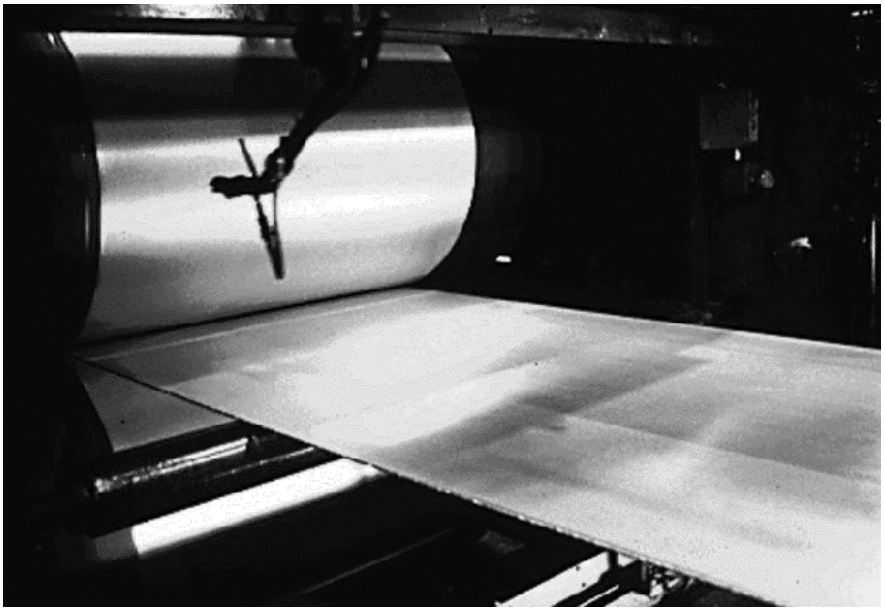


Figure 2.1: Continuously cast strip exiting a twin roll caster. After Sanders *et al.* [2].

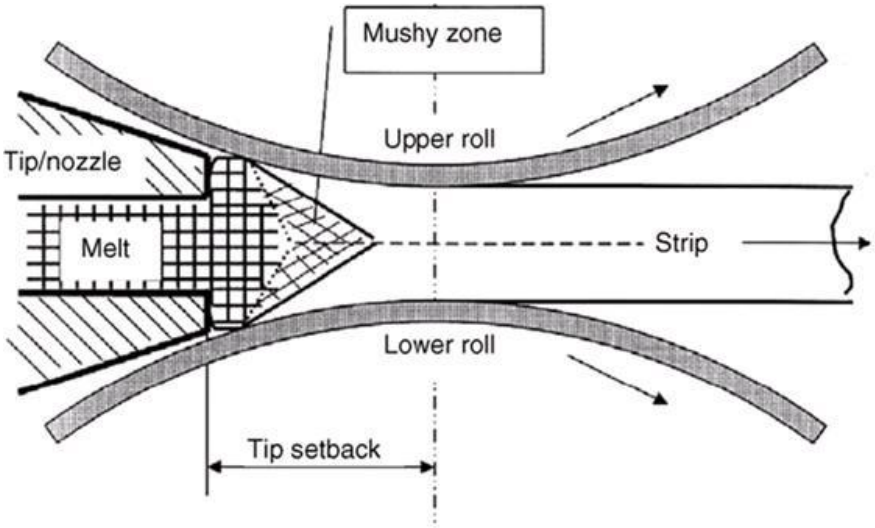


Figure 2.2: Illustration of the solidification and rolling process during TRC. After Sun *et al.* [15].

continuously-cast aluminium rolled products. A typical roll caster in operation is shown in Figure 2.1 and a schematic is shown in Figure 2.2.

2.1.1 Microstructure and associated defects

Though TRC is an attractive technique to cast Al-alloys into thin sheets, it faces its own set of disadvantages which has prompted a continued research interest in this area. Sheets as thin as 0.5 mm can be cast directly from the melt, but the number of defects which occur, limit the productivity of this process.

In TRC, molten metal is fed onto water-cooled rolls, where it solidifies as it is rolled. The combined effect of high pressure and rapid solidification results in the transport of material. As the alloys solidify, the liquid is continuously enriched with the alloying elements (microsegregation) and gets squeezed through the solidified structure to form segregates.

Yun *et al.* [3] suggested that the defects during TRC can be broadly divided into three major categories:

- macroscopic buckling;
- surface defects; and
- segregates.

Macroscopic buckling (Figure 2.3) occurs when the metal undergoes different amount of forward slip at the contact with the rolls. Since there are non-uniformites present in the incoming metal due to differences in metal feed temperature, lubricants or tip position, the metal is deformed by varying degrees at different locations [3, 4]. This can cause result in buckling of the sheet. Buckling is much less severe in thick sheets where the stresses are redistributed better. In TRC, buckling is reduced as the difference in slip at the contact layer is accommodated by the movement within the semi-solid region. Therefore, even for a macroscopic defect in TRC, the understanding of the semi-solid layer is critical.



Figure 2.3: An example of macroscopic buckling on twin roll cast Al-alloy. After Yun *et al.* [3].

The formation of defects at the surface is attributed to the appearance of the enriched liquid in a disc-like formation on the surface. Gras *et al.* [4] explained that as the metal is squeezed between the rolls, it undergoes micro-buckling. This doesn't result in the breaking of the sheet mainly because everything behind this layer is semi-solid. Therefore, this buckled structure is sustained till the pressure between the rolls squeezes the liquid into the gaps formed due to the buckles. Gras *et al.* explained it in simple terms as a damp sponge expelling water when squeezed. The liquid which fills up these spaces solidifies immediately forming droplets.

Under the rolls, these droplets undergo deformation in the direction of rolling, resulting in bleeds, which further explains the stretched disc shape (Figure 2.4). However, the TRC process involves both solidification and deformation, large variations in metal temperatures, velocity fields and pressure distribution exist. The flow of the liquid from the centre towards the surface cannot be ruled out. Forbord *et al.* [16] did a comparative study of the experimental results and the models. Their results show the presence of low pressure zones on the surface of the sheets. Since the pressure between the rolls is already high, the low pressure

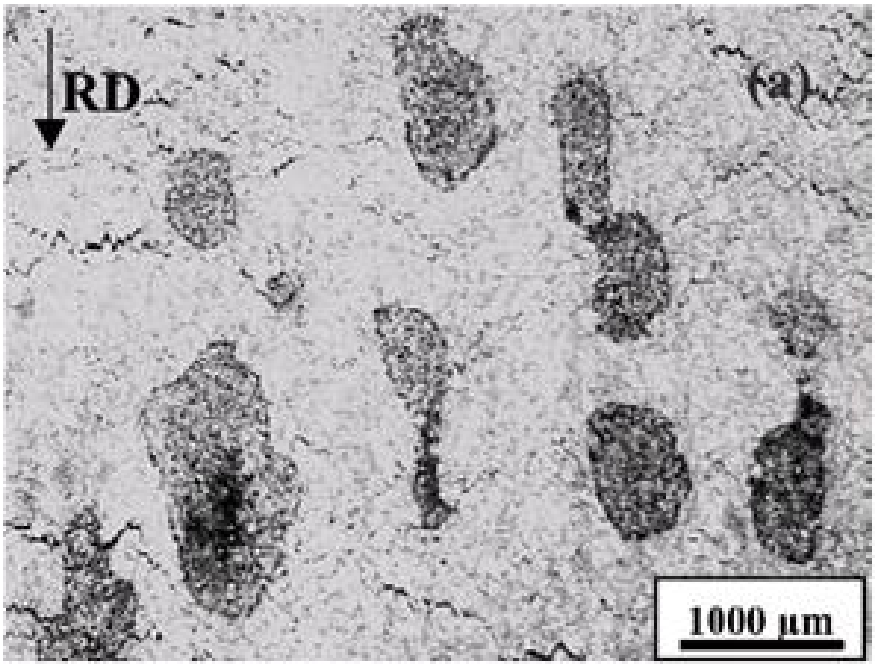


Figure 2.4: Surface bleed on the surface of TRC alloy. After Gras *et al.* [4].

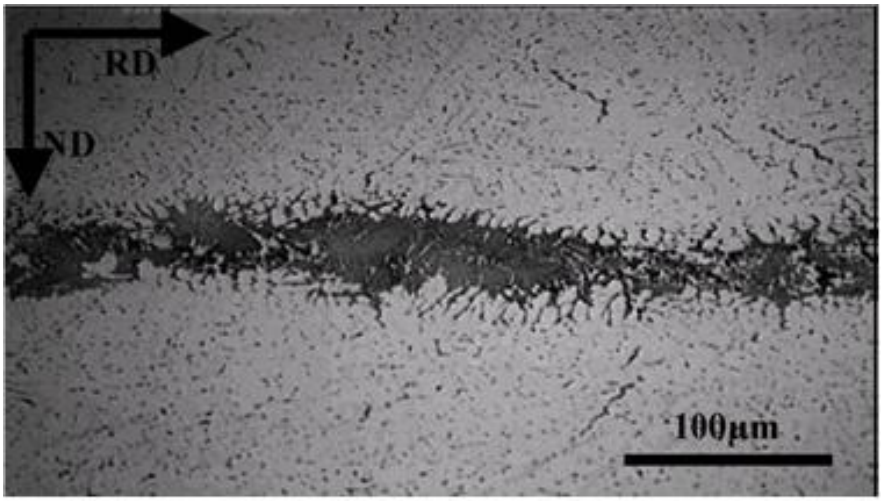


Figure 2.5: Optical Micrograph of centreline segregation. After Sun *et al.* [15].

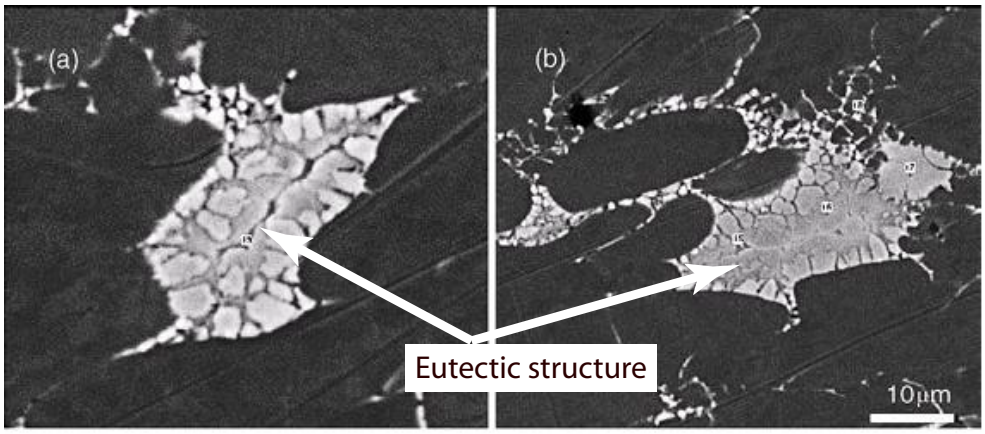


Figure 2.6: Back scattered (a and b) SEM images of segregates (eutectic structure) in the centreline of high speed TRC cast AA3105. After Gras *et al.* [5].

fields on the surface provide an outlet for the liquid.

Segregates at the centre are the result of deformation through rolls and solidification dynamics [3]. At high casting speeds, a deep sump is formed which retains a large volume of liquid in between the two solidification fronts approaching from the two rolls. The build up of the pressure results in an increased rate of heat extraction and rapid solidification at the centre. The solute rich liquid at the centreline solidifies and can give a eutectic structure depending on the composition of the alloy. The pressure of the rolls also forces the flow towards the centreline as the layers in contact with the rolls are solidified. As the liquid flows through the dendrites, channels are formed which facilitate the flow of solute rich liquid towards the centre of the sheet. The solute rich liquid is the last to solidify at the centre of the sheet forming segregates (Figure 2.5). These segregates have a fine eutectic structure due to the rapid solidification of the trapped solute (Figure 2.6).

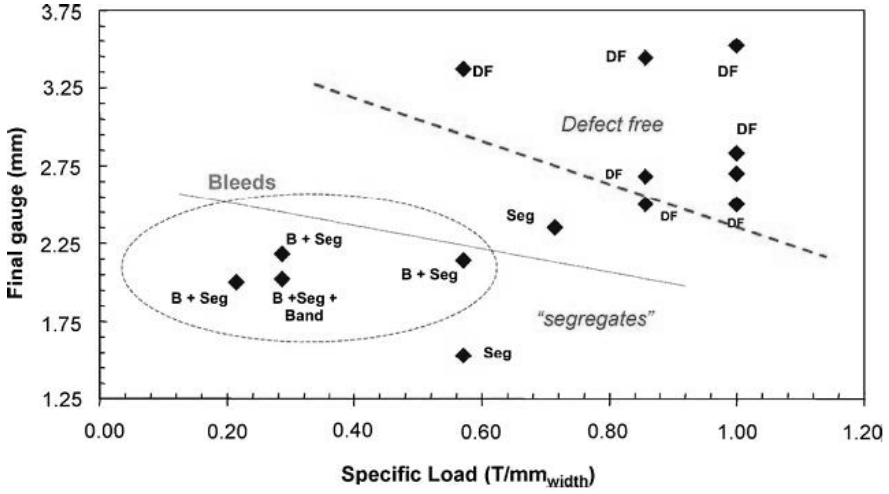


Figure 2.7: Defect map for a twin roll cast AA3105 sample ("B: bleeds, Seg: central segregates and DF: defect free"). After Gras *et al.* [4].

2.1.2 Laboratory simulation of TRC

Laboratory experiments and computer models are necessary to understand the underlying phenomena in TRC in detail. Since the cost of experiments in a real caster is high, scaled laboratory setups provide an inexpensive method of testing various alloys in a wide range of casting conditions. Similarly, computer models of the process help in identifying the key parameters which directly effect the quality of sheet produced.

Prior studies mentioned in the previous section have emphasised the microstructural changes based on their works in laboratory casters [4, 5, 16, 17]. They were also able to show that the defects during twin roll casting occur only for a particular set of casting conditions. If all the results coming from different casts are grouped together, it is possible to build a convenient graphical representation to define the combination of necessary experimental conditions to generate microdefects. This provides us with the conditions to reproduce experiments to study a particular form of defect. An example of the defect map is given in Figure 2.7 as derived by Gras *et al.* [4] for an AA3105 alloy sample.

A series of experiments performed by Gras *et al.* [4] (Figure 2.7), were able to demarcate regions which had propensity for certain defects as a function of final gauge thickness and the specific load. Such defect maps are particularly useful in industrial setups as they provide a reasonable idea of expected microstructure to an operator. However, these results are based on a number of trial and error routines and do not provide any physical reasoning on why and how the defects are formed. Without any concrete understanding of the microstructural scale phenomena, even a slight change in TRC operation parameters (temperature, alloy composition, material of the rolls, etc.) would require another set of trial and error experiments, which are both expensive and unclear.

Computer simulations have provided an easier and cheaper option to highlight the critical production conditions through various macromodels of the twin roll caster [13, 16, 18, 19]. At a macro-scale, the twin roll casting problem is easier to define and the following phenomena need to be considered:

- Heat-transfer through the rolls and its effect on the solidification profile of the sheet.
- Deformation of the sheet as the pressure is applied through the rolls.
- Fluid flow within the semi-solid region.

Such numerical simulations have been able to predict the thermal and pressure profiles as a function of casting speed and roll pressure. One such model [18] in Figure 2.8 shows the effect of assumptions of flow on the temperature, solidification front, flow streamlines and pressure zones during twin roll strip casting. Though these macromodels provide an alternative to extensive experiments, they are limited in their understanding of micro-scale and local changes.

The development in computer modelling and characterisation techniques has opened up more ways of understanding the coupled fluid flow, heat transfer and deformation mechanism which exists in a twin roll caster. This study focuses on the microstructural deformation and interdendritic fluid flow within a twin roll

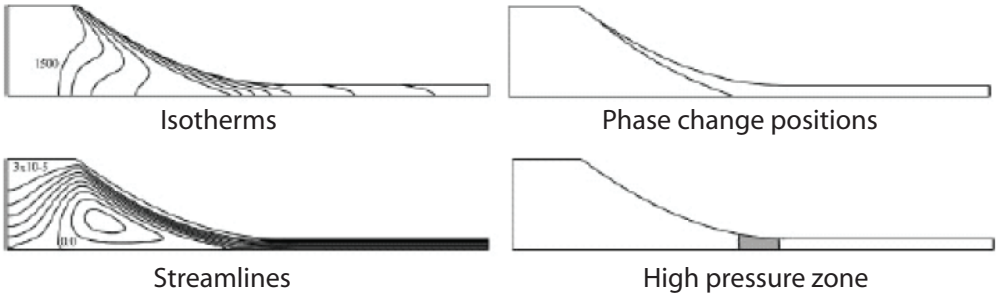


Figure 2.8: Isotherms (25 °C apart), phase-change front positions, streamlines ($5 \times 10^{-6}\, m^2/s$ apart) and high pressure zone location using a laminar and non-newtonian model without gravity and buoyancy effects during for modelling TRC. After Cruchaga *et al.* [18].

casting with a novel combination of experimental, x-ray microtomography and finite element modelling techniques.

2.2 Flow of interdendritic liquid

Most metals are used in an alloy form to obtain desired properties. The mixing of metals results in the metal solidifying over a temperature range. Therefore, when these alloys are cast, it becomes a tedious job to control the solidification process and a lot of research is dedicated to modelling of solidification processes [20–27]. As far as metals growing under normal solidification conditions are concerned, local equilibrium is assumed to hold at the solid/liquid interface. Then, at the interface, the solid concentration, $C_{\mathtt{s}}$, is related to the liquid concentration, $C_{\mathtt{l}}$ by the partition coefficient k_p (Figure 2.9), defined as:

$$C_{\mathtt{s}} = k_p.C_{\mathtt{l}} \tag{2.1}$$

This compositional difference will always lead to concentration variations in the solidified alloy, which is known as segregation [22] when the initial solute concentration, $C_{\mathtt{0}}$, is not equal to the eutectic composition, $C_{\mathtt{eut}}$. The solute during solidification can be transported by diffusion and/or convection, but in processes like TRC, the solute transport mainly takes place due to the flow of interdendritic liquid, driven by pressure applied through the rolls. Therefore, in the case of TRC, quantification of the fluid flow is critical when segregates at the centreline form.

Permeability characterises the ease with which the interdendritic liquid can flow through the dendritic network [28–33]. The formation of defects in industrial metal castings critically depends on the flow of the interdendritic liquid in the mushy zone. In shaped castings, for example, the permeability determines the pressure drop associated with liquid feeding to compensate for solidification shrinkage, which in turn affects the solubility of gas in the melt and porosity formation [34–36]. During twin roll casting, where pressure is applied to the solidifying metal through the rolls, squeezing of the liquid in the mushy zone is one of the main mechanisms which result in the formation of segregates.

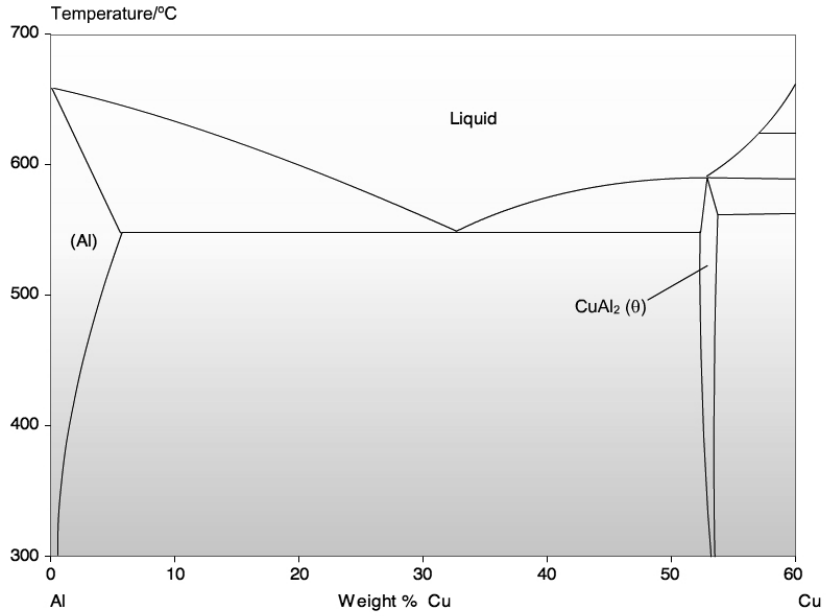


Figure 2.9: Al-Cu phase diagram. Source: DoITPoMS micrograph library.

2.2.1 Experimental measurement of permeability

A number of experiments have been performed to empirically assess the values of permeability [32, 33, 35, 37–45]. The designs of these permeameters have had problems associated from preparation of the samples to maintaining a uniform temperature during the experiment. Other experimental difficulties were associated with the dynamic nature of the problem. Two of the designs used to measure permeability are shown in Figure 2.10.

Al-Cu alloys undergo a significant coarsening and globularisation during casting in permeability experiments. Since, the microstructures change continuously, they could have the following effect on the results of the experiments:

1. For the modelling of interdendritic flow in casting processes, permeability measurements for the different types of morphologies are required for castings under different conditions. During these experiments, temperature is held constant for longer periods of time to maintain a particular f_s. The

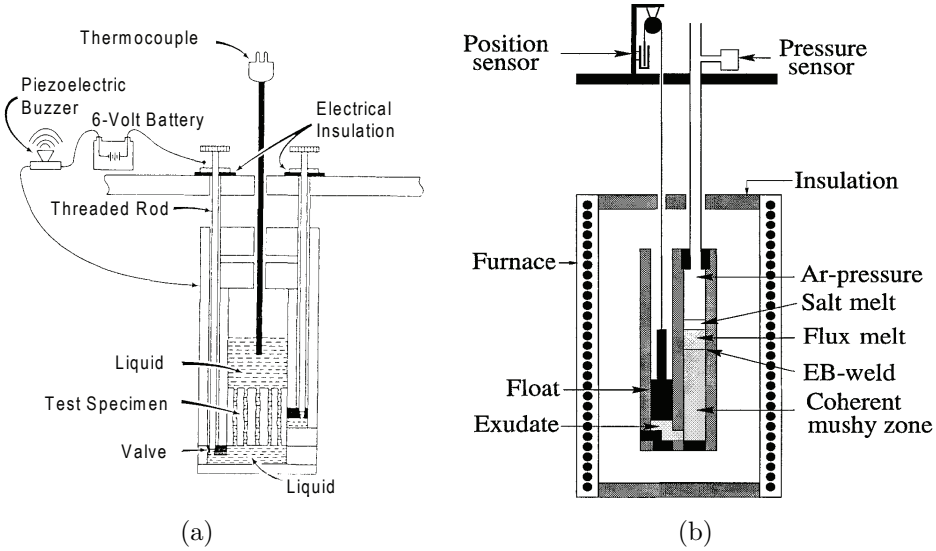


Figure 2.10: Experimental setup to calculate permeability as used by (a) Poirier [46] and (b) Nielsen *et al.* [37].

increase in timescale in the experiments compared to real castings effect the morphology as grain coarsening occurs. This difference causes inaccuracies in the permeability experiments [37].

2. During the experiments, as the pressure is applied, the interdendritic liquid has a tendency to flow along the preferential channels. The formation of these channels results in the experiments being inaccurate [39].

3. To reveal the morphology at a particular instance of time, samples need to be quenched. The limitation of this method is that only one data point is obtained from each experiment [47].

Therefore, it could be concluded from the above inferences that measurement of permeability experimentally has certain drawbacks. In contrast, numerical methods provide a fast and reliable route to study the flow through dendritic structures.

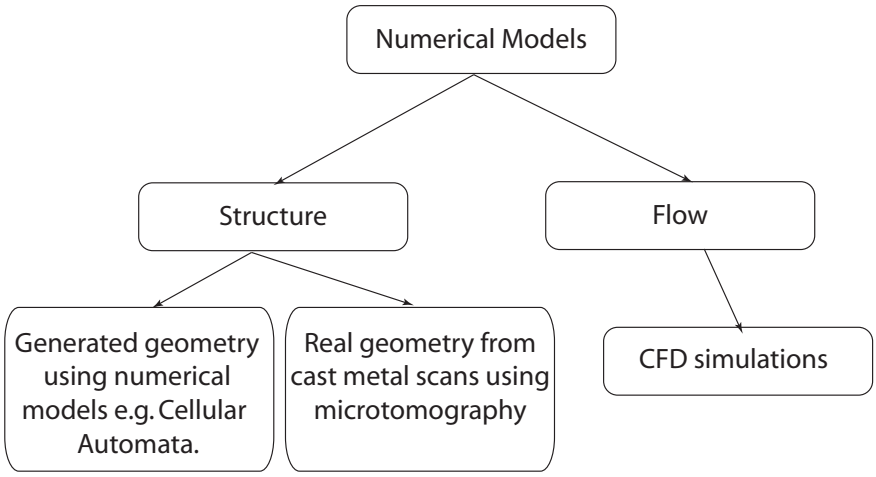


Figure 2.11: Numerical modelling routes to understand the permeability problem.

2.2.2 Numerical models for permeability measurement

The inherent problems with the experimental setup to calculate permeability values for a dynamic system has forced many researchers to come up with numerical models to clearly understand the nature of the permeability problem in a solidification regime [33].

The numerical problem of calculating permeability for dendritic structures can be broken down into two challenges: (i) *modelling the structure*; and (ii) *modelling the flow* (Figure 2.11). The calculation of flow numerically involves the solution of the Navier-Stokes equation and has been common in all the numerical models. For the structure, various simplified models (e.g. flow through stacked cylinders) have been used to compare the results of experiments with the numerical calculations of simplified structures [48]. Lately, new approaches for structure modelling have emerged - simulated microstructures (through cellular automata) [49] and real 3D microstructures [34, 49, 50]. The advantages of such techniques lie in their ability to simulate different structures and details within them, and their reproducibility.

Brown *et al.* [49] worked on the simulated equiaxed dendritic structure to calculate the permeability. The distinct advantage of using this method over the real 3D microstructures lies in the fact that in the simulated structure, various morphologies can be studied easily as compared to the experimentally derived microstructure even though the size of the microstructure that could be simulated is presently limited as it is highly computationally intensive.

The other major issue in numerical modelling of permeability is the computational time required to solve the flow equations. The flow equation for solving the flow of the interdendritic liquid through the dendritic structure which combines Navier-Stokes equation and Darcy term was derived by Ganesan and Poirier [39]:

$$\rho_{\text{L}} \left(\frac{\partial \mathbf{V}}{\partial t} + \mathbf{V}.\nabla \mathbf{V} \right) = -\nabla P + \rho_{\text{L}} \mathbf{g} + \frac{\mu}{f_{\text{L}}}.\nabla^2 \left(f_{\text{L}}.\mathbf{V} \right) - \mu.f_{\text{L}}.\left[K \right]^{-1} V \tag{2.2}$$

where, ρ_{L} is the density of the interdendritic liquid, f_{L} the volume fraction of the interdendritic liquid, $\mathbf{V}$ the velocity of the interdendritic liquid, P is the pressure, $\mathbf{g}$ is the gravitational acceleration, μ is the viscosity of the interdendritic liquid and K is the permeability tensor.

$$K = \begin{bmatrix} K_{xx} & K_{xy} & K_{xz} \\ K_{yx} & K_{yy} & K_{yz} \\ K_{zx} & K_{zy} & K_{zz} \end{bmatrix} \tag{2.3}$$

The computational costs involved in solving the above equation are exorbitant and impractical with the present computers. Darcy's equation is a simpler relation to estimate the permeability in a porous media and has been used in understanding the flow through soils. Derived by H. Darcy, the equation can be written as [28]:

$$\mathbf{q} = -\left(\frac{K}{\mu} \right) \left(\nabla P - \rho.\mathbf{g} \right) \tag{2.4}$$

Equation 2.2 has been approximated in the interior of the mushy zone (where $0 << f_{\text{L}} << 0.7$), where it reduces to the Darcy's equation, which is [46]:

$$\mathbf{V} = -\left(\frac{K}{\mu.f_{\mathtt{L}}}\right)(\nabla P - \rho.\mathbf{g}) \tag{2.5}$$

This is a much simpler equation to solve and cuts down the computational time by a large factor. The value of the permeability tensor can be expressed using the Kozeny-Carman relationship. Most experiments show good agreement with this expression within a certain range of liquid or solid fractions ($0.5<f_{\mathtt{S}}<0.9$).

The Kozeny-Carman relationship can be expressed as [49],

$$K = \frac{(1-f_{\mathtt{S}})^3}{k.{S_{\mathtt{V}}}^2} \tag{2.6}$$

where, $f_{\mathtt{S}}$ is the volume fraction of solid and $S_{\mathtt{V}}$ is the solid-liquid interfacial area per unit volume. In the case of interdendritic liquid flow, it is often assumed that k has a value of 5 and that $S_{\mathtt{V}}$ remains constant as $f_{\mathtt{S}}$ increases. Brown *et al.* [49] argued that these assumptions may not be valid for interdendritic fluid flow for complicated geometries where flow channel dimensions and shapes are not uniform.

Poirier [46] studied the columnar dendritic structure in Pb-Sn and borneol-parrafin alloys. He arrived at relationships between permeability and the morphology of solid dendrites based on regression analysis of the data and comparison with simple flow models. The study suggested that for flow parallel to the primary dendrite arms, the important morphological aspects are the volume fraction solid ($f_{\mathtt{S}}$) and the primary dendrite arm spacing (λ_1). For flow normal to primary dendrite arms, the permeability depends upon the secondary dendrite arm spacing (λ_2) as well as λ_1 and $f_{\mathtt{S}}$. Their main conclusions were:

- For $0.30 < f_{\mathtt{S}} < 0.83$, the permeability for parallel flow are represented best by the Hagen-Poiseuille model, and can be calculated using the following simplified expression,

$$K = 3.75 \times 10^{-4}.{\lambda_1}^2(1-f_{\mathtt{S}})^2 \tag{2.7}$$

- For $0.34 < f_s < 0.81$, the permeability for normal flow are represented best by a multilinear regression,

$$K = 9.66 \times 10^{-18}.{\lambda_1}^{0.699}.{\lambda_2}^{2.73}(1 - f_s)^{3.34} \tag{2.8}$$

- When it is necessary to extrapolate beyond the scope of experimental values, the Blake-Kozeny model is applicable. For parallel flow,

$$K = C_2.{\lambda_1}^2.\frac{(1 - f_s)^3}{f_s} \tag{2.9}$$

  Where, based on a multilinear regression, C_2 is:

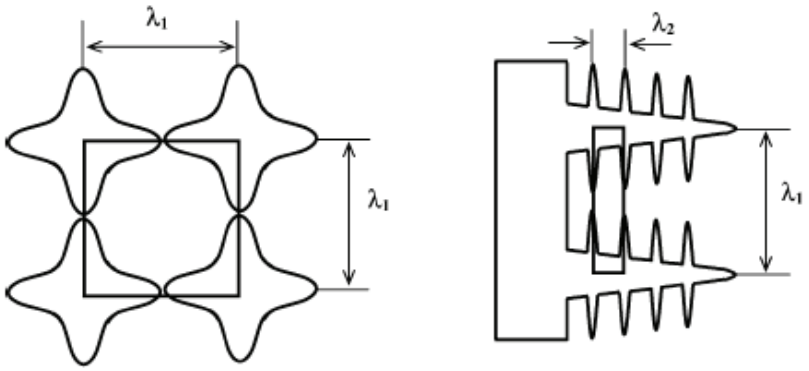
$$C_2 = 4.53 \times 10^{-4} + 4.02 \times 10^{-6}.(1.1 - f_s)^3 \tag{2.10}$$

  For normal flow,

$$K = 1.73 \times 10^{-3}.\left(\frac{\lambda_1}{\lambda_2}\right)^{1.09}.{\lambda_2}^2.{f_s}^{-0.749}.(1 - f_s)^3 \tag{2.11}$$

The regression models were extended to high solid volume fractions (up to 0.98) by Bhat *et al.* [48] by solving Navier-Stokes equation for velocity and pressure in a direction perpendicular to the primary dendrites in columnar structure.

For the measurement of flow along the primary arms and in a direction normal to it, Santos *et al.* [51] derived expressions for the permeability in both the directions. In their expressions, the tortuosity of the channel, τ is taken into account [51]. Tortuosity of the interdendritic channels has been previously studied by image analysis and is an important factor to be calculated in the measurement of flow [52]. Figure 2.12 shows how primary and secondary dendrite arms spacing affect the flow in the directions parallel and normal to the primary dendrite arms. However, the work by Santos *et al.* was based on simple 2D models, whereas, the fluid flow in a 3D structure could be very different when compared to a 2D geometry [53].



(a) (b)

Figure 2.12: Cross-sectional area of an interdendritic channel for liquid flow (a) parallel and (b) normal to primary dendritic arms. After Santos *et al.* [51].

2.2.3 Flow simulations on real structures

Bernard *et al.* [54] calculated permeability in the semi-solid by solving the volume averaged Darcy's law. Several simplifications of Stokes equation are necessary in order to arrive at the Darcy's law. In general, these simplifications are valid if the following length scale constraints are satisfied:

$$l_l, l_s << r_0 << L \tag{2.12}$$

where, l_s, l_l, r_0 and L are the characteristic length of the solid and the liquid phases, the RVE and the large scale problem. A good choice of RVE is necessary to optimise between the size of the tomographic volume and the computation costs required to run flow simulations. Therefore, it is necessary to find out the smallest size of the 3D volume above which the value of permeability and fraction solid, both remain constant (Figure 2.13).

Bernard's model [34] for calculating the flow works well for structures which have some form of uniformity because the boundary conditions assumed are periodic. Therefore, though the model works well for fully grown dendritic structure,

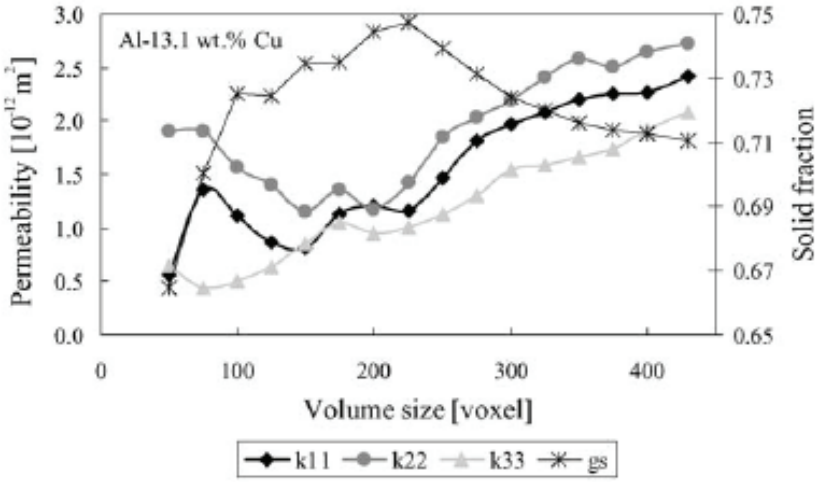


Figure 2.13: The evolution of the diagonal terms of the calculated permeability tensors along with the solid fraction as a function of the size of the cubical calculation volume. After Bernard *et al.* [34].

it has its limitations when working with domains which have non-periodic nature (e.g. dendrite tips).

2.2.4 Permeability simulations/experimental results

In the last few years, a number of investigators have tried to understand the flow in the semi-solid by estimating the permeability of such samples. It is interesting to see how the progress has been made in relation to the calculation of the permeability tensor over last few years. It started with simplified models of porous structures which suggested fairly accurate values, to the experiments which were done at the actual temperatures to understand if the simplified models still held good or not. Recently, the shift has been to simulated structures or tomographs of the real samples. The results in Table 2.1 show that measured values of permeability in the experiments have been quite close to the ones from the simulated flow calculations done on the reconstructed 3D structure.

A common way to compare the permeability data is to plot the dimensionless

permeability, $K.S_v^2$, as a function of fraction solid. This also facilitates the comparison to the Kozeny-Carman model as in Equation 2.6. The results of various studies are compared in Table 2.1 and it shows a good correlation between the values calculated experimentally and numerically.

The lack of control on the experiments to measure the permeability of the semi-solid in alloy systems has opened a lot of scope for the modelling of flow. Flow models have been based on the simplifications of the Navier-Stokes equation and Darcy's law. But the real nature of flow and its response to changing pressure conditions, like in the case of TRC, are still open to further research. The advances in the computational capabilities are helping in the development of more complex models. This has also led to the development of phase-field models [55] and network models [56] as a tool to understand the dynamics of the semi-solid system.

Table 2.1: Comparison between morphology parameters measured from 2D sections [37] and 3D tomograms [34], and calculated and experimentally determined equivalent permeability.

Sample	Source	f_s	$S_v(m^2)$ $(10^4 m^{-1})$	$K(\times 10^{-12} m^2)$
Al-10 wt.%Cu	Simulated[37]	0.78	3.5	1.6
	Measured[34]	0.83	3.5	0.92
Al-13.1 wt.%Cu	Simulated[37]	0.71	5.2	2.2
	Measured[34]	0.74	6.4	1.9
Al-15.8 wt.%Cu	Simulated[37]	0.72	6.4	0.83
	Measured[34]	0.68	12	1.11

2.3 Deformation of semi-solid alloys

Understanding the deformation of semi-solid materials is critical when predicting the formation of defects during many phenomena, ranging from the casting of metals to granular flow of magma in volcanoes [57–62] (see Figure 2.14). During the initial stages of solidification in alloys, equiaxed crystals are suspended in interdendritic liquid and the material behaviour is similar to suspensions. Recently, an increased understanding of granular material deformation in physics has led to analogous applications in solidification science; for example, Gourlay and Dahle [63] analysed the formation of dilatant shear bands under shear in semi-solid alloys with an equiaxed structure using the principles and techniques developed in the area of granular mechanics (Figure 2.15). However, these modeling methods are limited to circular or spherical morphologies [60, 61].

In solidification processing, although globular solids can be present during the semi-solid state, in majority of processes, solidification occurs via the formation of much more complex microstructures such as equiaxed or columnar dendrites [29, 31]. The flow of semi-solid materials is often approximated as a two phase flow similar to granular material but this is not appropriate at higher solid fractions [64, 65]. As the fraction solid increases, the solid crystals impinge against each other resulting in a sharp increase in strength, termed the coherency point of the semi-solid. The onset of coherency in semi-solids with complex morphologies is earlier than those which have a globular morphology [66]. These complex morphologies have been shown to potentially have a very different rheological behaviour than globular materials [67, 68].

In TRC, high pressure is employed on the rolls to deform the semi-solid aluminium alloys to thin sheets. The metal experiences temperature differences which induce convection in the liquid and deformation of the solid. The combination of these two effects can result in a lack of feeding in the dendritic network resulting in defects like microporosity and hot-tears [69].

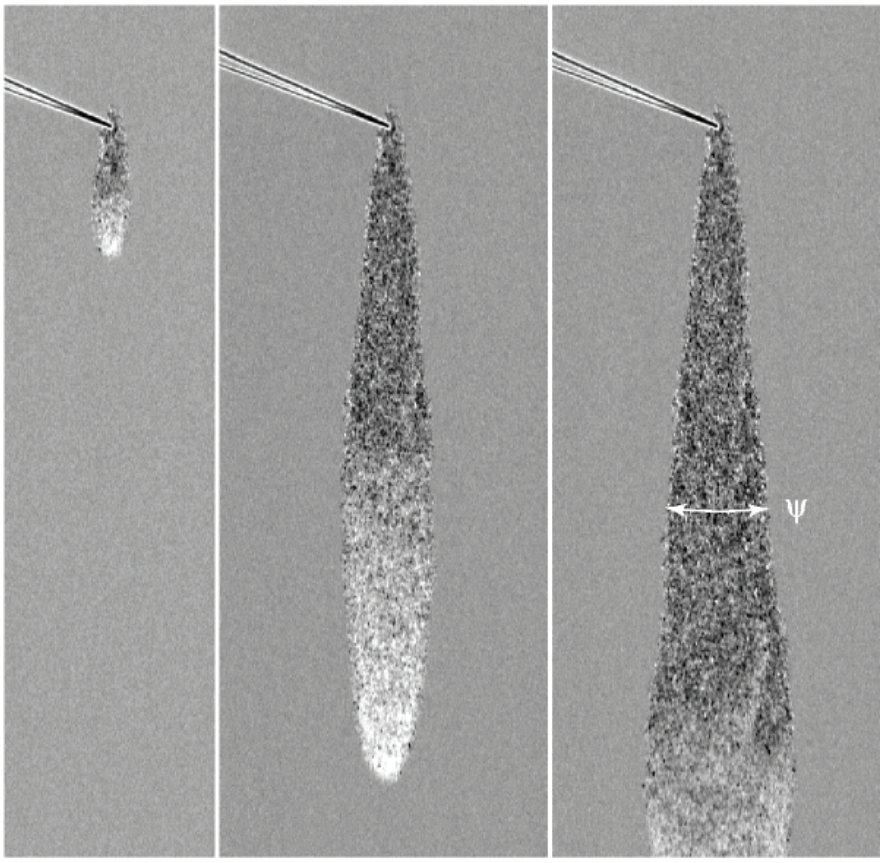


Figure 2.14: The figure shows the evolution of triangular avalanche in a granular media. An avalanche is generally a two-phase (snow and water) deformation and requires the same understanding of granular material behaviour as in any semi-solid alloy. After Daerr and Douady [57].

In the conditions existing during TRC, the effect of deformation is accentuated by the pressure being applied through the rolls. The solidifying metal may act as a solid or a pseudo-plastic under compression. Therefore, the rheology and deformation behaviour becomes an important aspect to understand the final microstructure of the rolled product [70]. Presently, the high temperature constitutive equation used for aluminium alloys in the industry is [71, 72]:

$$\sigma = \frac{1}{\alpha} \, sinh^{-1} \left[\frac{\dot{\epsilon} \, exp(Q/RT)}{\beta} \right]^{\frac{1}{m'}} \tag{2.13}$$

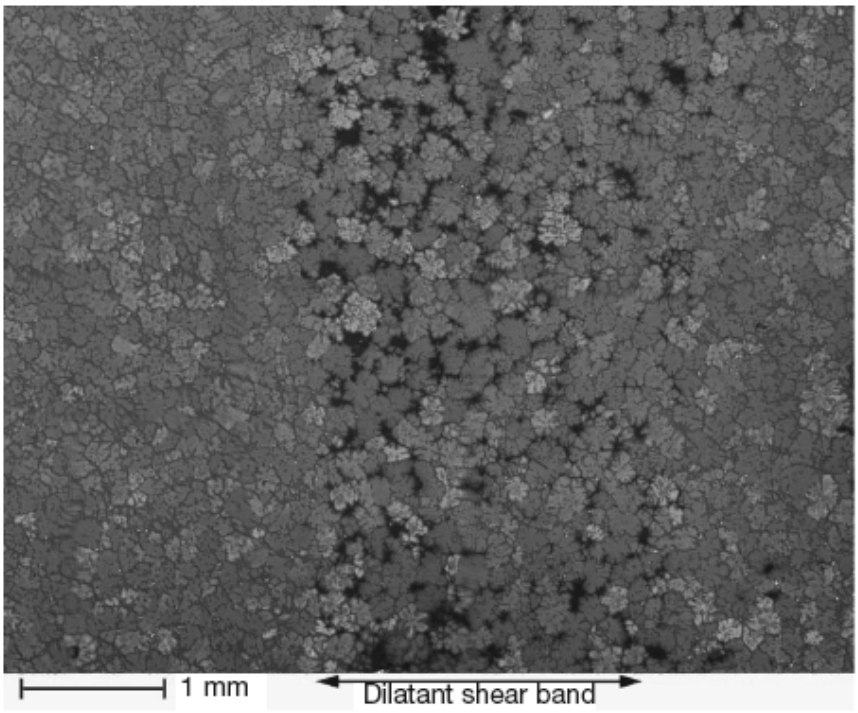


Figure 2.15: Post-deformation microstructure of an Mg alloy after complete solidification in a sample deformed at f_s=0.19. After Gourlay and Dahle [63].

where, α, β and m' are experimentally determined constants. However, the above relation is only true for temperatures below solidus. In twin roll casting conditions, molten metal is fed to the rolls at above the melting point and during deformation, there is a range of f_s present throughout the cross-section of the sheet. Therefore, a new constitutive equation needs to be developed which would take into account the microstructural information relevant to TRC.

2.3.1 Experimental/numerical approaches to study deformation in semi-solids

Experiments have been performed by prior authors to understand the deformation mechanism in cellular aluminium alloy structures using XMT by Bart-Smith *et al.* [20]. They used tomography to derive cellular strain information from the images and observed that plastic deformation occurred in localised regions (Fig-

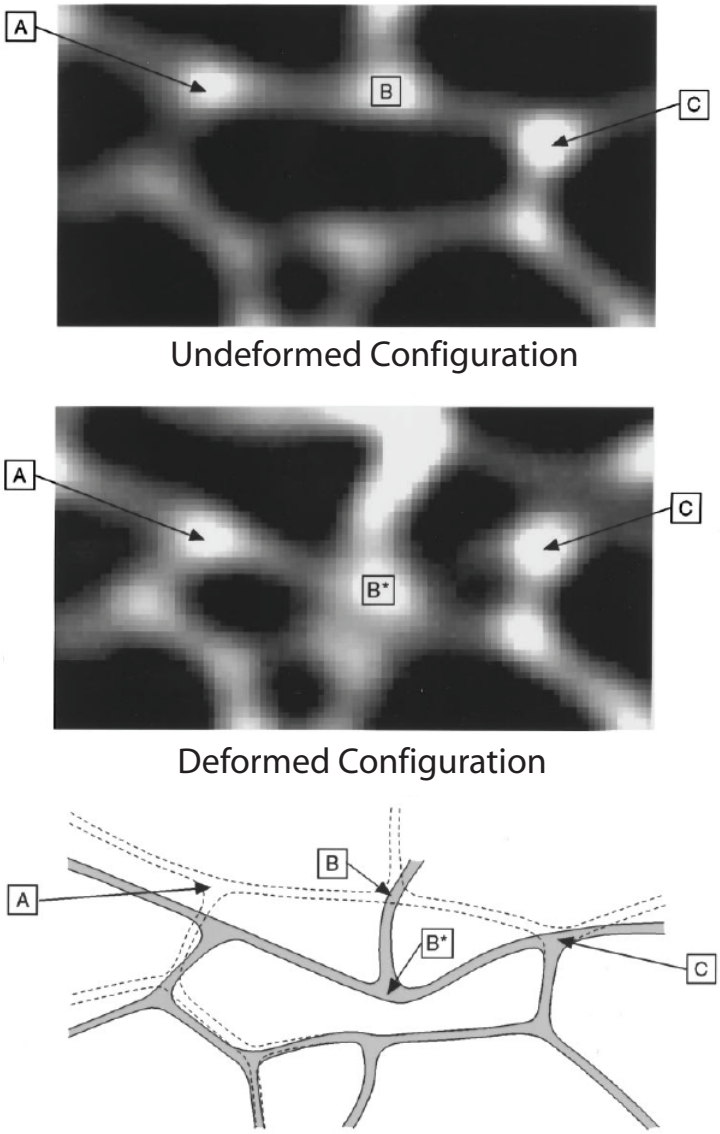


Figure 2.16: X-ray tomographic images of a sample before and after straining followed by a schematic. After Bart-Smith *et al.* [20].

ure 2.16). Outside these small regions, the material remained elastic. However, this study was limited in analysing only cellular structures and the results were based on observations of experiments performed *ex-situ* in a synchrotron.

Dragnevski *et al.* [73] argued that under most conditions encountered within solidification processing, the likelihood of dendrites experiencing mechanical damage due to flow of the parent melt is remote. However, they also observed that during the processing of undercooled melts, the conditions of both very fine dendrites and high flow velocities required to initiate such damage may exist using Cu-O and Cu-3 wt.%Sn alloy systems.

Though there has been limited work to study the deformation of dendritic structures under stress, a number of studies have been done of semi-solid deformation in general. The results from studies on non-dendritic structures can be useful to understand the mechanisms which are applicable in such conditions. From their study on semi-solid deformation of non-dendritic structures, Chen *et al.* [74] concluded that semi-solid deformation occurs due to the following four mechanisms - liquid flow, flow of liquid along with solid particles, sliding between solid particles and plastic deformation of solid particles. With increase in solid fraction and the deformation rate, sliding and plastic deformation become more dominant.

Ferrante *et al.* [70] compared the rheology and mechanical properties of the AA2024 alloy and a laboratory prepared Al-4 wt.%Cu alloy. They did simple compression tests on both materials at elevated temperature to study their stress response characteristics. The results of this study are important as a base for the high temperature response of Al-alloy as a function of fraction solid. On the basis of the results in Figure 2.17, they observed that:

1. The two alloys exhibit very similar peak stress.

2. They concluded that the solid skeleton of the one alloy must possess higher intrinsic resistance to deformation than the other since its solid fraction is different at the same temperature.

The above conclusions suggest that in the semi-solid state, for a given fraction solid, the strength of the solid skeleton does not vary by much. Therefore, a parametric study on the semi-solid deformation behaviour should be applicable

to other alloy with same primary phase.

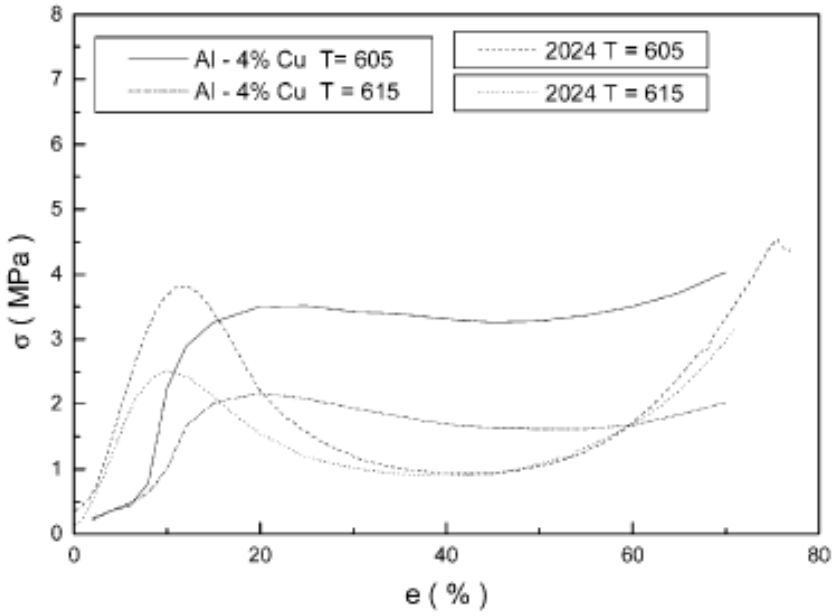


Figure 2.17: Stress-deformation curves of a 2024 and Al-4 wt.%Cu alloys under same temperature and strain-rate conditions. After Ferrante *et al.* [70].

Deformation of solid materials or bulk material can be observed and understood with the help of experiments and are therefore, easier to model. In case of semi-solid material, where the structure is not static and is a continuously changing form, the models have to be based on simplified numerical expressions. Though, the behaviour of the semi-solid material can be predicted with a fair accuracy, the lack of understanding of the microstructural changes and interaction of the liquid and solid phase, act as hurdles in modelling techniques.

The studies done by Pilling [67] and later by Vieira *et al.* [75] are more relevant to the present study as they discuss the effect of the flow of interdendritic liquid on the segregation susceptibility and stresses on dendritic arms. The interdendritic flow rate, which they found to be as high as 10 mm/s, could result in the

mechanical deformation of the dendrites. In their analysis, they estimated the stresses at the root of the secondary dendrites due to the fluid flow around it. They argued that the narrow neck around the root of the secondary arm was the most susceptible to any possible deformation. Their results showed that the stress in a dendrite arm will always lie below that for plastic flow and that the response to the interdendritic fluid flow will only be elastic. One of the main inferences out of their studies was that the interdendritic fluid flow does not cause dendrite fragmentation but aids in the transport of dendrite fragments which have already formed by other mechanisms. Though, on the basis of solidification science, it can be argued that interdendritic does enhance fragmentation in dendrites as local remelting occurs at high curvature locations (such as roots of secondary dendrites).

2.3.2 Direct finite element modelling

With the improvement in computing capabilities, FEM techniques have become increasingly efficient. This has allowed microstructure based FEM to flourish as the individual effect of grain size orientation [76, 77] or effect of different phases [78], etc could be quantifed. The findings from these micro-mechanical models can then be scaled to macro-scale models [79]. One method which has been successful in predicting the bulk behaviour of materials with complex internal microstructure is the direct finite element (DFEM) method. Unlike micro-mechanical models where an approximate geometry is used [79, 80], this technique uses real image data (micrographs, tomographs) where each phase is individually meshed and the flow stress of that constituent is used as input. The entire ensemble of different geometries and phases is then deformed together computationally, to predict the behavior of the heterogeneous material. The geometries used to create the meshes for direct finite element modelling (DFEM) have been generated by a number of methods including microtomography [10, 20, 81–85]. For example, this methodology was successfully employed to understand mechanical behaviour of composites and alloys and the fatigue behaviour of cast aluminium alloys [86–89]. Another method of generating the meshes is Voronoi

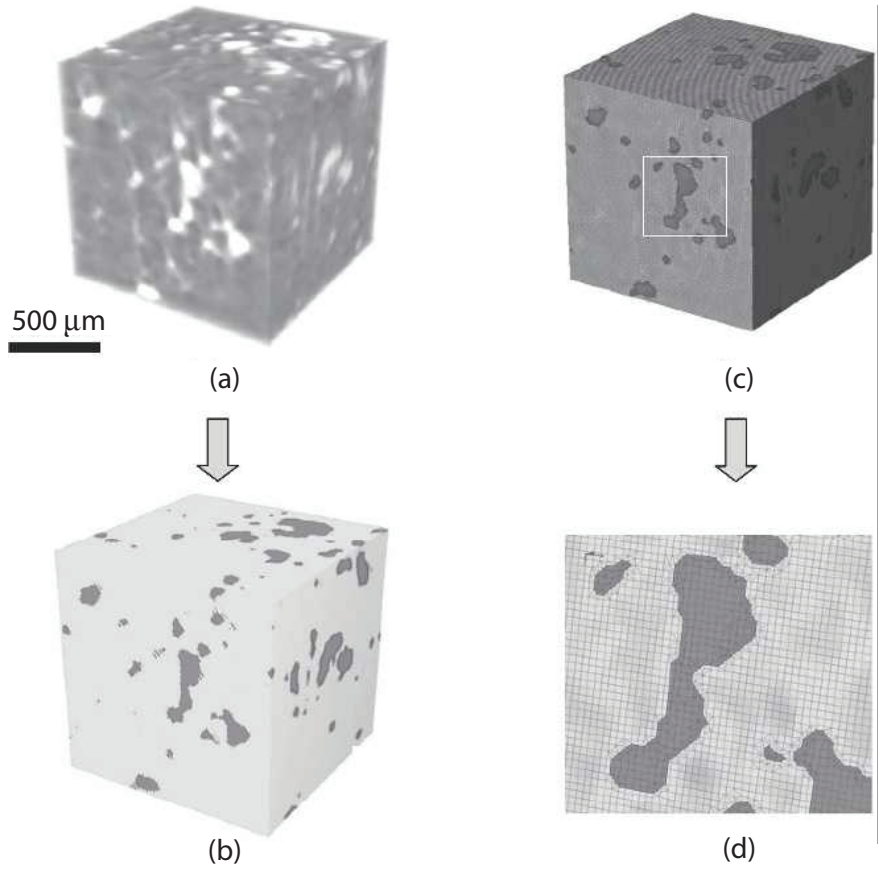


Figure 2.18: Segmentation and meshing: (a) original tomogram, (b) segmented data, (c) meshed data, and (d) close-up of mesh at interface in case of a metal matrix composite. After Watson *et al.* [81].

tesselation [90–93]; however, only one author [94] has used this technique to determine the flow stress behaviour in the case of semi-solid alloys and this study was limited to 2D near globular grain shapes.

To employ DFEM successfully, the material properties of each phase need to be accurately known. A number of experimental studies have been performed to derive accurate properties of individual phases using high temperature mechanical testing [70, 95–97]. Based on such experiments, mathematical models have been presented which mainly include the deformation of the bulk solid in rela-

tion to the viscous interdendritic liquid in the channels [65, 98–100]. A common approach to understand this problem has been to study the semi-solid structure as a porous media saturated with a viscous liquid [101] or to model the thermo-mechanical behaviour at high temperature [102, 103]. This has led to a number of formulations that have been used in finite element models [104]. The interaction of the liquid and the solid occurs at a microstructural scale and that is where recent studies have focused both in tension and compression [73, 93, 105–107]. However, the models in the literature are designed for specific alloys and are difficult to apply to other alloy systems.

2.3.3 Summary

The deformation of Al-alloys under stress and its correlation with the flow of the interdendritic liquid is still not well understood. The models present in the literature are relatively simple due to the complexity of the mechanisms involved. The application of finite element modelling (FEM) to the microstructures [81, 87, 108] is an attractive technique to understand the deformation behaviour in microstructural scale. A complete macro-model which could relate the macro-deformation of the semi-solid with deformation of micro-structure and convection is absent.

2.4 X-ray microtomography

X-ray microtomography (XMT) is a non-destructive, three-dimensional characterisation method that has been applied in a number of fields within materials science including the characterisation of dendritic microstructures [10, 20, 34, 50, 82, 83, 108–114]. During an XMT analysis, internal microstructural features are distinguished by measuring the intensity of a transmitted x-ray beam whilst the specimen is rotated. The resultant absorption maps (projections) are then used to reconstruct a 3D representation of the material structure. The most common reconstruction method is based on the inverse radon transform and is generally referred to as the filtered back-projection method [86].

There are two important types of x-ray source which are used in modern x-ray microtomography [115]; the synchrotron ("parallel beam" - Figure 2.19(c)) radiation source and divergent ("cone beam") laboratory sources (Figure 2.19(d)). Synchrotron radiation offers many advantages over laboratory sources, most notably:

- A very high intensity which yields a high signal-to-noise ratio in a short time step;
- The beam can be made monochromatic very easily, allowing spatially resolved elemental maps of a material to be obtained;
- The beam is parallel, which eliminates many imaging artifacts.

However, the number of synchrotron sources around the world is limited and when available, the time windows tend to be very tight. Compared to that, a laboratory x-ray source provides a more accessible and cheaper option to a synchrotron. The increased interest in laboratory XMT has seen a number of commercial companies providing turn-key laboratory XMT systems, most notably Phoenix x-ray Systems and Services GmbH (Germany), X-Tek Systems Ltd (UK) and SkyScan (Belgium). Recently, Xradia (USA) have developed high resolution (sub 60 nm) tomography capabilities with improvements in optical design which has increased

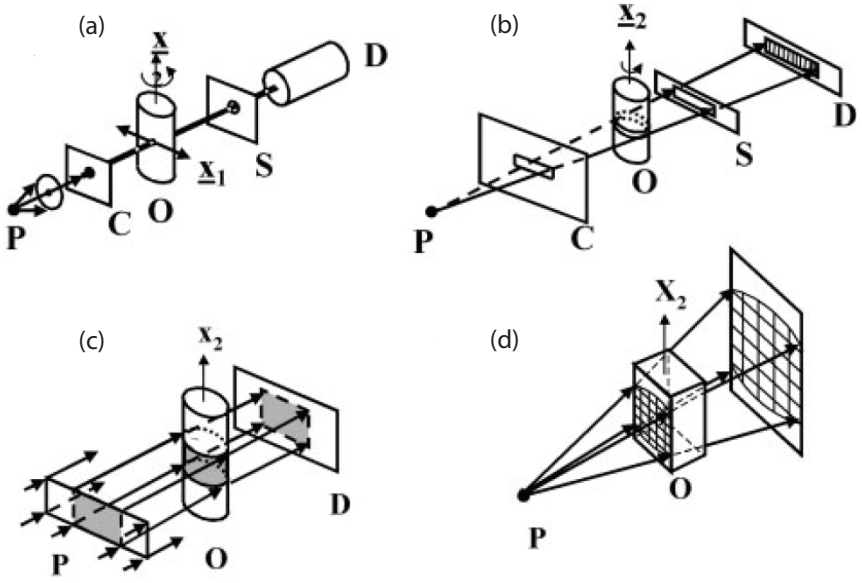


Figure 2.19: Schematic of tomography technique with (a) pencil-beam, (b) fan-beam, (c) parallel beam and (d) cone-beam [115].

the range of effectiveness of laboratory sources.

When x-rays are passed through a material, the photons entering the material are either absorbed or scattered. The extent of this absorption or deviation of the x-ray beam depends not only on the energy of the photons, but also on the atomic structure of the material. In the case of a monochromatic source, if N photons enter the material, then the number of photons exiting is given by [116]:

$$N(x) = N_0.e^{-\mu_0.x} \tag{2.14}$$

where, μ_0 is the attenuation coefficient of a homogeneous material. For a multiphase material, μ_0 is also a function of position. This x-ray beam attenuation coefficient is a function of photon absorption by the atoms of the material (the photoelectric effect), and photon deflection from their original direction of travel (Compton scattering) [117].

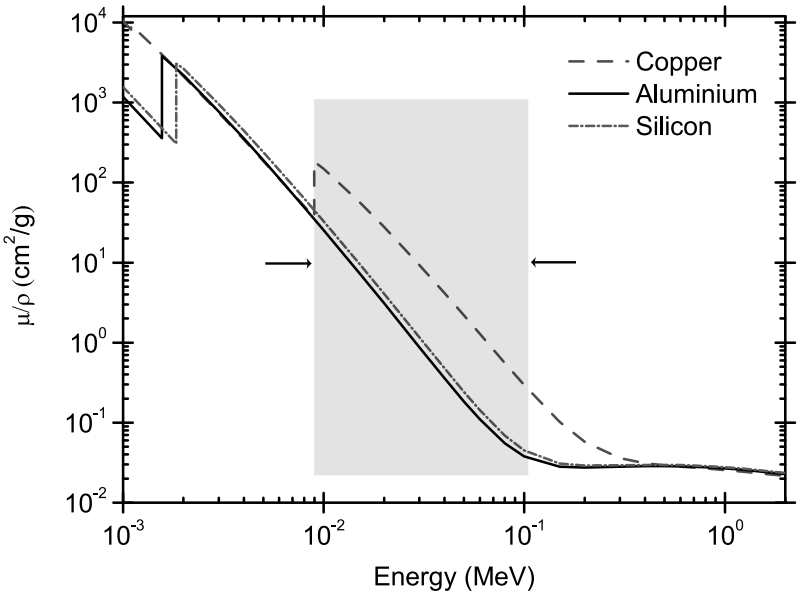


Figure 2.20: Attenuation coefficients of aluminium, copper and silicon as a function of photon energy and the range of energies which can be effectively used for Al-Cu alloys in tomography [118].

Photoelectric absorption is proportional to W^n (where n = 4-5), whereas Compton scattering is proportional to W (W being the atomic number of an atom in the attenuating medium). Since the photoelectric effect is the dominant interaction at low x-ray energies (<100 keV), low energy x-rays are more sensitive to compositional variation than higher energy x-rays [36, 84].

2.4.1 Limitations of XMT

Laboratory XMT has a number of limitations, most of which are a consequence of the white (polychromatic) x-ray source. For example, it is not possible to derive true compositional information unless proper calibration using x-ray photons is conducted, to account for the non-linear attenuation of the polychromatic beam.

The low photon flux of a laboratory source (compared with a synchrotron source) also places certain limitations on the user. High resolution imaging re-

quires a beam spot size smaller than the voxel size. Clearly, as the spot size is reduced, so is the number of available photons, increasing the signal-to-noise ratio. If the voxel size (i.e. spatial resolution) is increased, such that it is comparable in size to the microstructural features of interest, then partial volume effects become significant.

Streaking is an artifact which can result when a phase occupies only part of the x-ray beam measured by a single detector element. Before reconstruction, the x-ray intensity measurements are converted into attenuation measurements by taking the logarithm. If a phase intercepts part of an x-ray beam path, the measured intensity will be the average of the intensity over the x-ray path, and the resulting attenuation measurement (the logarithm of the average intensity) is not the same as the average attenuation over the x-ray path. This discrepancy results in streak artifacts that occur tangential to object detail with sharp attenuation transitions [116].

Other artifacts which occur in the laboratory XMTs are beam hardening artifacts, ring artifacts and hot points [116].

2.4.2 Summary

For the study of Al-Cu alloys, XMTs can provide high resolution ($\approx 4\,\mu m$ in laboratory units, $\approx 1\,\mu m$ in synchrotron sources) imaging of the microstructure in 3D. The presence of a laboratory x-ray source and reconstruction facility within Imperial College London provides an excellent advantage to characterise Al-Cu microstructures. The limitations of laboratory XMT sources are highlighted when Al-Si alloys are used owing to insignificant difference between the attenuation of Al and Si (Figure 2.20). Therefore, in the scope of present work, only Al-Cu alloys have been used. Within Al-Cu alloys, a higher solute content is desirable to easily resolve the phase contrast between the dendritic and the interdendritic phase.

Chapter 3

Permeability measurements and viability of combining XMT/FEM to estimate flow stress in semi-solids

3.1 Introduction

Twin roll casting (TRC) has been used for more than 50 years and is a popular method to cast sheets of narrow freezing range aluminium alloys up to 6 mm in thickness. One of the major challenges when twin-roll casting aluminium sheet is consistently achieving good physical and mechanical properties at the high speeds required for productivity. In TRC, heat is extracted through the rolls whilst pressure is applied. This results in solidification starting at the layer which is in contact with the rolls and converging towards the centre. The solute enriched liquid in the mushy zone is the last to solidify and is squeezed towards the centre line, forming pockets of centreline segregate. To simulate the formation of these

A version of this chapter has been previously published. Fuloria, D., Lee, P. D. and Bernard, D. (2008), Materials Science and Engineering A, **494**, p3

segregates the flow of interdendritic liquid in the semi-solid region and the deformation of the semi-solid structure must be quantified.

3.1.1 Flow of interdendritic liquid

The fluid motion through a dendritic structure is often treated as porous media flow and Darcy's law (Equation 2.5) is applied to estimate the pressure drop in the flow channels [46].

A number of prior authors have experimentally measured permeability in the semi-solid region. Various designs of permeameters exist in the literature but the basic principle behind most of them is the same - when a pressure difference is applied over the mushy zone and the resulting superficial velocity of the liquid calculated, permeability can be measured [37, 38, 45–47, 119]. But due to the time evolution of the solid-liquid interfaces and the oxidation of the liquid in the permeameter, these experiments were not very accurate. For Al-Cu alloys, a significant coarsening was observed during the experiments [37, 39].

For the accurate measurement of permeability, the information about the internal structure has to be precise. The experiments fail in this particular aspect. The usage of XMT [10, 20, 34, 50, 83, 111–114] to capture the structure provides actual information about the state of the structure and thus provides a more accurate structure upon which flow simulations can be performed.

In this chapter, interdendritic fluid flow has been measured in columnar dendritic structures in Al-12 wt.%Cu alloy. To generate the structures, alloy samples were directionally solidified using an x-ray temperature gradient stage (XTGS) and a quenching directional solidification (QDS) furnace. While alloy casting in XTGS was performed *in situ* a laboratory x-ray unit for the initial samples, it was conducted *ex situ* in the QDS owing to the ease of operation. The columnar structure of directionally solidified samples was then quantified in 3D using XMT. A fluid flow solver was on the virtual 3D samples to simulate interdendritic fluid

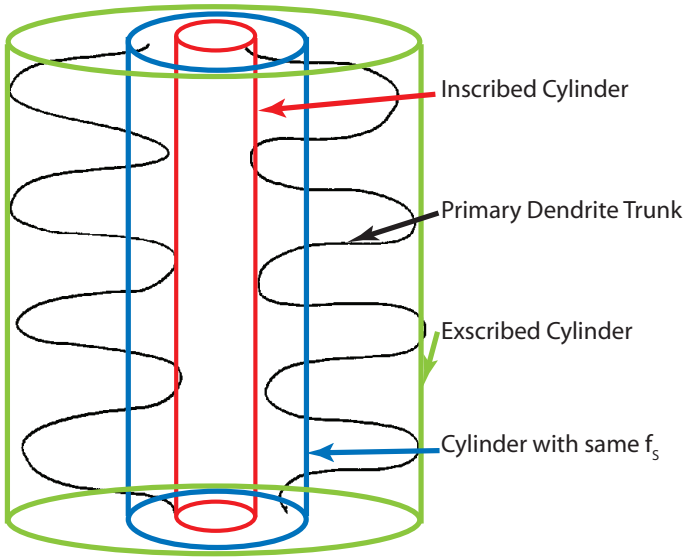


Figure 3.1: Schematic showing the cylinders used for dendrite shape approximation.

flow through the complicated structure and the permeability was measured.

3.1.2 Deformation of dendrite

The other important factor which affects the formation of defects during TRC is the deformation of the semi-solid. Most simulations of the semi-solid region approximate the flow behaviour either using a flow stress that linearly decreases as a function of increasing temperature (T), or apply the fraction solid (f_s) as a multiplicative factor. To determine if these approximations are appropriate, finite element (FE) simulations were performed on sub-volumes (or representative volume element, RVEs) of the segmented dendrites. The final goal of such a methodology would be to determine the appropriate size of RVEs required and then to fit constitutive equations to the calculated flow stresses as a function of either temperature or fraction solid for use in macro models of the entire twin roll caster.

In this chapter, preliminary simulations to demonstrate meshing and simulation procedures were performed. The primary dendrite was sub-sampled at two locations (or f_s). The first volume was located close to the tip of the dendrite and the second volume was situated a little further down in the mushy zone. The methodology, if viable, could be extended across the whole range of f_s values in columnar structures to derive the constitutive semi-solid deformation behaviour of Al-Cu alloys.

The standard approximations to relate the change in flow stress in the semi-solid to T / f_s are to either make the flow stress linearly decrease with increasing T or to multiply by the fraction solid. The behaviour of the true geometry of the dendrite was compared to these approximations, together with cylinders of: (a) equal fraction solid; (b) inscribed, i.e. the largest cylinder with only solid in it or primary trunk; and (c) circumscribed or bounding, i.e. the smallest cylinder with no solid outside (Figure 3.1). Cylinders (b) and (c) provide the zone boundary for the deformation behaviour of the dendrite. But the cylinder with an equivalent diameter based on the equality of volume fraction solid is the only simplification with a physical basis. Identical compression was applied in each simulation. The comparisons between the deformation of the dendrite and the cylinders in the RVEs are discussed.

3.2 Methods

3.2.1 Direction solidification experiments - XTGS

A previously developed two-zone furnace called the XTGS was used for the *in situ* observation of as-cast aluminium solidification. The unit was originally developed by Lee [6, 8], and was adapted for use in this experiment. The XTGS provided controlled solidification while placed inside the XMT machine for observation. This is similar to the real time observation of solidification in synchrotron units [120, 121].

Molten aluminium was cast into a thin boron nitride crucible or boat through a refractory pouring basin. Once filled, the pouring basin was removed and replaced by a thermal insulation blanket. The boat was then lowered through a temperature gradient zone produced by a 'hot zone' and 'cold zone' in the XTGS. The temperature gradient induced a controlled solidification of the aluminium. *In situ* observation during this process was achieved through a small viewing window cut into the front and back of the apparatus.

The real time x-ray imaging is done using a commercial XMT unit[1] in the transmission mode with 80 kV, 200 μA setting. The images were recorded in a digital detector at the rate of one frame per 200 ms. The main components of the XTGS are the boat, the hot and cold zones, the insulation materials, and the DC motor.

Boat: The two part design of the boron nitride boat ($210 \times 45 \times 8\,\text{mm}^3$ in size) allowed for the cast aluminium to be removed at the conclusion of each experiment. The boat was held to a track by two inserted pins. The top portion of the boat was cut deeper to act as a pouring basin for the molten aluminium. The pouring basin opening was 5 mm × 25 mm and 25 mm deep before the boat blended back to 1 mm in thickness.

[1] Phoenix—x-ray Systems and Services GmbH, Wunstorf, Germany

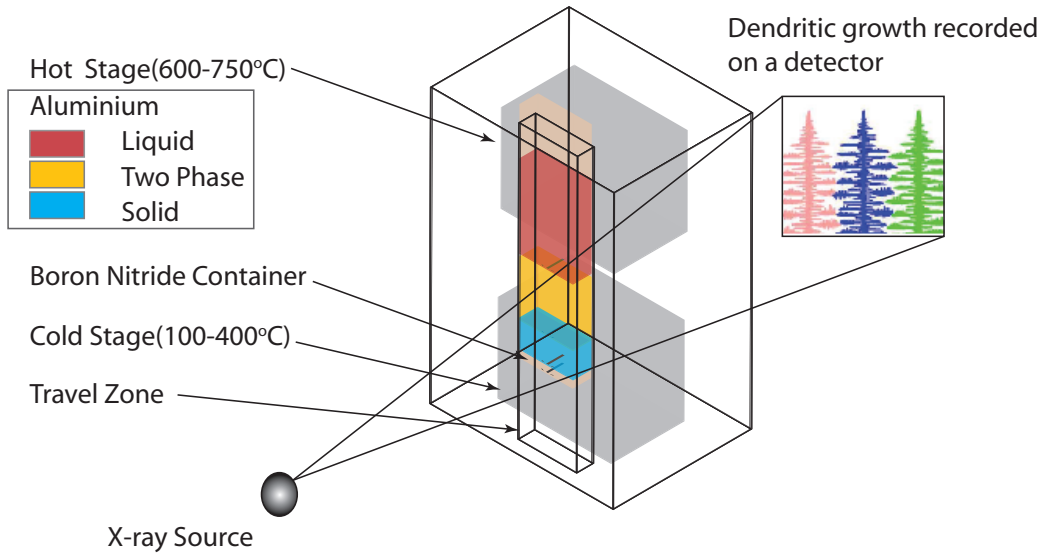


Figure 3.2: Schematic of the XTGS apparatus. Liquid alloy is directionally solidified and the growth of solidification front is captured on digital detector. The motion of the boron nitride container is controlled so as to track the solidification front at all times.

Hot and Cold Zones: The temperature gradient that the boat passed through was created by a 'hot zone' and a 'cold zone' (see Figure 3.2) separated vertically by a distance of 25 mm. The hot zone consisted of a silver block heated to 700 °C, while the cold zone consisted of a copper block heated to 500 °C. The separation of the blocks also acted as a viewing window for x-ray transmissions to pass through the sample. The spacing between the blocks and the boat was at a minimum providing maximum heat transfer to the boat. The hot and cold zones were monitored by K-type thermocouples, and the temperature ranges maintained by a temperature control box. Thermocouples were also placed inside the casting cavity through grooves cut on to the sides of the boat and placed 20 mm apart.

Insulation: Heat from the molten aluminium and the heaters inside the XTGS was contained within the apparatus with the use of several insulation materials. Surrounding the internal components of the XTGS were pieces of refractory board, wool insulation and a specially constructed thermal blan-

ket that lined the front cover. A thermal insulation blanket constructed of wool insulation was also placed over the top of the XTGS after the removal of the pouring basin.

DC Motor and Track Speed: The boat and track assembly was moved by a cogwheel that pulled the pinion track downwards through the temperature gradient. The speed of the pinion track was controlled by the voltage supplied to the DC motor that drove the cogwheel. For this casting, the track speed was kept constant at 0.44 mm/s.

Sample preparation for XMT: Specimens for tomography were in the form of cuboids with a cross sectional dimensioning of $2 \times 2 \times 20\,\mathrm{mm}^3$. These samples were cut from the thin strip of Al-12 wt%Cu which was directionally solidified in the XTGS. For the identification of the best region to cut out small volumes, the thin strip was mounted back on the XMT for transmission images. Regions with best features are marked and subsequently made into small samples for three dimensional reconstructions.

The casting of samples in XTGS provided excellent control of temperature gradient and growth velocity and real time image feedback of actual solidification dynamics. The real time images (see Figure 3.3) are helpful in analysing the nucleation and the growth events for porosity [8] and its subsequent modelling [9]. In the present study, the columnar dendritic structures were quantified in 3D using XMT. One disadvantage of XTGS samples was that the structure was fully grown and it was impossible to analyse the dendrite tips or the semi-solid material.

3.2.2 Directional solidification experiments - QDS

For growing the columnar structure in the Al-12 wt.%Cu alloy, cylindrical samples (ingots) of the alloy were used. The dimensions of the ingot were decided on the basis of the size of the alumina tube. The alumina tube, which acts as a mould for the melting, has an outer diameter of 9 mm and an inner diameter of 6 mm. To allow the ingot to be placed smoothly inside the mould, a diameter of 5.5 mm was chosen. Cylindrical alloy samples were sectioned using EDM. The length of

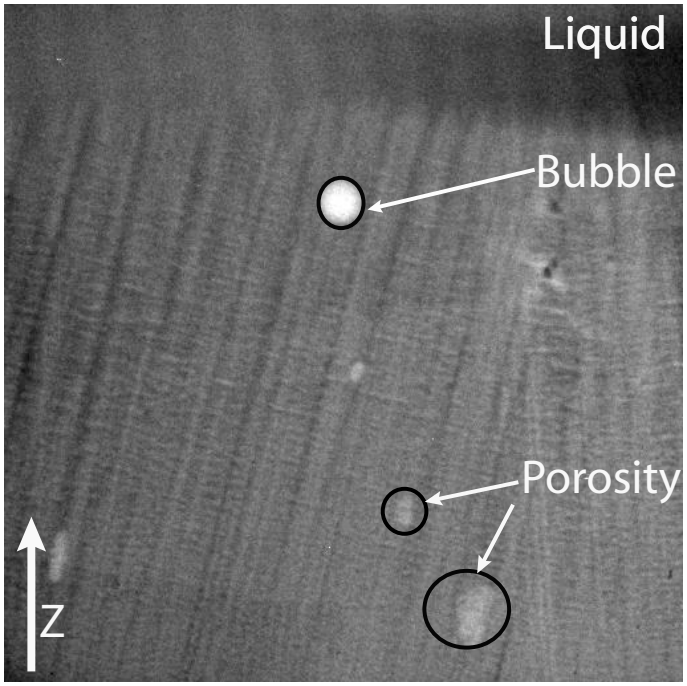


Figure 3.3: XTGS radiography image showing the growth of columnar dendritic front and the presence of porosity and bubbles.

each cylindrical ingot is 70 mm.

To grow a columnar structure for studying the permeability of Al-12wt%Cu, directional solidification experiments were carried out in a Bridgman furnace as shown in Figure 3.4. The heating of the sample was established by coupling a high frequency field from a primary induction coil into a graphite susceptor. The graphite susceptor takes the role of the secondary coil which helps by providing a high temperature jacket around the sample and thereby reducing the gradient between the centre and the edge of the sample. The outer diameter of the graphite susceptor is 25 mm and its inner diameter is 22 mm. The high frequency generator has an output power of 3.3 kW and generates a primary coil signal of 450 kHz and 415 V. Glass tubes insulate the system from the environment and water flows through them and the system lid to keep them at a constant temperature to avoid thermal stresses. The insulation brick protects the glass tubes from direct heat radiation of the graphite susceptor and reduces the radial heat

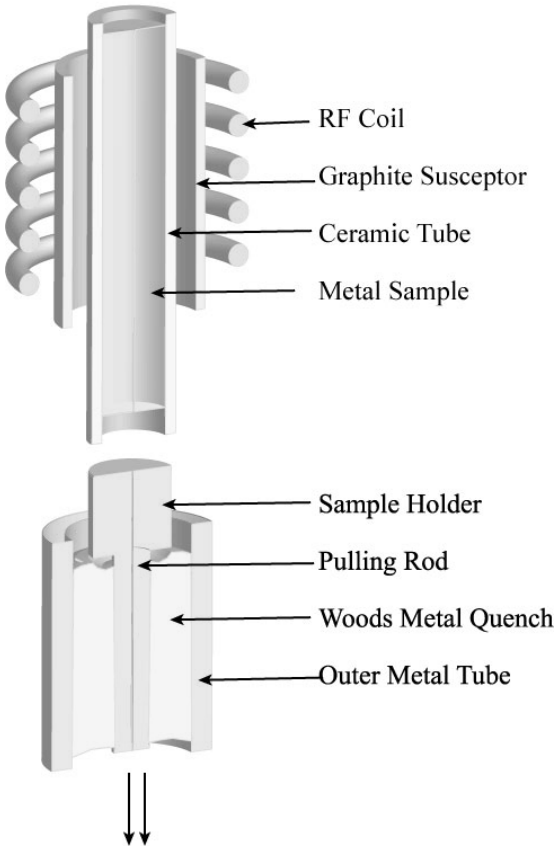


Figure 3.4: Schematic diagram of the solidification rig used for the quenched directionally solidified samples of Al-12 wt.%Cu.

flow. An inert gas atmosphere is established inside the glass tube by a constant flow of argon gas. The argon gas flow is controlled with the help of a gas flow indicator. The gas inlet is positioned at the bottom lid of the rig and the outlet at the top lid. A mould of recrystallised alumina contains the ingot which was fixed to the withdrawal rod.

A separate water supply flows through the hollow withdrawal rod, the chill and the bottom lid to keep them at a constant temperature. The chill used in these experiments contains a Woods metal substitute, which has a melting point of 75 °C, for the purpose of enhanced cooling and subsequent quenching of the ingot. The Woods metal substitute is kept molten with a hot water supply through

the external sleeve. The flow of the hot water is maintained using a pump with a heater. The withdrawal unit has a motor that withdraws the ingot during the experiments through the hot zone of the susceptor. The range of possible withdrawal rates ranges from 275 μm/sec to 0.03 μm/sec. For the present study, the sample was withdrawn at a rate of 250 μm/sec. A hole in the top lid allows the introduction of a thermocouple.

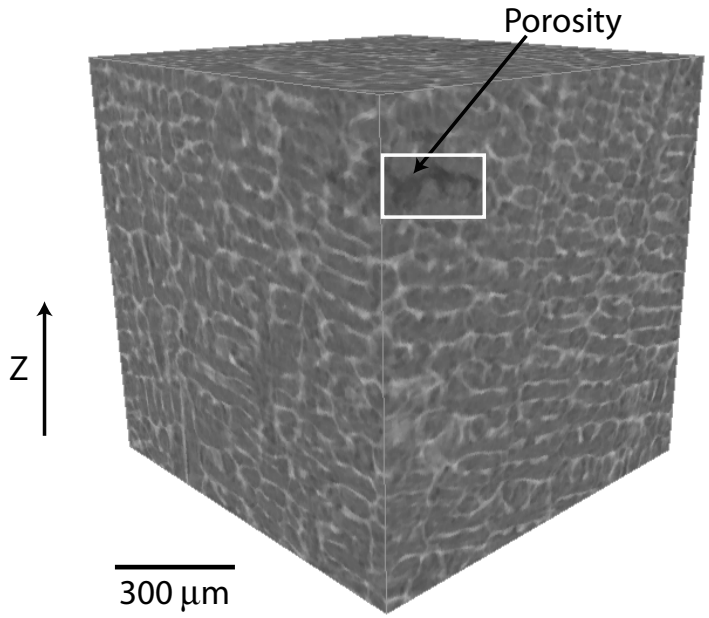
Fifteen minutes after the generator was switched on, the temperature of the metal becomes stable at 880 °C. The motor of the pulling rod is turned on at this moment and the sample is withdrawn from the hot zone. When more than half of the sample is removed from the hot zone, the rod is subjected to a quench (Woods metal substitute).

3.2.3 XMT and image analysis

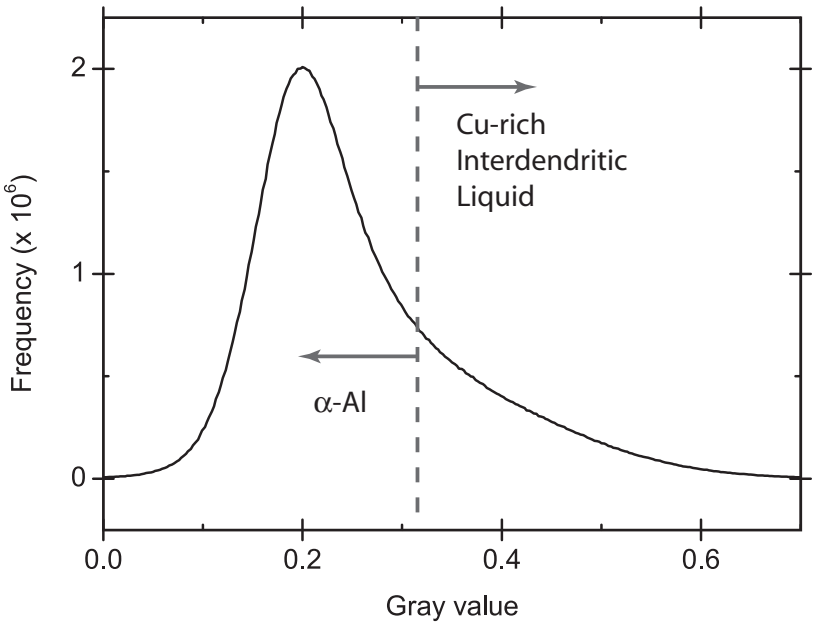
An Al-12 wt%Cu alloy was selected to provide a favourable differentiation in the x-ray attenuation coefficients of the dendrite composition and that of the interdendritic region [8]. The directionally solidified samples from XTGS (1 mm × 1 mm cross-section and long in the direction of columnar growth) and quenched samples from the Bridgman furnace (cylinder of 6 mm diameter and 60 mm in length) were scanned in a commercial XMT[1] unit . A spot size of approximately 2 μm was used with accelerating voltage of 80 kV and a current of 80 μA. Polychromatic tungsten K_α radiation was used and transmitted radiation was recorded on a two-dimensional semiconductor type direct digital detector. A voxel size of 7.2 μm was achieved.

The reconstructed volume was visualised using the commercial package Amira[2]. Figure 3.5a shows the reconstructed columnar dendrite network with the Al-dendrite appearing as the dark phase and Al-Al_2Cu interdendritic phase appearing as the lighter phase. The primary arms are aligned along the z-direction in all the tomograms. A threshold value was selected to convert the image into a

[1]Phoenix—x-ray Systems and Services GmbH, Wunstorf, Germany
[2]Mercury Computer Systems, Inc., USA. (version 4.1)



(a)



(b)

Figure 3.5: (a) A 3D tomogram of the directionally solidified Al-12 wt.%Cu sample with key microstructural features (Z is the direction of solidification) (b) Histogram showing the frequency of gray values for the 3D volume shown above and a distinct peak for the α-Al dendrite.

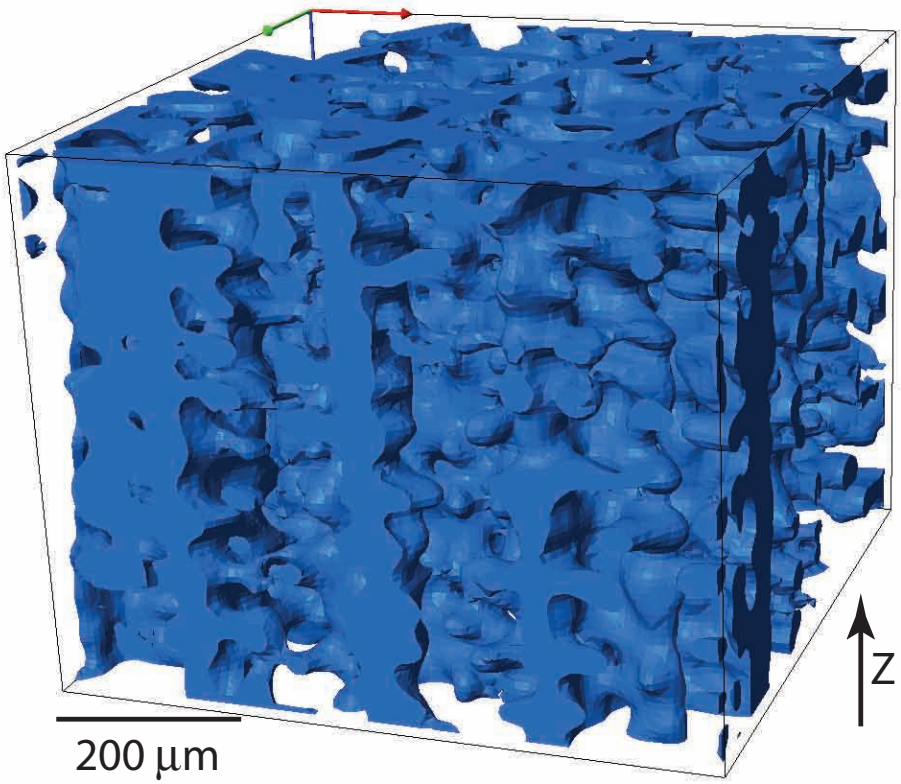


Figure 3.6: A segmented and 3D rendered image of the columnar dendritic structure derived from XMT.

binary volume with only liquid or solid cells. This value was based on the histogram, but due to a strong overlap in the peaks and hence is subjective adding an additional error (Figure 3.5b). The dendritic or the interdendritic phase can then be selectively rendered for meshing procedures (Figure 3.6).

3.2.4 Permeability

The permeability was calculated using the model developed by Bernard *et al.* [34, 122]. The model solves the generalised Stokes problem in a 3D interdendritic domain (Equation 2.5). Periodic boundary conditions were applied on the faces and permeability was measured in directions parallel and perpendicular to the

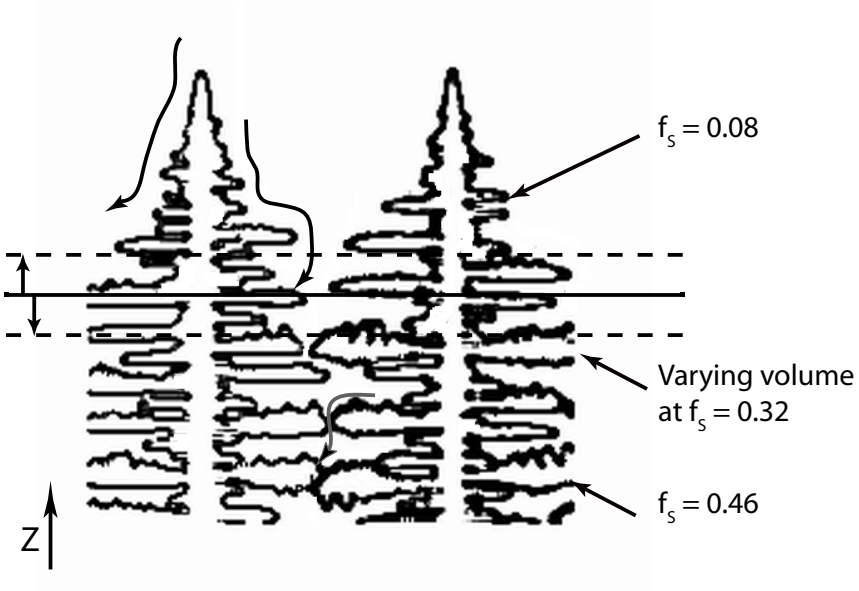


Figure 3.7: Schematic illustrating RVE selection for permeability calculation along the direction of primary dendrites.

columnar structure.

Moving average permeability at different locations - To get a better understanding of the local variations in permeability, moving average permeability values were measured at different locations along the direction of the primary arms (different values of f_s, Figure 3.7). This allows the influence of the size of the volume analysed to be determined by growing the region, centred at the same slice (Figure 3.7).

Measurements in a fully grown columnar structure - The measurement of permeability close to the tips gives an indication about how the ease of flow of interdendritic liquid varies as we move from the dendrite tips into the mushy zone. The anisotropy in the flow properties becomes more distinct as we go deeper in the mushy zone. Permeability simulations were performed on directionally solidified Al-12 wt.%Cu castings.

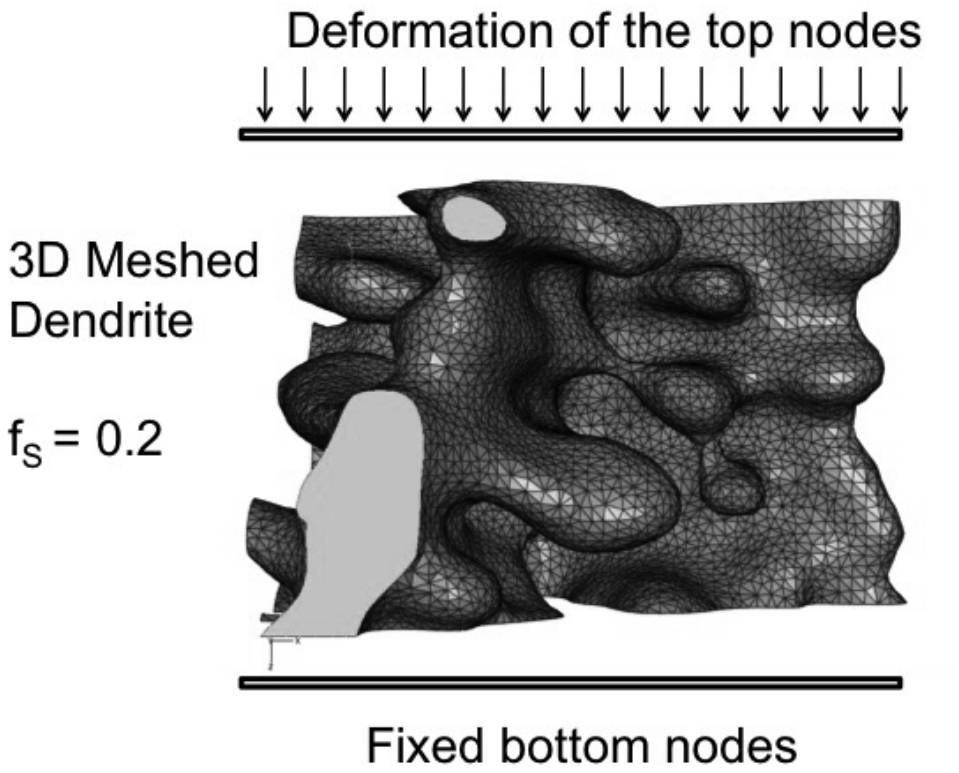


Figure 3.8: Schematic showing the meshing of the dendrite and the boundary conditions for FE simulations.

3.2.5 FE modelling for deformation

For deformation modelling, the binarised quenched Al-12 wt.%Cu sample was divided into two parts along the length of the primary. The two sections (or RVEs) of the dendrite were separately meshed using the commercial meshing software ScanFE[1] . The deformation behaviour of each meshed RVE was simulated using ABAQUS[2] by applying a compressive displacement of 25 μm at the top face (which translates into $\epsilon \approx 0.1$) and fixing the bottom face (Figure 3.8). For this preliminary study, the dendrites were assumed to have the properties of aluminium matrix material [81], i.e. a Young's modulus of 73 GPa and Poisson's

[1] Simpleware, Exeter, U.K.
[2] ABAQUS UK Ltd.

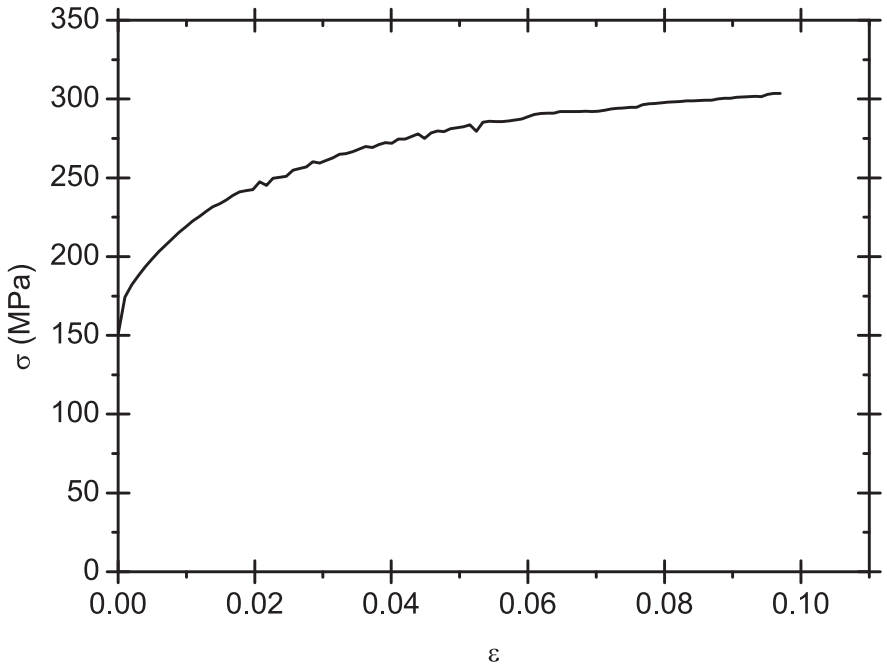


Figure 3.9: Plastic deformation curve for aluminium as used in simulations by Watson [81].

ratio of 0.33. The plastic deformation curve used for material property is shown in Figure 3.9.

3.3 Results and discussion

3.3.1 Permeability

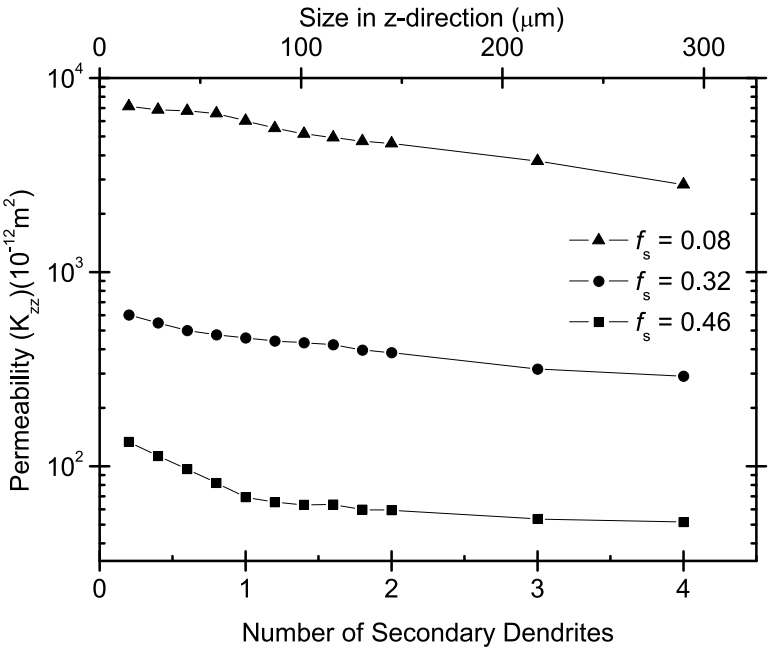
Flow simulations were performed in three distinct regions of the columnar dendritic structure: (i) at the bottom of the primary dendrite trunks ($f_s = 0.46$); (ii) in the middle ($f_s = 0.32$); and (iii) at the tip ($f_s = 0.08$).

The first study performed was the sensitivity of the permeability to the size of the RVE in the z-direction. The values for all the major components of the permeability tensor, i.e. K_{xx}, K_{yy}, K_{zz} (where x, y, z are as defined in Figure 3.7; effect of all other components is negligible) are analysed at three different locations as mentioned above. K_{zz} denotes the permeability of the structure along the direction of primary dendrites, whilst K_n (avg. [K_{xx}, K_{yy}]) denotes it in a direction normal to the primary dendrites.

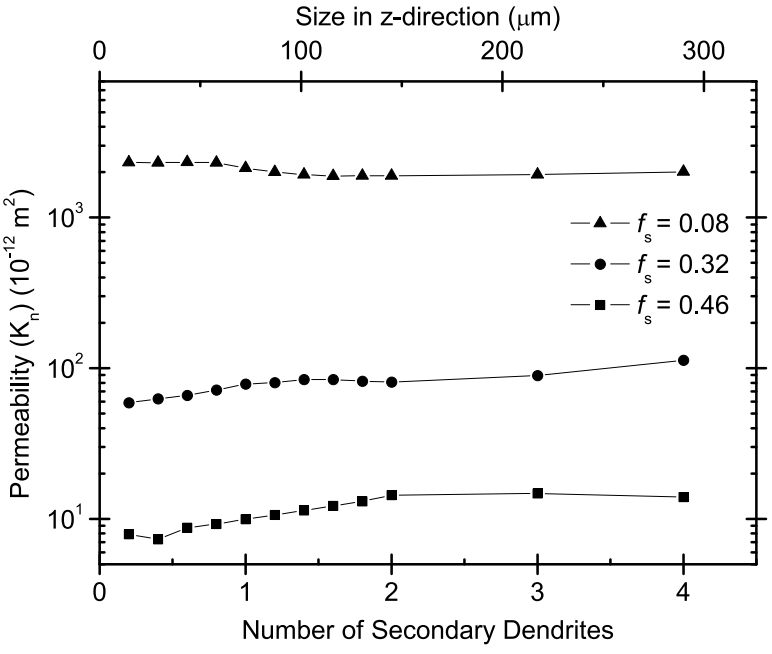
$$K = \begin{bmatrix} K_{xx} & 0 & 0 \\ 0 & K_{yy} & 0 \\ 0 & 0 & K_{zz} \end{bmatrix} \tag{3.1}$$

K_{zz}, at all three locations as defined above, decreases and stabilises monotonically with increasing number of analysed z-slices (or secondary arm spacing, λ_2) (Figure 3.10a). Along the dendrite, the value for K_{zz} decreases as the size of the volume is increased. This is due to addition of more solid with increasing volume. This is true for the other two locations as well but the effect is much less pronounced. For the flow parallel to the primaries, the region of minimum cross-sectional area open to flow dominates - i.e. the secondaries at the bottom of the volume restrict the flow rate. Therefore, K_{zz} decreases slowly with increasing RVE size.

The component of the permeability tensor perpendicular to the primary dendrites, K_n, increases to a constant value (Figure 3.10b). The plateau is at about $2\,\lambda_2$, showing that at least two secondaries need to be included to obtain typical results. However, as more volume nearer to the tips (lower f_s) is included, there is less restriction in flow perpendicular to the primaries and hence the values for



(a)



(b)

Figure 3.10: Moving average value of local permeability at (a) parallel to the dendrite arms, (b) perpendicular to the dendrite arms (Figure 3.7). Note secondary arm spacing is approximately 72 μm.

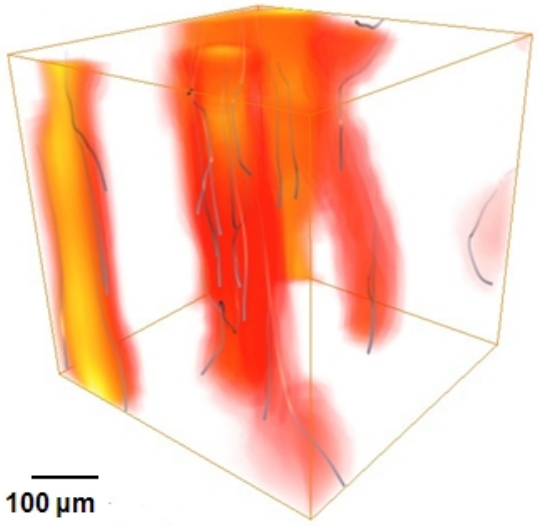
K_n start to increase.

It should also be noted that the perpendicular component, K_n, is much lower than K_{zz}, or the flow parallel to the primary arms is easier. This indicates that the secondary arms provide a more tortuous path, matching experimental measurements [123]. Also, at the dendrite tips ($f_\mathrm{s} = 0.08$), the fraction solid is so low that the drag on the very slim primary dendrite trunks is the main restriction to flow. As the volume is increased, the trunk stays constant at the top but widens slightly at the bottom, causing a slight decrease in all components of the permeability tensor.

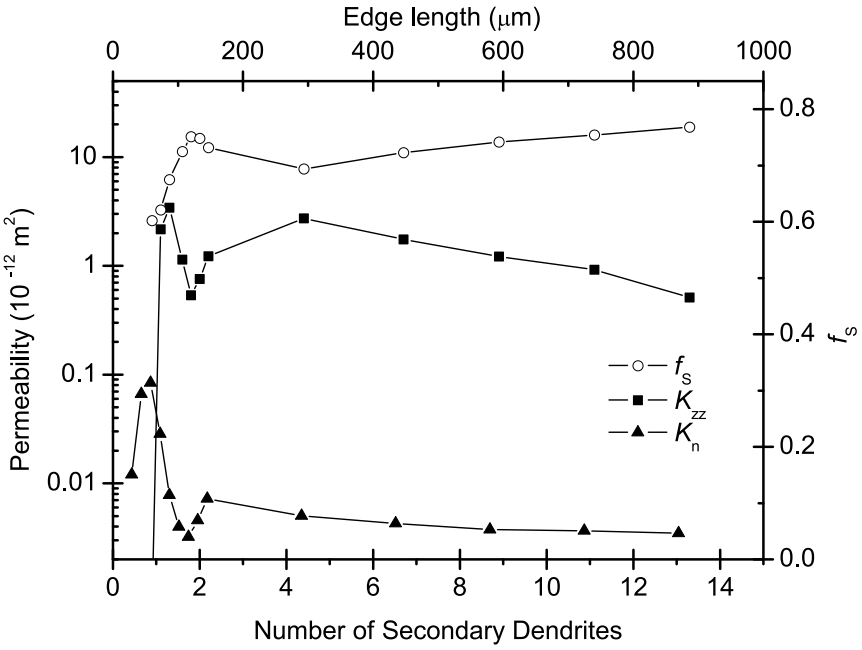
In summary, this preliminary study suggests that the RVE must include at least 2 secondaries. Increasing the size beyond this shows a stable change in predicted permeability; however, this rapidly changing RVE now includes regions which are very different from the centre of the volume. Further experiments/computations are required to determine the trade off between too small a volume and including structures which are not typical of the central f_s value. One solution might be to significantly grow the volume in the $x - y$ directions; however more experiments are required to obtain a larger number of primaries to allow this.

A second study was performed on a fully grown columnar dendrite structure to establish the RVE size required for a structure which is not changing with z. A volume of 200 × 200 × 200 voxels, 7.2 µm resolution, was selected as being sufficiently large based on the work done by Bernard *et al.* [10]. The simulations were then performed on the subsets of this volume, all centred on the centroid of the maximum volume. Starting with only 2 × 2 × 2 voxels, the size was increased in 12 additional steps until the full size was reached.

Typical results from one of the calculations are shown visually in Figure 3.11a for a 50^3 voxel volume, where the streak lines are rendered together with velocity magnitude when a pressure drop is applied across the z-direction. The quantified results are shown in Figure 3.11b. All components of the permeability tensor



(a)



(b)

Figure 3.11: (a) Flow channels in a direction parallel to primary dendrites. (b) Permeability values from the simulations as a function of edge length of the cubic volume and number of secondary dendrite arms.

Table 3.1: Permeability values from present study as compared to other numerical models and to the experimental data

Sample	f_s	Source	$S_V(m^2)$	$K_{ZZ}(\times 10^{-12} m^2)$	$K_n(\times 10^{-12} m^2)$	$K.S_V^2$
Al-12 wt.%Cu	0.742	Present Study	34387	3.1	1.21	0.0037
		Blake-Kozeny[46]		3.16	0.97	
		Poirier[46]		3	0.55	
Al-12 wt.%Cu	0.768	Present Study	31432	2.72	0.51	0.0027
		Blake-Kozeny[46]		2.83	0.69	
		Poirier[46]		2.43	0.38	
Al-13.1 wt.%Cu	0.71	Bernard-Nielsen[34]	52000	2.2		0.0059
(Equi-axed)	0.738	Nielsen-Arnberg[37]	63956	1.9		0.0078

stabilise after an edge length of $\sim$ 400 μm or 4-6 secondary dendrites ($\lambda_2 =$ 65 μm). Hence, in the final structure the edge length of an appropriate RVE should ideally be about 5 times the characteristic length of the key microstructural feature. However, once an edge length of $2\lambda_2$ is reached (Figure 3.11b) the values stabilise, if not converge. Below this edge length the perturbations are large. When analysing rapidly changing structures, an RVE closer to the lower limit of two times the characteristic length might be a reasonable compromise.

The results of the analysis of the final structure are compared with prior experimental data and computational measurements in Table 3.1. The results of the present work agree well with the experimental measurements performed by Poirier [46] on columnar/dendritic structures, both parallel and normal to the primary arms of the dendrites. The predictions are also in agreement with the analytic Blake-Kozeny expression [46]. In this expression, the specific surface area S_V is defined as the solid/liquid interfacial area per unit volume of solid and is calculated from the tomograms using the marching-cube method. In the direction perpendicular to the primary trunks, the average of K_{xx} and K_{yy} was used, termed K_n. Two further studies are listed in Table 3.1, both of which are on equiaxed structures, but are listed for comparison. In the first study by Bernard *et al.* [34], the permeability of equiaxed Al-13.1 wt.% Cu structures was calculated using geometries obtained via synchrotron tomography and the same model as employed in this study, thus allowing the dimensionless permeability ($K.S_{\mathtt{V}}^2$) to be determined as a function of the size of the volume. The second, by Nielsen *et al.* [37], experimentally measured the $K.S_{\mathtt{V}}^2$ as a function of $f_{\mathtt{S}}$ for equiaxed Al-13.1 wt.%Cu structures by analysing the flow through a permeameter.

3.3.2 Flow stress

Finite element simulations were performed on the dendrite branches to determine the effective localised flow stress as a function of fraction solid. To compare with possible approximate solutions, a similar analysis was also performed on cylinders of: (a) equal fraction solid; (b) inscribed; and (c) circumscribed (Figure 3.7).

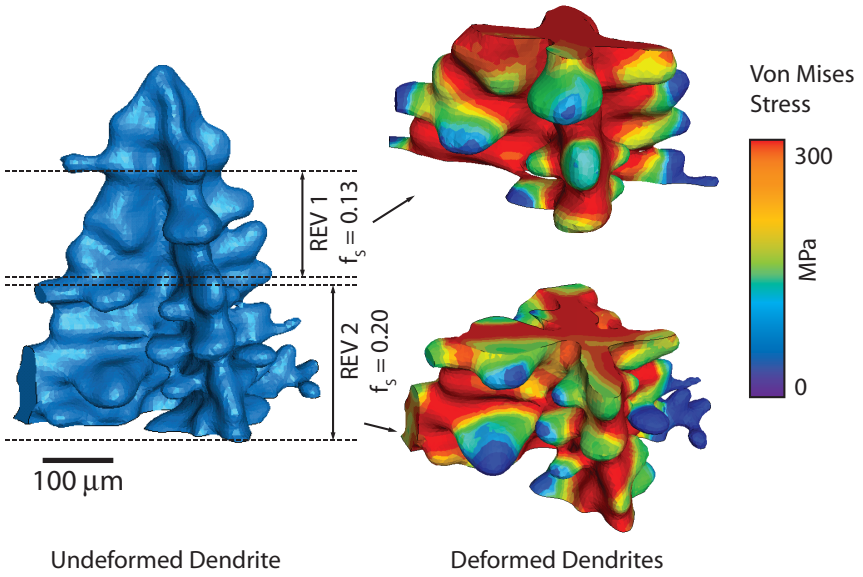


Figure 3.12: Simulation results for deformation of dendrite near the tip.

The stress generated in the RVEs is concentrated around the main stem of the primary and decreases towards the tips of the secondary arms (Figure 3.12). The load versus displacement curves for one of the RVEs is shown in Figure 3.13, together with possible approximate solution. Stress versus strain is not plotted since the cross-sectional area varies along the dendrite. The inscribed and the circumscribed cylinders define the boundary of the problem and as expected, the results for the load response of the dendrite and the cylinder with same fraction solid lie in this zone.

The load responses of the dendrites are also compared to the load response of a fully solid material multiplied by the respective volume fraction solid (Figure 3.13), an assumption used in many macro-model simulations. The results are off by 80-100%. These preliminary results clearly demonstrate the need for constitutive models to be developed by simulating the actual structure. For the cylinder with equivalent volume fraction of solid, the load response is offset to that of the dendrite by approximately 150%. The large difference in the values

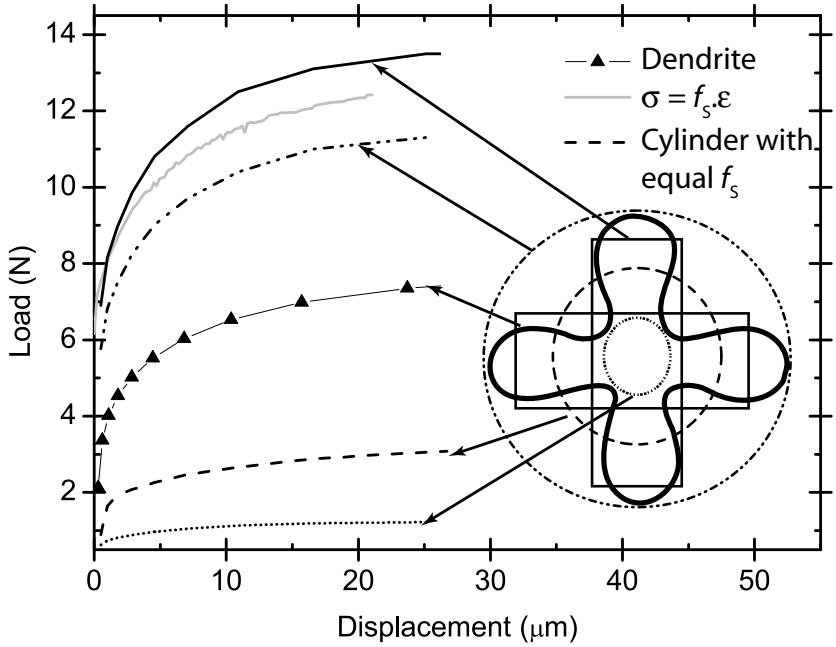


Figure 3.13: Load-displacement curve comparison for a dendritic geometry with other simple approximations as derived using FEM simulations.

dispenses with the assumption that the volume fraction of solid value being the determining factor in the case of deformation.

3.4 Summary

In this chapter, the columnar dendritic structure of quenched Al-12 wt.%Cu samples was quantified using x-ray microtomography and then used as the geometry input to demonstrate the feasibility of numerically determining the permeability using a control volume code and second, the flow stress behaviour using a finite element code. The conclusions from this chapter were:

1. The permeability tensor can be calculated using this technique and shows excellent correlation to experimental values.

2. To calculate representative flow behaviour, the RVE needs to have an edge length of at least two times the characteristic length scale (λ_2 in this case), but preferably 4 to 6 times.

3. The flow stress of real dendrite structure can be calculated via this technique. The results indicate that the existing approximations used to characterise the flow stress in the semi-solid as a function of the monolithic properties deviates from the actual behaviour by over 100%.

The last conclusion above highlighted the need to develop constitutive behaviour of semi-solid deformation using a full parametric study. This problem has been tackled in chapter 4.

Chapter 4

Derivation of a constitutive equation for the compressive behaviour of Al-Cu alloys

The semi-solid deformation behaviour of Al-alloys in processes such as TRC is often dealt in the industry [71] with a constitutive law meant for temperatures below solidus (equation 2.13). However, the temperatures at which the alloys are deformed are generally above the solidus temperature. Therefore, to improve the understanding of defect formation during thermo-mechanical conditions present during TRC, a better formulation of the semi-solid deformation is required. In chapter 3, the viability of performing virtual compression experiments on XMT generated columnar structures was assessed. Based on the results from that chapter, a comprehensive study has been performed in this chapter.

Neither analogous models nor experimental measurements have been successful in generating a constitutive model for flow stress behaviour of semi-solid with columnar morphology for a wide range of fraction solid due to complex geometry. In order to improve the methods further, a greater understanding of the deformation of real 3D microstructures is required. The 3D structures can be directly

A version of this chapter has been submitted for publication. Fuloria, D. and Lee, P. D.

exported as finite element (FE) meshes. The 3D geometries could also be generated using modelling techniques such as phase-field or front tracking which could be computationally intensive. This study will demonstrate how XMT and direct finite element modelling (DFEM) can be combined to predict the deformation behaviour of semi-solid Al-Cu alloys as a function of fraction solid by simulating the complex geometry evolving during solidification as demonstrated in chapter 3. Utilising this technique, a novel constitutive equation for the behaviour of semi-solid columnar dendritic structures in Al-Cu alloys is presented in this chapter as a function of temperature, strain, strain-rate and fraction solid.

4.1 Experimental methods

4.1.1 Sample Preparation

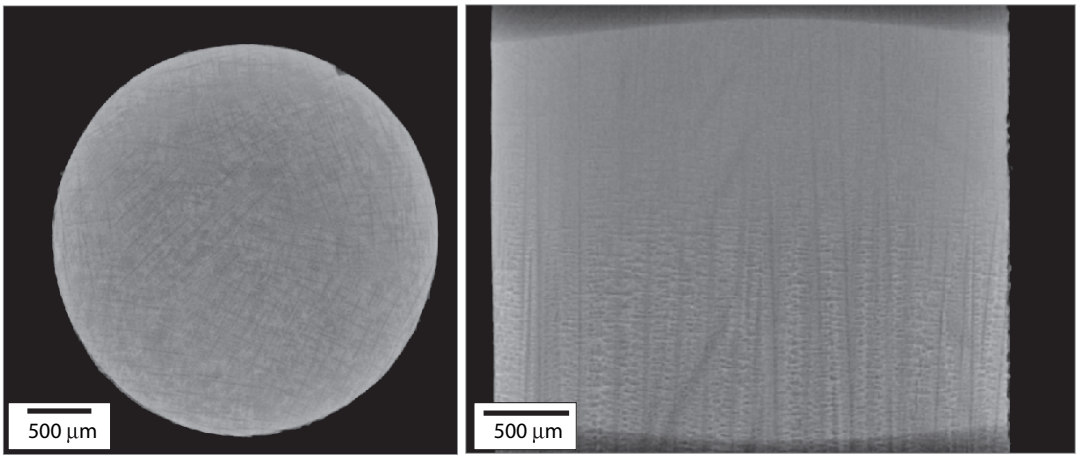
Al-12 wt.%Cu samples were directionally solidified and quenched in a liquid metal bath [124]. The resulting order of magnitude change in cooling rate alters the microstructure and composition sufficiently to resolve the columnar dendrite structure near the tips [125]. Metallographic analysis of the dendrites in directionally solidified sample using back scattered SEM images revealed that the concentration of Cu in the dendrites vary between 1 wt.% - 3 wt.%. This was quite different from the initial composition of the alloy due to solute rejection during solidification,requiring measurement of the mechanical properties of Al 1 wt.% and 3 wt.% Cu to be performed as detailed in section 4.1.4.

4.1.2 XMT and image analysis

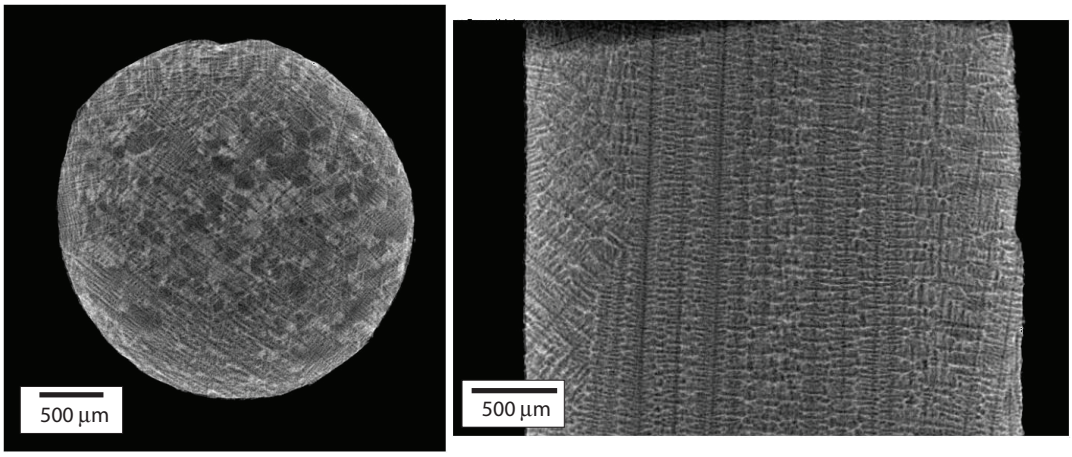
XMT was used to characterise the dendritic microstructures in 3D. Al-12 wt.%Cu was selected on the basis of considerable difference between x-ray attenuation coefficients for Al and Cu [8]. A laboratory x-ray source[1] with a spot size of approximately 2 μm was used with an accelerating voltage of 80 kV and a current of 80 μA. Polychromatic tungsten K_α radiation was used and transmitted radiation was recorded on a two-dimensional semiconductor type direct digital detector. After reconstruction, a resolution of 7 μm per voxel was achieved.

During the directional solidification of this alloy, the aluminium rich phase solidifies first in a dendritic manner, enriching the interdendritic liquid with copper, which solidifies when it reaches the eutectic composition of 33% Cu. In the XMT reconstruction of the quenched structure, the Al-rich dendrites appear as the bright phase and the interdendritic eutectic appears as the dark phase (attenuation ratio (Cu/Al) $\approx$ 8, see Figure 2.20). The difference in greyscale values is used to separate the phases (Figure 4.1 and 4.2).

[1] Phoenix—x-ray Systems and Services GmbH, Wunstorf, Germany



(a)



(b)

Figure 4.1: Slices of directionally solidified columnar dendritic structure of Al-12 wt.%Cu from (a) close to the tips; (b) deeper in the mush. Both figures show one axial and one sagittal slice as obtained from XMT scans.

4.1.3 Meshing of the 3D dendritic structure

One of the most critical steps to perform FE simulations on 3D microstructures is the mesh generation. The process of converting a 3D volume to a finite element mesh is not trivial, and many different approaches are available. One of the approaches used is the voxel-element technique [126], whereby each voxel in

the 3D volume is converted into an 8-node cubic element. However, voxel-based methods produce an inefficient representation of the microstructure containing a large number of elements and often requiring down-sampling of the mesh prior to modelling. Furthermore, this approach does not capture the particle morphology accurately if the voxel size is comparable to the feature size.

More sophisticated approaches to meshing involve the marching cubes algorithm [127] and advancing front methods. The marching cubes algorithm generates planes between interpolated values along the edges of each voxel, considering given weights of the corners and a user specified reference value (the grey level threshold). These 2D polygonal planes join together to form an enclosed 3D surface mesh. An advancing front method may be used to replace each polygon with a number of triangles, to allow subsequent solid meshing using tetrahedral elements as used in Amira[1]. This approach produces a more efficient mesh than the voxel-element method, allowing the modelling of large material volumes.

Whilst this technique works well for relatively simple geometries such as spherical pores, the present study has found it to be unreliable for complex geometries. In complex surfaces, the worst effect is seen at the edges, which can become staggered and act as regions of stress concentrations. Furthermore, the Amira meshing algorithm produces only linear (4-node) tetrahedral elements. Recently, Fureder *et al.* [128] have developed another technique which has been integrated to a commercial software ScanFE[2]. The technique involves proprietary algorithms for direct volumetric mesh generation from multi-part segmented data. The meshing is again grid-based but incorporates an adaptive meshing scheme resulting in a mixed 4-node tetrahedral / 8-node hexahedral mesh with variable mesh density. The automated mesh generation process ensures robust models in which the morphological accuracy is only contingent on the quality of the original image data. Though the automated mesh generation is very effective, it does generate a very fine mesh at simpler surfaces too. Presence of more nodes/elements than

[1]Mercury Computer Systems Inc., USA, ver. 4.1
[2]Simpleware Ltd., Exeter, UK

required puts a lot of pressure on the subsequent FE computational processes.

For the present study, meshes were generated through ScanFE. In terms of computing resources required to run deformation simulations, a coarser mesh with well defined features is desirable. Therefore, the coarser mesh generated by Amira is far less computationally extensive than the finer mesh generated through ScanFE. But the mesh generation in Amira requires the user to identify and amend the discrepancies in the structure, like intersections, orientations of triangular faces. For simple geometries, the process is smooth and there are few errors in the meshes which are easily amended. But as the geometry becomes more complex, the process of mesh generation does not remain trivial and requires trial and error method to amend the triangles. The time involved in the process could be huge. In comparison to Amira, ScanFE generates a finer mesh but takes a fraction of a time to generate meshes for highly complex dendritic structures used in the present study (Figure 4.2).

4.1.4 Gleeble: Thermo-mechanical testing

High temperature compression data available for Al 1 wt.% - 3 wt.% Cu is scarce. Therefore, alloys 1-3 wt.%Cu alloys were cast into wedges. The wedges were heat-treated to homogenise the chemical heterogeneity (see Figure 4.3). Cylindrical samples from the wedges (ϕ = 10 mm, length = 15 mm) were used for compression testing using Gleeble 3500[1]thermo-mechanical simulator at the University of British Columbia, Vancouver.

Tests were conducted at nine different temperatures in the range of 300 °C to 600 °C to study the temperature and strain rate dependent behaviour of the above alloys (see Table 4.1). For the first set of tests, strain rate was kept constant at $10^{-2}\,s^{-1}$ for a total strain of 0.4. For the second set of experiments, different strain rates ($10^{-4}\,s^{-1}$, $10^{-3}\,s^{-1}$, $10^{-1}\,s^{-1}$ and $1\,s^{-1}$) were used at three different temperatures (500 °C, 525 °C and 550 °C). The temperatures selected emulate

[1]Dynamic Systems Inc., Poestenkill, NY, USA

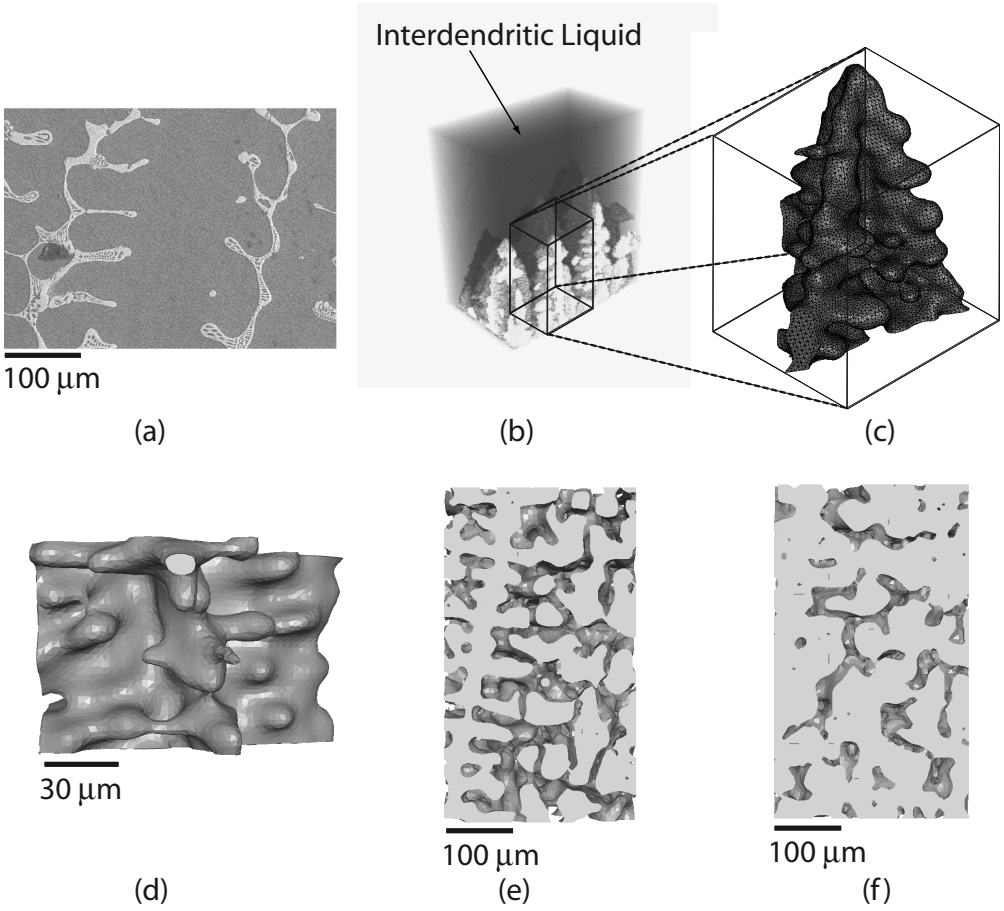


Figure 4.2: (a) SEM micrograph showing the columnar dendritic structure for Al-3 wt.%Cu were used to determine the composition of the dendrites. (b) XMT images are rendered in 3D to segment the phases (solid dendrites and interdendritic liquid) from each other. (c) Close-up of a meshed dendrite tip. Sample RVEs with different fraction solids are selected from similar 3D volumes. Figure (d) shows the structure of the dendrite near the tips where the fraction solid is below 0.2. Figure (e) and (f) show the RVEs with an average fraction solid of 0.60 and 0.77 respectively.

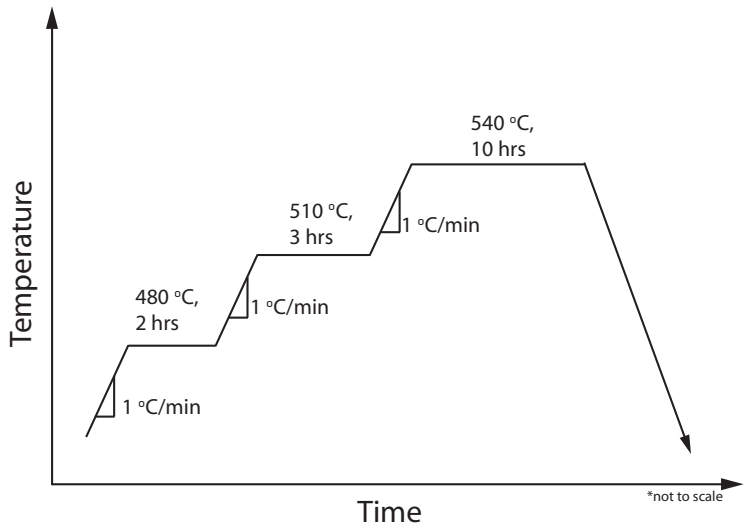


Figure 4.3: Homogenisation plan for Al-Cu wedges before extracting the samples for compression testing.

Table 4.1: Gleeble experimental conditions for compression tests on Al-1 wt.%Cu and Al-3 wt.%Cu.

T(°C)	300	400	450	475	500	525	550	575	600
			0.0001		0.0001		0.0001		
			0.001		0.001		0.001		
Strain-rate ($\dot{\epsilon}$)	0.01	0.01	0.01	0.01	0.01	0.01	0.01	0.01	0.01
			0.1		0.1		0.1		
			1		1		1		

the behaviour of the alloy at temperatures close to that in semi-solid processing of Al alloys. Repeats were also performed to assess the error at selected T/$\dot{\epsilon}$.

During the tests, the samples were heated resistively at a rate of 5 °C/s until reaching the test temperature and held for 5 mins before compression began. They were compressed to a macroscopic strain of 0.3 after which they were left

to undergo normal cooling. The temperature was measured using spot welded K-type thermocouples attached to the central region and the strain was measured using a clip-gauge.

4.2 Simulation methodology

The dendrites were divided along the solidification direction into representative volume elements (RVE) of varying fraction solids. As shown in Chapter 3 on flow properties of the semi-solid, a volume of size at least 3-5 times λ_2 is required for representative behaviour. In this study, the average RVE includes 7-8 secondary arms with the minimum of 3-4 secondaries near the tip of dendrites where f_s changes most rapidly [34, 68].

The same boundary conditions were applied to each RVE (Figure 3.8). Symmetry boundary conditions were imposed on the sides parallel to the columnar dendrites whilst deformation equivalent to 0.047 total planar strain was applied through the top nodes of each mesh. The nodes at the bottom face were fixed. The strain rate for all tests was kept constant at $0.1\,s^{-1}$. The bulk constitutive behaviour was estimated from the force-displacement values at reference nodes. A temperature boundary condition was also imposed to simulate the change in temperature along the length of the dendrites. A uniform temperature field was applied to each RVE depending on the average fraction solid. Corresponding temperatures were calculated from the Al-Cu phase diagram using the lever rule.

The mechanical properties of the semi-solid are comprised of the relative contribution of the different phases. In a typical Al-Cu alloy, these can include α-Al, liquid, θ-Al_2Cu and porosity. It has been shown that porosity less than 1% causes a drop of less than 10% on the flow stress [129]. In the present study, the effect of porosity was ignored. For the effect of the liquid phase, a sensitivity analysis was performed. For one of the simulations ($f_s = 0.6$), a hydrostatic pressure boundary condition was applied on the interface of the liquid and solid. There was a variation of less than 5% when the pressure was varied between 1 - 1000 MPa but including the surface boundary conditions made the simulations computationally more intensive. Therefore, in all subsequent simulations, the effect of hydrostatic pressure was ignored.

For the material properties of the solid dendrites, empirically derived properties of Al-1 wt.%Cu and Al-3 wt.%Cu were used in separate simulations. These temperature and strain rate dependent properties cover the range of simulation conditions. The elastic modulus of the solid phase was assumed to be 70 GPa while the poisson's ratio was set to 0.35 (which is that of a low temperature aluminium alloy).

4.3 Results and discussion

The flow stress data measured on the Gleeble will be presented together in with the regression analysis which were used to derive a constitutive equation for the σ-ϵ behaviour of polycrystalline Al-1 wt.%Cu and Al-3 wt.%Cu alloys as a function of temperature and strain rate. This equation, combined with DFEM simulations will be used to derive a fraction solid dependent flow stress equation for Al-Cu alloys.

4.3.1 Monolithic behaviour

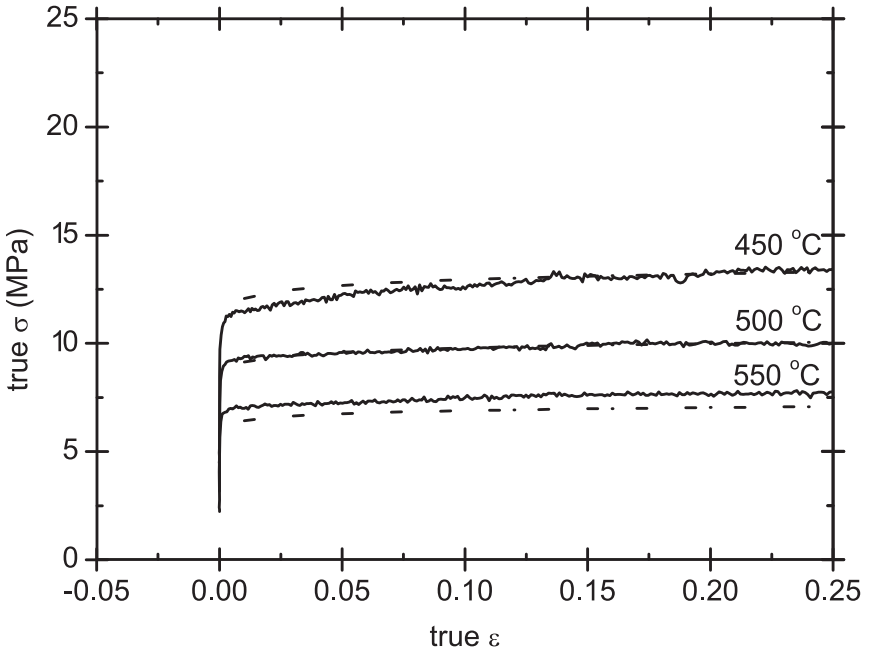
The temperature and strain rate dependent behaviour of Al-1 wt.%Cu and Al-3 wt.%Cu from the thermo-mechanical tests is summarised in Figure 4.4 and 4.5. Both alloys show a strong dependence on temperature and strain rate but a weak dependence on strain. In the temperature range $450\,^{\circ}\mathrm{C} < T < 550\,^{\circ}\mathrm{C}$, both samples show minimal elastic deformation followed by plastic flow with a minimal strain hardening. Above 550 °C, the stress actually decreases with increasing strain; this can be attributed to almost no strain hardening combined with sample barreling, giving an apparent softening behaviour. The results of the compression tests were used to derive an empirical flow stress relationship of the form [104, 130],

$$\sigma(\epsilon, \dot{\epsilon}, T) = K_0(\epsilon, \dot{\epsilon}, T).\epsilon^{m(T)}.\dot{\epsilon}^{n(T)} \tag{4.1}$$

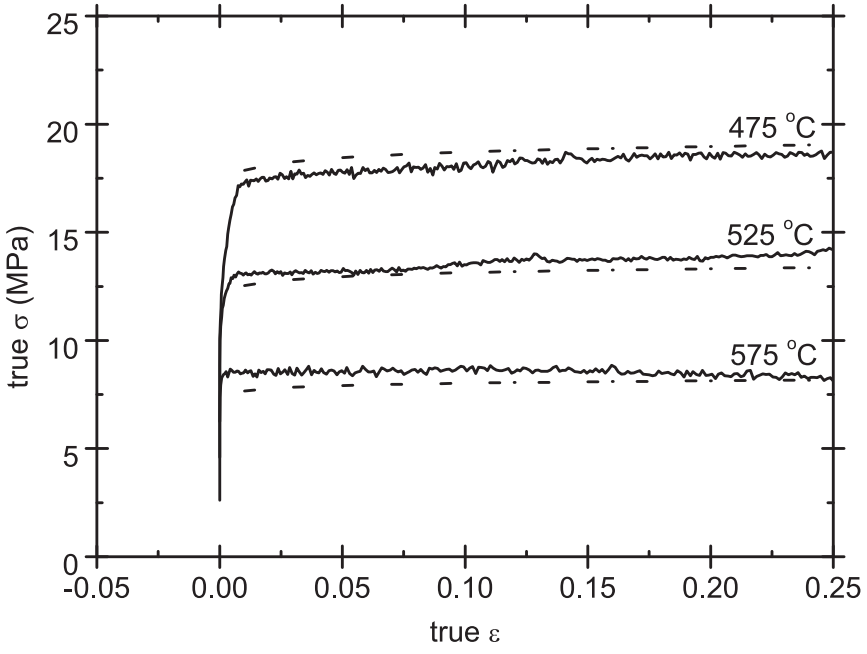
where, σ is the stress, ϵ is the plastic strain, $\dot{\epsilon}$ is the strain rate, K_0 is the

Table 4.2: Experimentally derived coefficients for Al-Cu alloys for $450\,^{\circ}\mathrm{C} < T < 600\,^{\circ}\mathrm{C}$.

	Al-1 wt.%Cu	Al-3 wt.%Cu
$K_0(MPa)$	$75.93 - 0.11T$	$140.56 - 0.2117T$
m	0.03	0.022
n	$0.14 + (T - 450) \times 0.0002$	$0.15 + (T - 450) \times 0.0002$

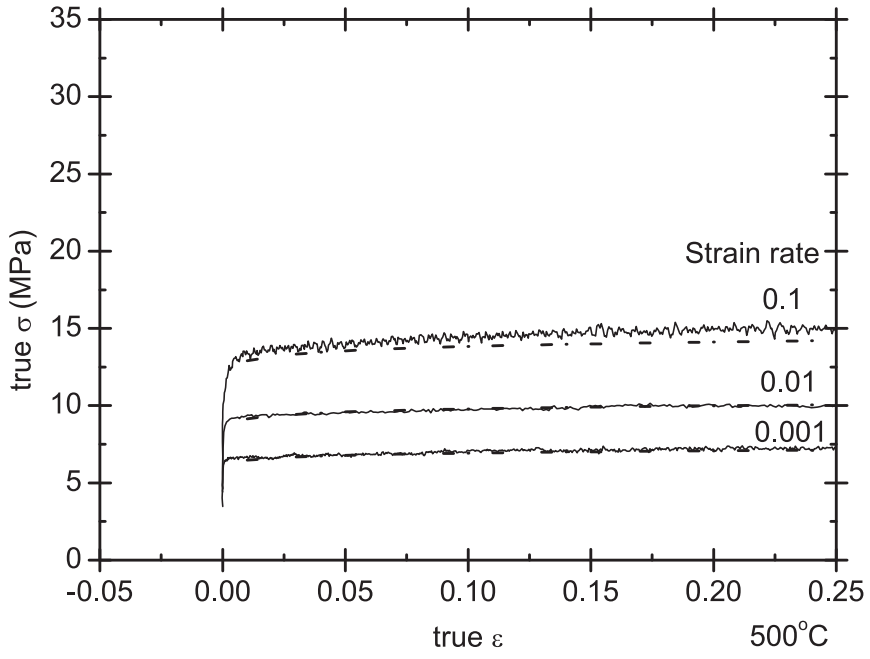


(a)

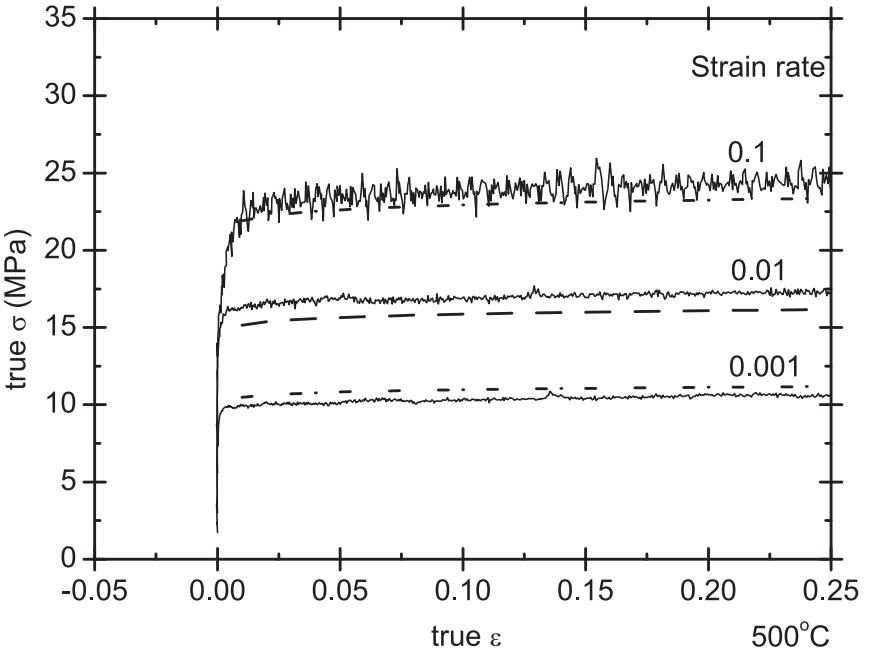


(b)

Figure 4.4: True stress - true strain relationship in (a) Al-1 wt.%Cu, (b) Al-3 wt.%Cu measured during compression experiments at $\dot{\epsilon} = 0.01$. The empirical model based results are shown as dashed lines.



(a)



(b)

Figure 4.5: Strain rate dependent properties at T = 500 °C for (a) Al-1 wt.%Cu, (b) Al-3 wt.%Cu. The dashed lines show the modelled results for the respective strain rates.

flow stress coefficient, m is the strain hardening factor and n is the strain rate sensitivity factor. These factors are all temperature dependent allowing Equation 4.1 to be used for the entire experimentally determined temperature range. Note, that the effect of temperature on strain hardening factor m was negligible and has been ignored. The experimental data was analysed at constant strain and constant strain rate to determine the values for the coefficients. These values are presented in Table 4.2 in a similar form to Phillion *et al.* [131]. The prediction of high temperature deformation with Equation 4.1 gives excellent agreement (<10% variation) with experimental results (Figure 4.6) illustrating that the coefficients are accurate in the temperature range of 450-600 °C. In this figure, the predicted stress at a strain of 0.1 is plotted against the measured stress for all the temperatures and strain rates tested in the Gleeble.

The coefficients in Equation 4.1 have been specifically derived for Al-Cu alloys in compression for a high temperature range (> 450 °C). These results are analogous to those obtained by Phillion *et al.* [131] for AA5182 alloy in tension and are compared in Table 4.3. The comparison shows a good correlation for T > 550 °C. Below that temperature, the flow stress in AA5182 increases more rapidly as compared to Al-3 wt.%Cu due to the solution hardening effects of Mg even at high temperatures.

Table 4.3: Comparison of flow stress in AA5182 [131] and Al-3 wt.%Cu (Equation 4.1) at $\dot{\epsilon} = 0.0015$.

T(°C)	σ(MPa)	
	AA5182[132]	Al-3 wt.%Cu
560	7.2	6.92
557	6.4	6.75
548	11.5	7.43
540	13.1	8.02

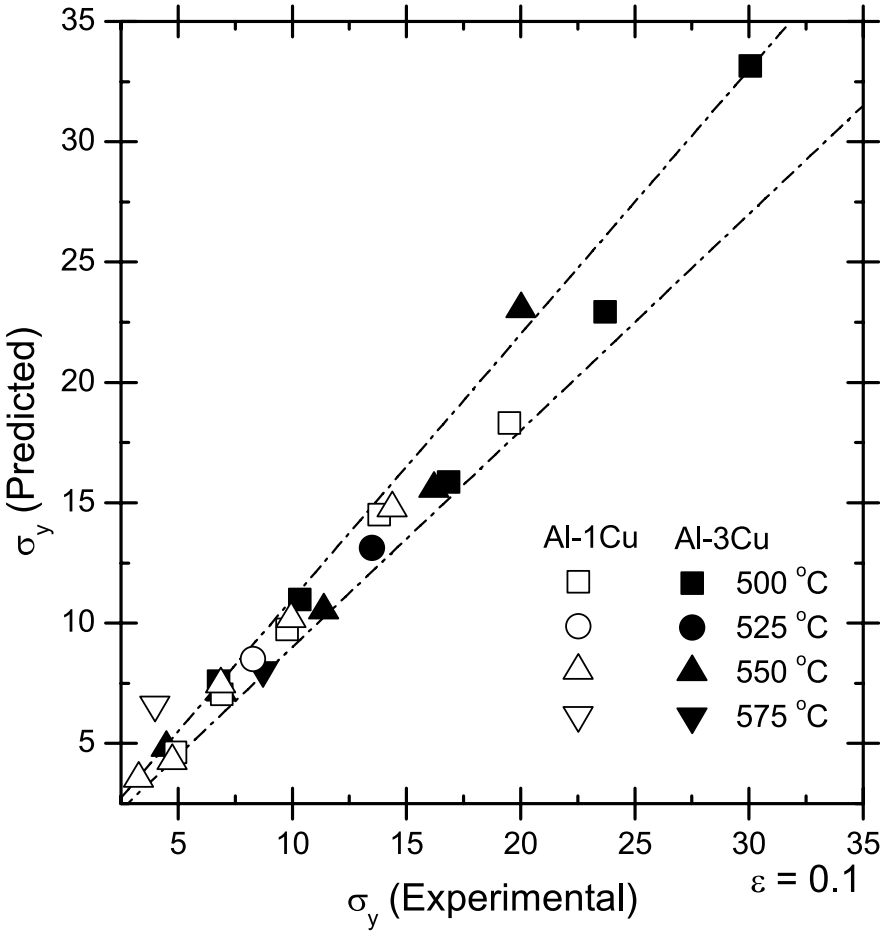


Figure 4.6: Comparison between the predicted *vs.* experiments stress values for Al-1 wt.%Cu and Al-3 wt.%Cu. Multiple points at a particular temperature represent stress values at different strain rates. The region bounded by the dashed lines represents the $\pm 10\%$ error.

4.3.2 FEM simulation results

In the first part of this study, an empirical constitutive Equation (4.1) was derived to predict the flow stress of monolithic Al-1 wt.%Cu and Al-3 wt.%Cu. The respective derived parameters for both alloys are listed in Table 4.2. The Cu compositional range was decided on the basis of energy dispesive x-ray spectroscopy (EDX) analysis on the columnar dendrites in a quenched Al-12 wt.%Cu sample (Figure 4.2). It is these dendrite pillars which provide resistance to com-

pression in semi-solid alloys assuming that the interdendritic liquid does not withstand any load. In the second part of the present study, FE simulations were performed on 3D dendrite structures derived from the XMT scans of directionally solidified Al-12 wt.%Cu sample. The use of real geometry of columnar dendrites gives an advantage over prior studies where approximated microstructures have been modelled [92, 107, 133, 134]. Examples of the typical RVEs used in the simulations are shown in Figure 4.2(d,e and f), normally encompassing $> 5\lambda_2$ (secondary dendrites) parallel to the loading direction and $> 4\lambda_1$ (primary dendrites) perpendicular to the loading direction. The range of strain simulated was limited to a maximum of 5% as beyond this strain, the impingement of the secondary dendrites to each other leads to numerical divergence. This limitation in the present model could be overcome if an explicit solver with contact is employed within the ABAQUS framework; However, the computational times would increase by greater than a factor of 10.

In the present simulations, the compressive behaviour of columnar dendrites was simulated in ABAQUS for 8 RVEs at fraction solid values of 0.13, 0.2, 0.57, 0.61, 0.67, 0.69. 0.77 and 1.0. The first two RVEs ($f_s = 0.13, 0.2$) were selected from close to the tip of dendrites (Figure 4.2(c)) while the last RVE ($f_s = 1$) was a monolithic volume. The other 5 RVEs ($f_s = 0.57$, 0.61, 0.67, 0.69 and 0.77) were selected from near the roots of the dendrite arms (Figure 4.2(e) and (f)).

During the FE simulations, the the top nodes were displaced to give a bulk strain of 0.047. The resulting reaction forces on the top nodes were used to calculate the bulk load. The load *vs.* displacement data was converted to true σ-ϵ data using the initial cross-sectional area of the respective RVE. This cross-sectional area includes the meshed dendrite as well as the unmeshed interdendritic liquid since the RVE represents a semi-solid. The length of the whole dendrite is used as the initial length to estimate the true strain. The comparison of true σ-ϵ curves in Al-1 wt.%Cu and Al-3 wt.%Cu from FE simulations is shown in Figure 4.7 for three different f_s values. The flow stress of the semi-solid is shown to be a strong function of f_s, reducing by over an order of magnitude as f_s goes from 1 to 0.13.

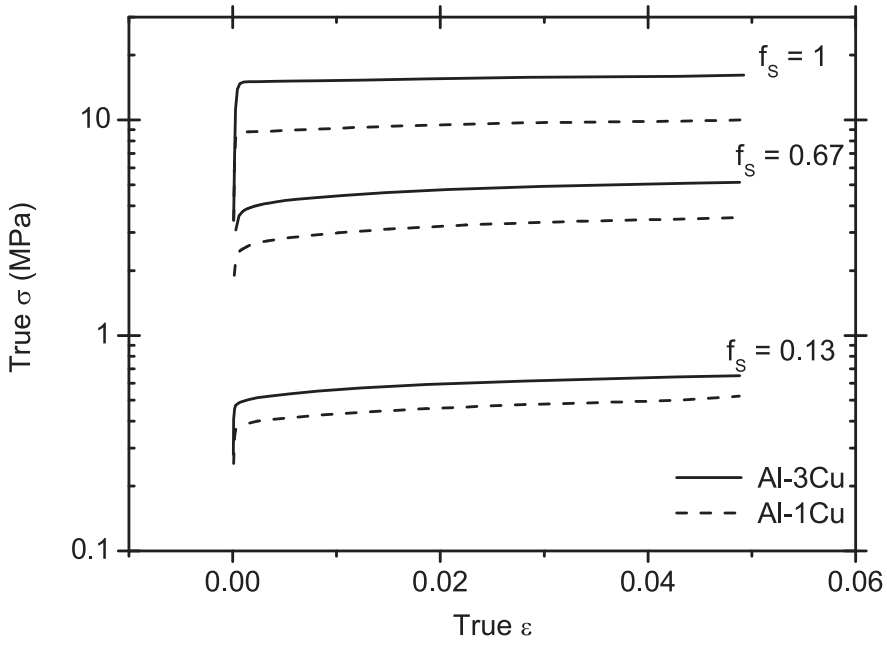


Figure 4.7: True stress - true strain curves for Al-1 wt.%Cu and Al-3 wt.%Cu at three different f_S values (0.13, 0.67 and 1.0) as determined from the FE simulations in ABAQUS.

The variation in flow stress with the variation in fraction solid of the columnar dendrite structure is critical in defining the constitutive behaviour of the semi-solid. To get the flow stress dependence as a function of fraction solid, flow stress for semi-solid Al-3 wt.%Cu was normalised relative to the flow stress for a fully solid volume at a strain of 0.01. The normalised flow stress was plotted as a function of the fraction solid as shown in Figure 4.8. The variation in the flow stress of the semi-solid in this plot can be attributed entirely on the geometric variations between the volumes. To verify that the difference is only geometric, another set of simulations is performed with the properties of Al-1 wt.%Cu and as can be seen in Figure 4.8, the normalised stress values match the ones for the previous alloy. The curves also show that the rate of change of strength increases approximately after 50% fraction solid which is similar to the bulk behaviour under deformation as presented in prior studies [65]. The results for the simulated alloys are also compared to experimental studies on other alloys.

As can be seen from Figure 4.8, the rate of drop in normalised flow stress is lower for the low carbon steel and Al-Si alloy the reason for which could be attributed to difference in structures.

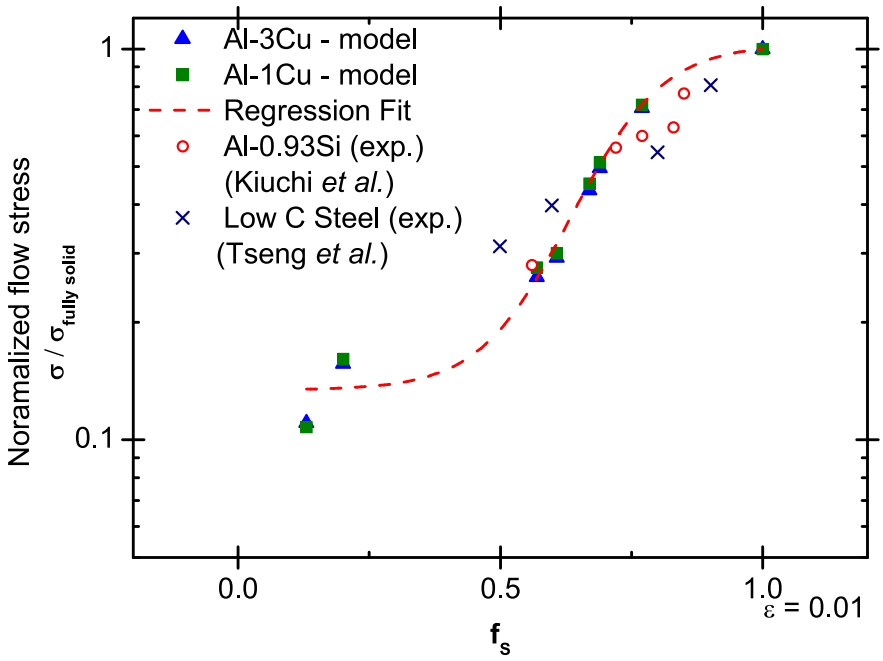


Figure 4.8: Normalised flow stress for dendrites of varying f_s from FE computations on Al-1 wt.%Cu and Al-3 wt.%Cu at 1% strain. The dashed line shows the regression fit which is then used as an f_s dependency term in Equation 4.2. These have been compared to the flow stress on other alloys (solid symbols) experimentally tested by prior authors [135, 136].

In conclusion, it was found that the flow stress of a coherent columnar structure in a semi-solid is a specific fraction of the flow stress of the alloy of dendritic composition. The points in the curve can be regression fitted to derive a fraction solid dependent function which defines the flow stress of the semi-solid.

$$\sigma = K_0.\epsilon^m.\dot{\epsilon}^n.F(f_s) \tag{4.2}$$

for $(0.1 < f_s < 0.9)$,

$$F(f_s) = A_1 + \frac{(A_2 - A_1)}{1 + 10^{(0.7172 - f_s).p}} \tag{4.3}$$

where, the values of constants A_1, A_2 and p are 0.134, 1.027 and 5.347 respectively. The relationship covers a wide fraction solid range and was selected since it was able to justify the nature of the curve in different fraction solid ranges; *e.g.* When the $f_s \approx 1$, the curve should be asymptotic. In columnar dendritic structures with uniaxial stresses, it could be assumed that at high fraction solid values (> 0.9), the stress-response of the structure does not change sharply. For f_s range between 0.2 to 0.5, where there was a clear lack of data, it was important to include the effect of dendritic geometry on the response of the structure. As shown in Figure 3.13, the stress response of a columnar dendritic geometry is off by 80-100% as compared to other simple geometric approximations (*e.g.* cylinders, crosses etc.) or a simple area fraction multiplicative factor. This is due to the effect of changing cross-section along the length of columnar dendrites. The stress is mainly generated in the primary trunk of a columnar structure but it is also distributed along the secondary arms (Figure 4.9). Therefore, it is important to use a curve fit which includes the actual geometric response of the structure. The resulting sigmoidal relationship is purely geometric and should be applicable to any alloy. For example, if the semi-solid properties of a different system with a similar structure are required, only the flow stress of the fully solid would need to be determined. The applicability of Equations 4.2 and 4.3 to other alloy systems is demonstrated by comparison to experimental data for semi-solid steels as measured by Tseng *et al.* [136] as shown in Figure 4.8. The data points are reasonably close to the curve given by equation 4.2, especially considering the solidification microstructure of the steel is not known. The data for Al-0.9 wt.%Si alloy [135] are also plotted on the same graph, again showing a good fit.

The new equation can be easily used in FEM simulations with improved capabilities for a wider range of f_s. Previously, the behaviour of semi-solid deformation was categorised into two distinct types based on the f_s - as a ductile solid beyond coherency ($\sim$50%) and as a non-newtonian fluid at low f_s [64]. This change

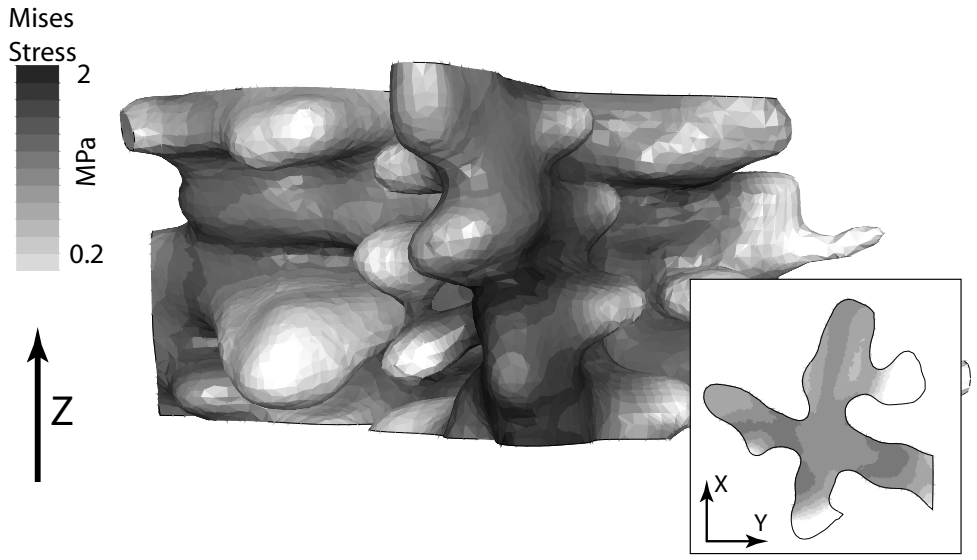


Figure 4.9: Stress distribution in a columnar dendrite ($f_s = 0.2$) for uniaxial deformation illustrates that the complex response of the dendrite shape cannot be modelled with simplified structures.

in the behaviour is difficult to simulate in FE models. It requires two different constitutive models for the simulations to be accurate over the whole range of f_s. This complication is overcome through Equation 4.2. The equation incorporates the changes in the deformation behaviour by only accounting for the change in geometry. Stress values predicted by Equation 4.2 were compared with peak stress values determined from from compression experiments on Al-4 wt.%Cu by

Table 4.4: Comparison of the present results on Al-3 wt.%Cu with Al-4 wt.%Cu by Tzimas *et al.* [95] and Ferrante *et al.* [70].

f_s	$\dot{\epsilon}$	σ_{exp}(MPa)[ref.]	σ_{pred}(MPa)
0.73	0.001	0.62 [70]	0.95
0.81	0.01	1.95 [70]	2.63
0.88	0.1	3.5 [95]	4.02

Tzimas *et al.* [95] and Ferrante *et al.* [70]. These predictions show a good correlation with at a fraction solid greater than 0.7 and strain rates less than 0.1 s^{-1}. However, the predictions using Equation 4.2 tend to overestimate the strength in general. This can be explained from the simulation methodology used in the present study. The compression applied is always uniaxial and along the direction of the primary. This is the direction of maximum resistance to compression as the structure is columnar. With increasing f_s, solidification structures become highly interconnected and the grains get interlocked (see Figure 4.2f). At these high f_s values, typically >0.9, the difference between the uniaxial compressive strength of a columnar and an equiaxed structure is considerably reduced. As can be seen from Table 4.4, the stress predictions are off by $\sim 50\%$ for f_s equal to 0.7. But when the f_s increases to 0.88, the predictions are off by $\sim 15\%$.

At lower fraction solid values, experiments are limited in studying the deformation behaviour. When the structure loses its coherency, the semi-solid behaves as a suspension and traditional compression tests are not useful. The results from the present study, therefore, provide new insight into the strength of the dendritic microstructures from near the roots ($f_s \sim 1$) to near the dendrite tips ($f_s \sim 0.1$). As can be seen from Figure 4.8, the rate of change of strength below 50% fraction solid is much lower. At $f_s = 0.13$, the strength of the dendrite is $\approx$10% of that of a fully solid material and cannot be ignored.

The methodology of using FE simulations on real structures has been demonstrated to work successfully. It has been used to derive a fraction solid dependency term for semi-solid compression which could be applied to similar alloys if the properties of the dendrites are known.

However, the present study has some important limitations which could be further improved. Firstly, in all simulations, the presence of interdendritic liquid has been ignored. In an open structure, where the liquid is free to move, the negligible effect of hydrostatic pressure is justifiable. However, in structures, where the liquid is trapped within a solid network, the resistance to deformation will be much higher. Secondly, one of the major assumptions in the present

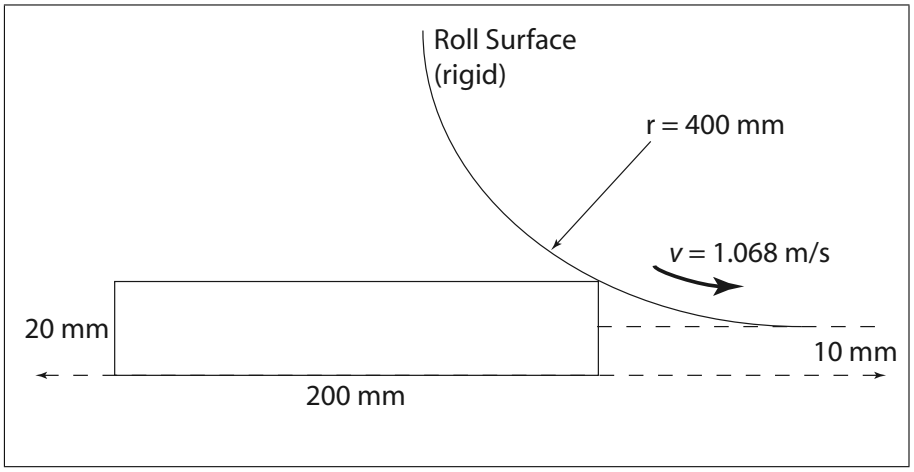


Figure 4.10: Schematic of the model with dimensions.

simulations is the application of material properties from compression tests on a polycrystalline material to a single crystal microstructure. This assumption has an important consequence as the compression tests (Figure 4.4) represent an isotropic yield stress which has been applied in a uniaxial compression state. In terms of the Mises criterion for yielding, the uniaxial stress, σ_0, is related to the multi-axial stress state in the compression sample by the following equation [72]:

$$\sigma_0 = \frac{1}{\sqrt{2}} \left[(\sigma_1 - \sigma_2)^2 + (\sigma_2 - \sigma_3)^2 + (\sigma_3 - \sigma_1)^2 \right] \tag{4.4}$$

Further improvements in the material property determination through accurate tests could be incorporated within the simulations. Also, the effect of multi-axial stress state in the RVEs need to be simulated. Thirdly, for the present study, an elasto-plastic model has been employed, but in high temperature deformation conditions, a visco-plastic creep based model would be more physically appropriate as a constitutive law as it includes the energy of activation required for dislocation climb [137, 138] (see equation 2.13). Lastly, in future studies, similar modelling procedure could be further improved by incorporating large simulation volumes, equiaxed structures and presence of liquid.

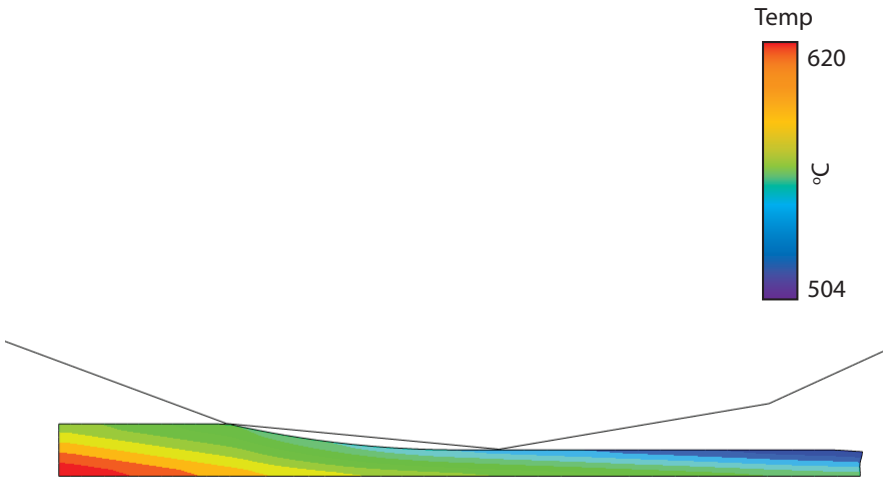
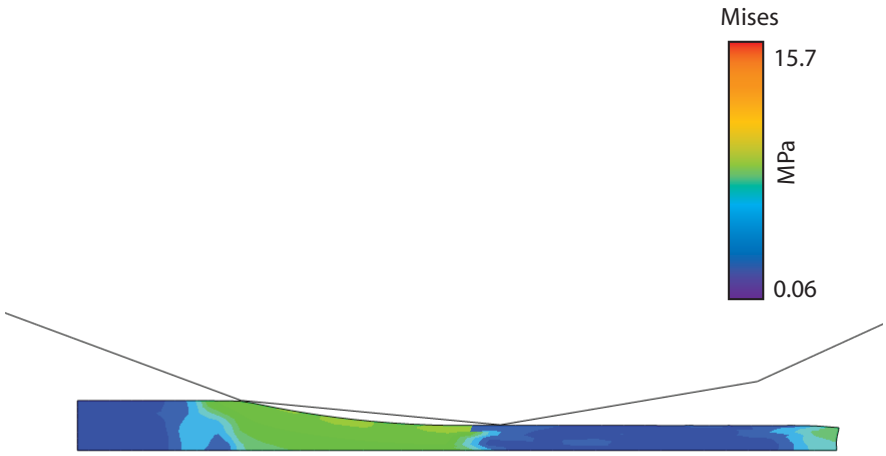


Figure 4.11: Assumed temperature profile in the 2D model of twin roll caster.

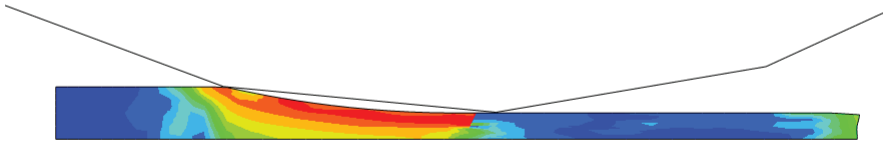
4.3.3 Macromodel of a twin roll caster

In this section, the constitutive equation for high temperature deformation of Al-Cu alloys has been applied to a 2D model (half symmetry) of a twin roll caster in ABAQUS. The dimensions of the rolls and the sheet deformation is illustrated in the schematic in Figure 4.10 and temperature profile is shown in Figure 4.11. The temperature along the sheet was a rough assumption of the profile expected within a roll caster [19]. At this stage, only stress analysis within the sheet was performed so as to illustrate the contrast between the simplified constitutive material behaviour (cylinder, f_s multiplication factor, etc) and the constitutive equation derived in the present study (Equation 4.2).

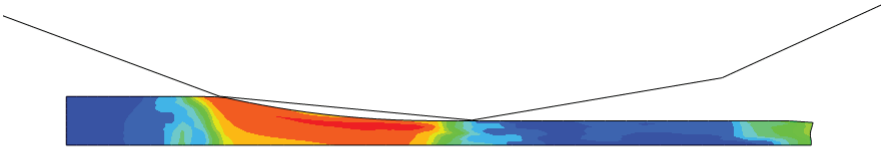
The stress response of a sheet with material properties defined as per Equation 4.2 (Figure 4.12b) was bounded by the responses for other approximations (Figure 4.12a and 4.12c). This was in accordance to the preliminary demonstration of the need to model the real geometry (Figure 3.13). More accurate stress distribution (Figure 4.12b) could then be used as an input in a separate simulation to model the interdendritic fluid flow at a location within the sheet. In



(a)



(b)



(c)

Figure 4.12: Stress distribution comparison in a twin roll cast alloy when three different cases for material property are used: (a) Inner bounding cylinder approximation (see Figure 3.13), (b) Equation 4.2 and (c) f_s multiplication factor case (see Figure 3.13).

future, a coupled fluid flow and deformation model could be useful in predicting the formation of certain defects as a function of temperature, displacement, roll speed, fraction solid etc.

In summary, a simplified constitutive material property equation was used in 2D FE models to demonstrate the applicability of the characterisation methodology presented in this work. Therefore, a computationally intensive analysis involving x-ray microtomography and meshing of microstructures was shown to be applicable to the macroscale as a single constitutive equation.

4.4 Summary

In this chapter, a full scale study was performed on XMT derived columnar structures of Al-12 wt.%Cu alloy to develop a constitutive equation for the semi-solid deformation. The specific conclusions from this chapter are:

1. The flow stress of Al-1 wt.%Cu and Al-3 wt.%Cu was measured using compression tests in a Gleeble 3500 for $450 \leq T \leq 600$ and $0.0001 \leq \dot{\epsilon} \leq 1$. Regression analysis was applied to this result to obtain the constitutive behaviour.

2. A procedure for determining the deformation behaviour of semi-solids was presented and validated for Al-Cu alloys solidifying with a columnar dendritic structure.

3. A fraction solid dependency term in a constitutive equation which provides a simple way to estimate the flow stress of semi-solid from fully solid properties. This term is only geometry dependent, which means that it can be applied to different alloys with similar solidification structures if the flow stress behaviour of the fully solid material is known. This relationship holds true for a wider range of fraction solid (0.1 - 0.9).

4. A preliminary 2D macromodel of a twin roll caster was presented to highlight the stress distribution within a deforming sheet. This macromodel could be further developed to include the heat transfer and fluid flow effects along with semi-solid deformation.

Chapter 5

In-situ synchrotron and x-ray observation semi-solid deformation of Al-Cu alloys

5.1 Introduction

The study of semi-solid deformation is important for a great number of material classes from the solidification of metallic alloys to the flow of granular materials in chemistry, geology etc. [57–62]. While low strains generally pose little risk to the semi-solid material, the combination of increasing strain above ∼2-3 percent and increasing fraction solid results in the formation of damage-induced voids [94, 139]. During solidification of metals, these voids may coalesce and form macroscopic cracks, otherwise known as hot tears, in the semi-solid. In aluminium alloys, hot tearing is particularly important since wide-spread commercial usage of many of the new, lightweight, and high strength alloy combinations are hindered by this defect. Hot tears develop in the mushy zone near the end of solidification [140], due to the combination of thermal strain, solidification shrinkage, and

A version of this chapter has been submitted for publication. Fuloria, D., Phillion, A. B., Hamilton, R. W., Rockett, P. and Lee, P. D.

a lack of interdendritic feeding.

Direct observation of semi-solid deformation is challenging due to the high temperatures and the similarity in opacity of both the solid and liquid phases. Almost all of the work in studying *in situ* semi-solid deformation has been to look at the formation of hot-tears through hot tensile tests. Though hot-tears can also be produced in a compressive state, the tensile tests provide an easier option. In spite of the challenges, *in situ* observation experiments has been previously reported by a number of researchers. Pellini [141] used x-ray radiography to observe hot tear formation in aluminum-copper alloys at low resolution. Fredriksson [142] performed hot tensile tests inside an SEM, showing that hot cracks occur if the alloy contains a eutectic liquid with good ability to wet the solid grain boundaries. Both Davidson *et al.* [143], and Mitchell *et al.* [144] recorded the formation of surface hot tears in an aluminum-copper alloy using a CCTV camera. Mitchell used the recording to examine strain accumulation, and determined that the strain is not homogeneous at the scale of the microstructure but is accompanied by a process of strain localisation. Farup *et al.* [145] combined an optical microscope and hot stage to study hot tear formation in succinonitrile-acetone. Hot tearing observations by Davidson, Mitchell, and Farup were captured real-time, while both Pellini, and Fredriksson captured images every 30 to 60 s. While the above research has been very insightful, key components have been missing. For example, in the studies by Davidson and Mitchell, it was not possible to observe clearly the dendrite / grain growth, and the interdendritic fluid. Furthermore, in the study by Fredriksson, the sample size was very small, and not representative of industrial hot tearing.

One alternative potential method for observing semi-solid deformation is a laboratory or synchrotron x-ray source, which can provide images with good phase contrast and high resolution. These x-ray sources have recently been successfully used for quantifying other solidification features such as dendrites, grains and pores [8, 10, 23, 114, 146–148]. In this chapter, a novel apparatus designed specifically to observe tensile and compressive deformation in the semi-solid materials is presented and applied to observe the first real-time, x-ray radiographic

observations of semi-solid deformation in Al alloys. The compression test data is presented first and it clearly shows the movement of interdendritic liquid with respect to the dendritic structure. These tests were followed by tensile tests that illustrated the stages of a void / hot-tear formation.

The motivation behind this chapter was to perform novel experiments to validate and further improve the constitutive model presented in chapter 4. However, a columnar dendritic growth in these experiments could not be achieved owing to a lack of thermal control.

5.2 Experimental setup

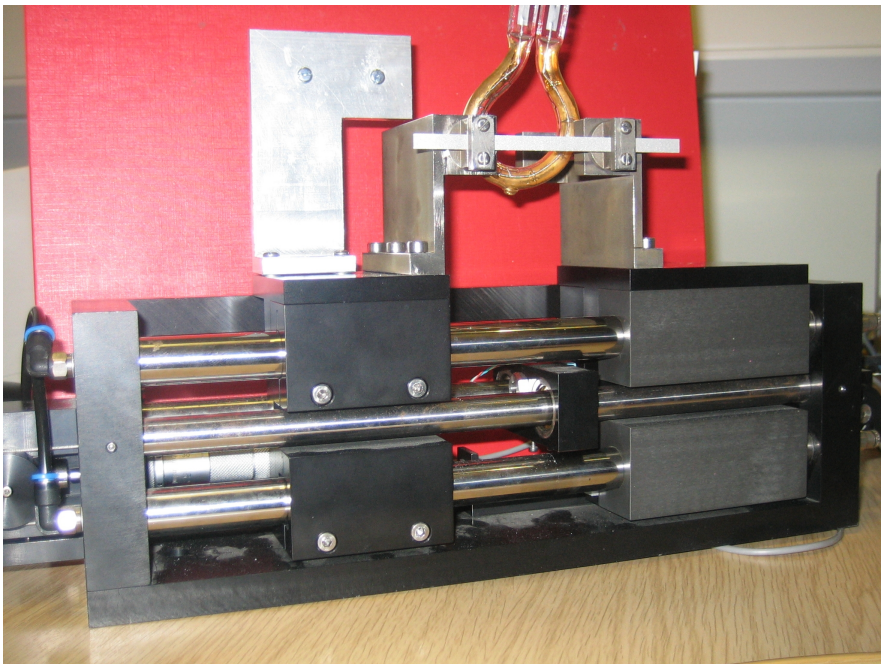
To perform *in situ* tension / compression experiments with semi-solid Al-alloys, an existing tensile / compression rig (described in detail in section 5.2.1) designed by Peter Rockett (University of Oxford) was modified. A new grip set was designed and infrared heating, capable of temperature in excess of 700 °C, was added. The motion control was reprogrammed so that it could be remotely controlled during synchrotron experiments.

5.2.1 Design of the tensile/compression rig

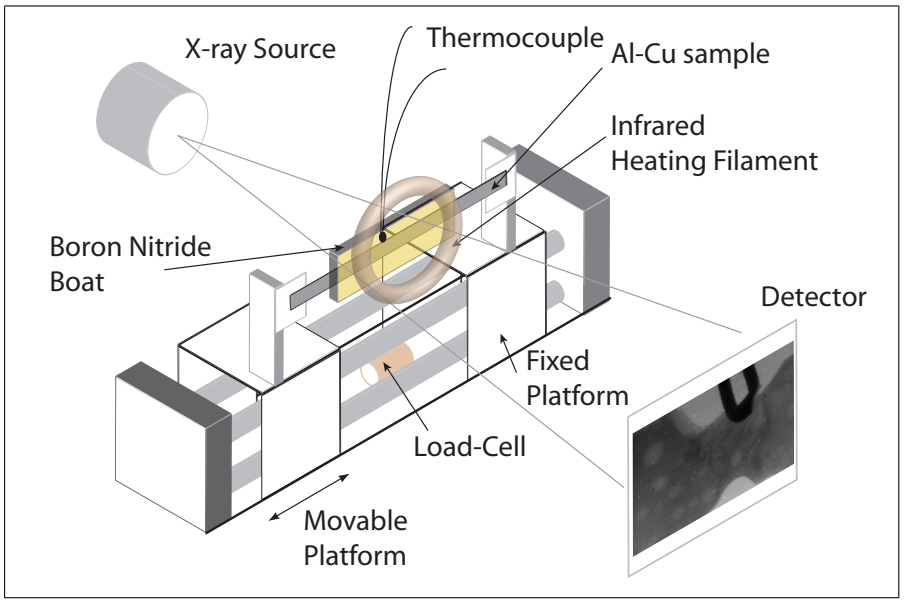
The semi-solid deformation apparatus consists of a tensile/compression platform with integrated heating (Figure 5.1), designed for use with both laboratory and synchrotron based x-ray sources. It has been designed to the following load-deformation performance criteria.

1. Axial loads up to 250 N with a load resolution of 0.1 N.
2. Deformation rates down to 2 µm/sec and up to 10^4 µm/sec with a resolution of at least 1 µm.
3. Computer controlled load-deformation path, with programmable options of load and deformation ramp rates. Exact load application or a step-sequence could also be independently programmed.

The tensile/compression grip platform is supported in a two shaft cylindrical aerostatic journal type bearing with negligible friction. Compressed air is supplied under 5 bar through the bearing shafts, rather than to the bearing casing, in order to avoid offset loads to the platform caused by the feed pipes. The bearing air film is replenished by radial feed holes in the shaft. This limits the travel of the mobile platform to a maximum of 30 mm, which is quite sufficient for the present set of experiments.



(a)



(b)

Figure 5.1: (a) Tensile/compression rig with compression sample; (b) Schematic of the equipment.

5.2.2 Motion control

The motion of the tensile/compression axis is provided by a crosshead mounted on a two shaft linear ball bearing system and is attached through a load-cell . The drive is coupled to a crosshead through a cable and pulley system, and driven by a *DC-servo* motor with a harmonic gearbox. For control, the motor possesses a rotary encoder with a resolution of 10^5 /rev and the mobile platform possesses a linear encoder with a resolution of $< 0.2\,\mu$m. The encoders provide the positional and velocity information which is used along with the load information from the load-cell as inputs in a computer program (MINT[1] programming language). These inputs are then used to control the motion of the moving platform through the motor.

5.2.3 Heating

The melting of the sample within an x-ray setup was performed using an infra-red emitting source (Omega emitter[2]) which is also shown in Figure 5.2. The selection of this heater was based on the design considerations which required focused heating of the sample without obstructing the x-rays. Selective gold coating of the heater helps in focusing the heat to center of the sample. The compact size of the heater (8 mm diameter quartz glass forming a loop of 39 mm diameter) is ideal to squeeze into the limited space available between the sample mounting blocks. It is powered with a 115 V supply which is manually controlled with a *variac* to provide desired temperature ramp rate. Manual control was preferred over automatic control of a controller as the on-off routine of a temperature feedback control was difficult to hold at a constant temperature. The variations during automatic control were $> 10\,^{\circ}$C. On the other hand, manual control of the voltage to the heater resulted in a smoother temperature profile.

[1]Baldor UK Ltd., Bristol, U.K.
[2]Heraeus Noblelight GmbH, Hanau, Germany

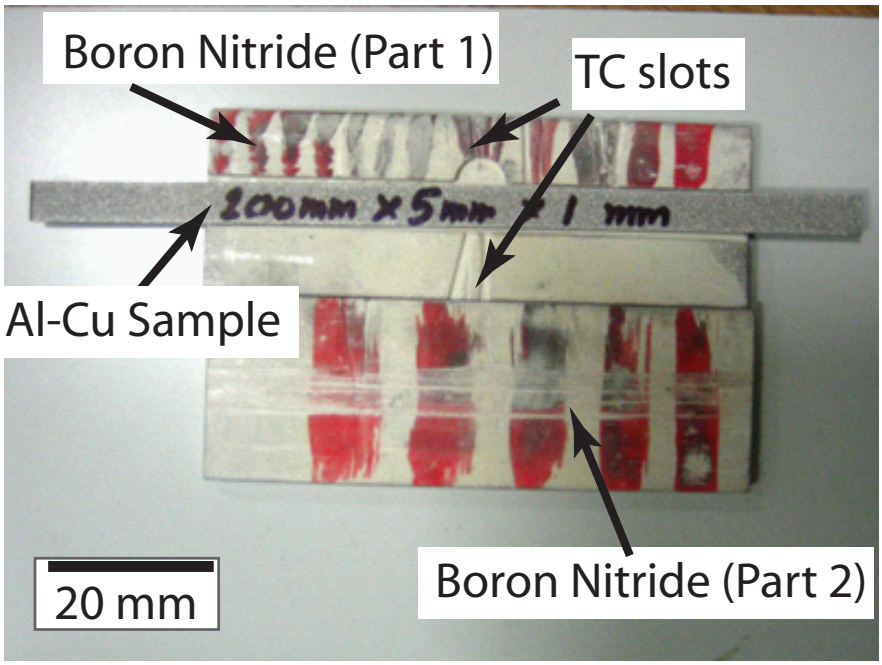


Figure 5.2: The omega emitter

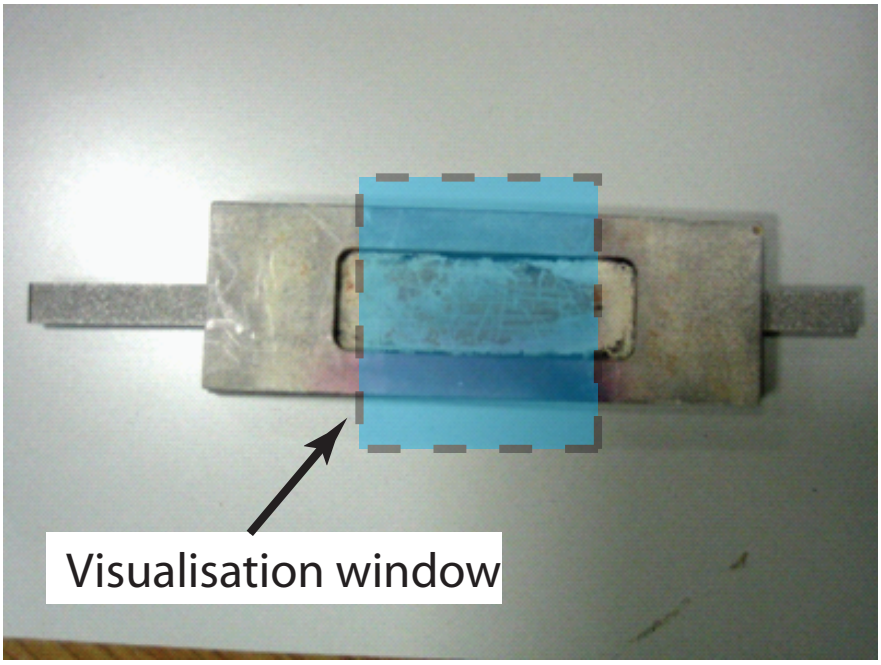
5.2.4 Experiments

The sample geometry for this apparatus consists of rectangular samples (100 mm × 5 mm × 1 mm with a central gauge (25 mm × 2.5 mm × 1 mm) region (see Figure 5.3). In this study, samples were machined from a pre-cast wedge of Al-12 wt%Cu.

Samples were heated until molten in the gauge region (∼675 °C) using an annular Omega infrared heater (Figure 5.2). This annular shape allows the x-rays to pass unencumbered from the x-ray source through the sample and into the detector. Heat was focused on to gauge length using selective gold coating, creating both a central hot-spot tapering with a parabolic temperature gradient to the chilled grips. The central gauge was surrounded by a boron nitride container which was open at both ends and free-floating, i.e. supported only by the solid part of the sample (Figure 5.3). Temperature was monitored using a K-type ther-



(a)



(b)

Figure 5.3: Actual sample within the boron nitride boat.

mocouple in contact with the top edge of the sample.

Using the deformation apparatus described above, real-time observations of semi-solid tensile deformation were obtained. The results from two tensile tests and a compression test are presented below. The samples were heated until fully molten (∼675 °C) and held for ∼500 s. First, a compression test was performed in constant cooling rate 2.2 °C/s and a crosshead displacement rate of 1.2 mm/sec. This test was performed at Imperial College London. These experiments posed problems with thermal control since the region of interest in the detector window was often not the hottest / weakest region.

In the first tensile experiment, samples were cooled at a rate of 0.3 °C/s which was maintained throughout the solidification. As the temperature passed through 625 °C, a crosshead displacement rate of 20 µm/sec was applied. The tests were performed for relatively low f_s (0.3 - 0.8) to increase the timescale of deformation and final fracture. Real-time observation of the hot-zone deformation were obtained using a laboratory x-ray source[1] at Imperial College London, and a 512 × 512 detector with an approximate resolution of ∼8.0 µm/pixel. The second tensile test was an isothermal test at 595 °C, and a crosshead displacement rate of 20 µm/s. For this specimen, images were obtained using a synchrotron-based x-ray source[2], and a 4008 × 2672 detector with resolution of ∼1.0 µm/pixel. For both tests, the image capture rate was 1.25 Hz.

[1] Phoenix—x-ray Systems and Services GmbH, Wunstorf, Germany
[2] SRS, Daresbury Synchrotron Radiation Source, Daresbury, UK

5.3 Results

5.3.1 Compression tests

The results of the first *in situ* and real-time x-ray radiographs of semi-solid compression in Al alloys are shown in Figure 5.4 for an Al-12 wt.%Cu alloy. The figure illustrates a sequence where semi-solid compression experiments were recorded in the laboratory x-ray source. The images show the growth of dendritic microstructures as the sample was cooled from an initial molten state. The relative distance between the dendrites decreased with deformation.

Force and temperature measured during the tests were plotted in Figure 5.5. This figure shows the increase in compressive load with decreasing temperature. As the temperature continues to decrease, the deformation got increasingly difficult. The disturbances in the load curve could be attributed to a combination of increase in the central cross sectional area and folding of the sample near the hot-spot.

The limited control of heating in the sample made it difficult to focus on to the deformation zone. The initial aim of recording the deformation of two converging columnar dendritic fronts could not be achieved. However, the results presented provide the basis on which the equipment could be further improved.

5.3.2 Tensile tests

The results of the first *in situ* and real-time x-ray radiographs of hot tearing in Al alloys are shown in Figs. 5.6-5.7 for an Al-12 wt.%Cu alloy. In Figure 5.6, the radiographs obtained during the continuous cooling / semi-solid deformation test are shown, along with a grey-scale histogram and a mechanistic diagram of hot tearing. In Figure 5.8, the recorded force and temperature as a function of time from the test shown in Figure 5.6 have been plotted with t=0 corresponding to the start of cross-head motion on the tensile/compressive platform. The locations of each of the images in Figure 5.6 are also indicated on this graph, by the letters (a)-(c). In Figure 5.7, the radiographs obtained during the isothermal semi-solid

Figure 5.4: X-ray radiography images of the compression experiment at (a) $t = 0\,\mathrm{s}$, (b) $t = 6\,\mathrm{s}$, (c) $t = 18\,\mathrm{s}$, (d) $t = 30\,\mathrm{s}$, (e) $t = 41\,\mathrm{s}$ and (f) $t = 60\,\mathrm{s}$. The dark band on top of the frames is the heater. Maximum compression occurs till frame (d) after which the structure becomes highly rigid.

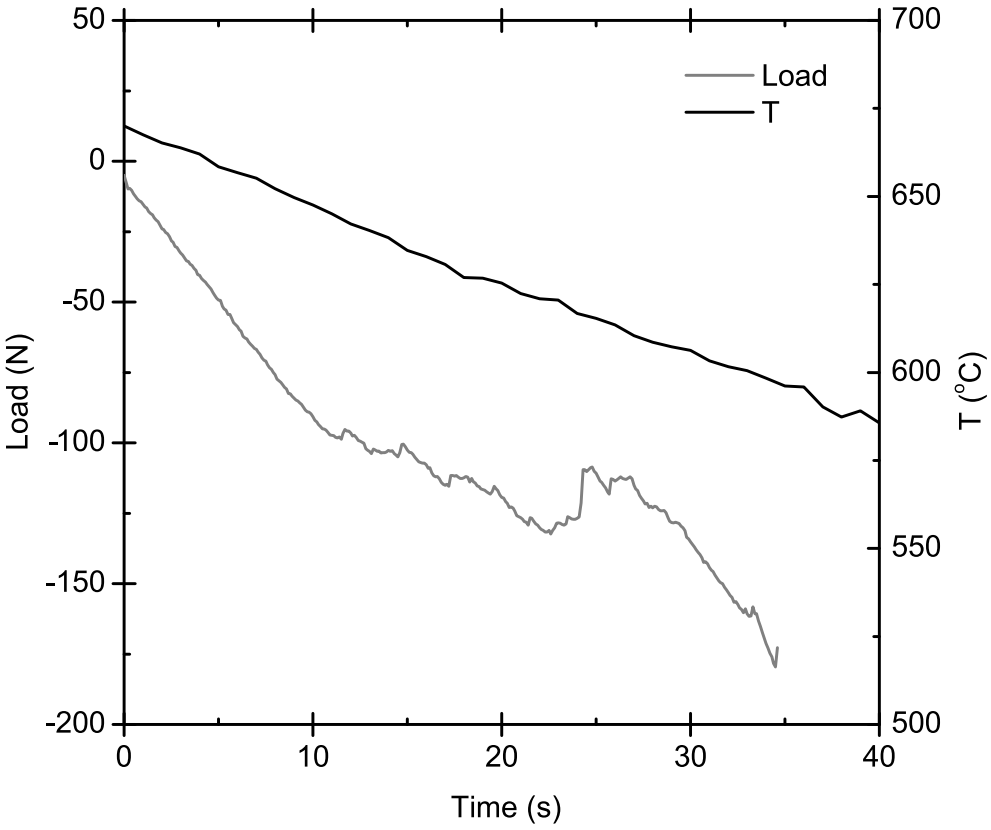


Figure 5.5: Load response and temperature variation as a function of time during the compression test.

deformation test are provided.

The radiographs shown in Figure 5.6 contain a portion of the deforming sample, as well as the thermocouple. At the start of the test, the sample was heated to 675 °C to ensure that it became entirely molten at the thermocouple location. Subsequently, the sample was cooled at a rate of 0.3 °C/s. Upon reaching 625 °C, tensile movement of the cross-head commenced. At this temperature, the sample was initially in a state of compressive stress resulting from the thermal expansion during heating (Figure 5.8, t =0). Once the compressive load was removed, plastic tensile deformation was initiated in the sample, and continued until final fracture. During deformation, the fraction solid, f_s, is estimated to have increased

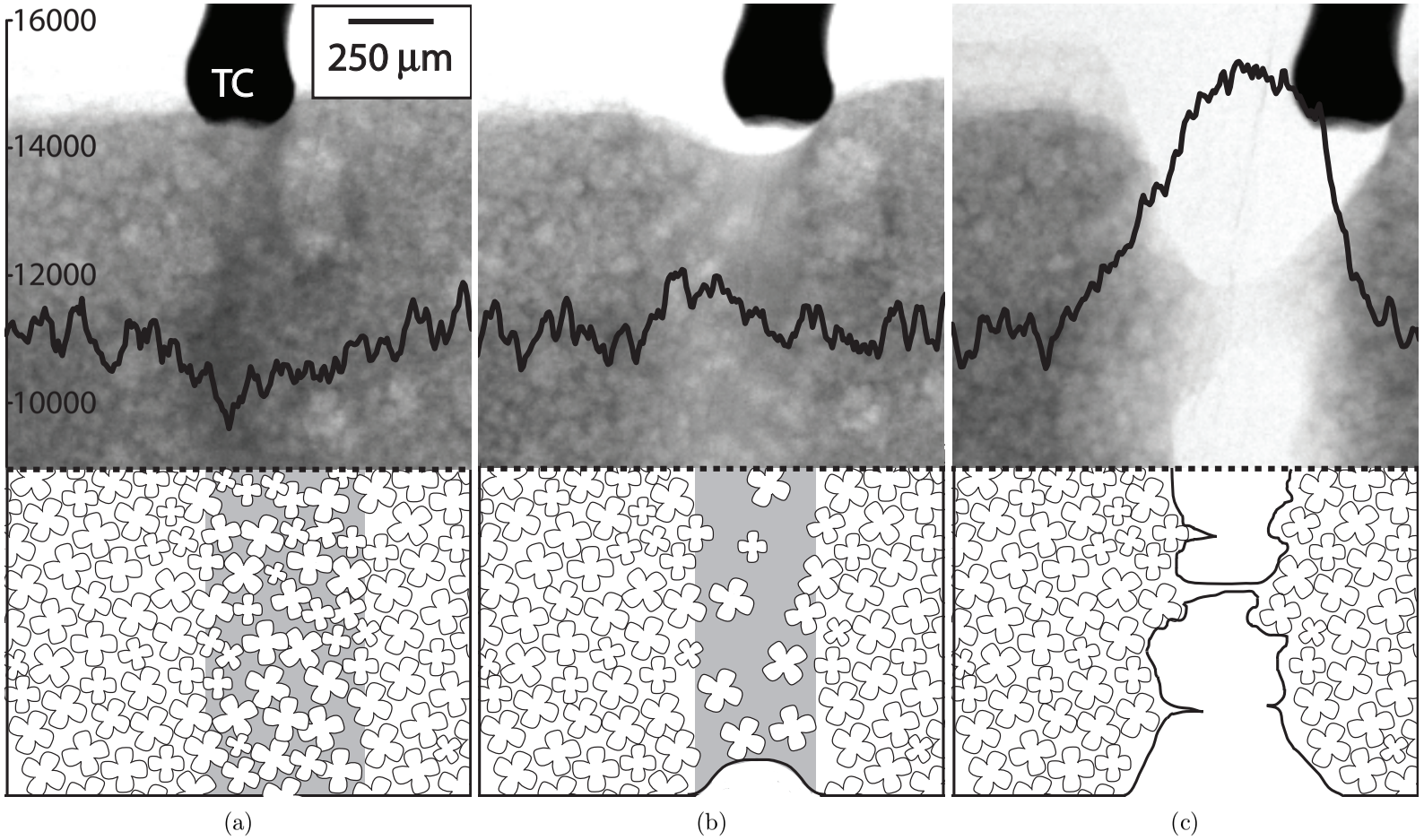


Figure 5.6: X-ray radiography images for the tensile experiment in the laboratory x-ray source at (a) $t = 67\,\mathrm{s}$, $T = 594\,^{\circ}\mathrm{C}$ and $f_\mathrm{s} = 0.56$; (b) $t = 95\,\mathrm{s}$, $T = 587\,^{\circ}\mathrm{C}$ and $f_\mathrm{s} = 0.66$; and (c) $t = 141\,\mathrm{s}$, $T = 544\,^{\circ}\mathrm{C}$ and $f_\mathrm{s} = 0.8$. The bottom half of each image is a schematic highlighting the key microstructural features. A histogram is also overlayed on each micrograph showing the variation of gray values along the specimen length.

from $f_s \sim 0.3$ to $f_s \sim 0.8$. This estimation is based on the thermocouple seen in the radiograph using a fraction solid - temperature curve derived from Thermocalc. However, since heat is extracted out along the length of the sample, the thermocouple reading represents an upper bound of the actual sample temperature and hence a lower bound on the fraction solid. Furthermore, the fraction solid on the crack surface will be considerably different than in the bulk, due to the liquid movement.

Visual evidence of a hot tear was first observed at 67 s, and is shown in Figure 5.6a. As can be seen in the figure, the hot tear initiated at the thermocouple, and there is clearly separation between the dark Cu-rich interdendritic liquid phase and the light Al-rich solid α-phase. After 95 s, Figure 5.6b, a neck has clearly formed in the sample. Deformation has localised to this necked region, where the fraction solid is lower due to the inflow of liquid. With increased tensile deformation, the neck continues to localise and eventually splits into multiple small bridges composed mostly of liquid between the two sides of the sample. Finally, only one semi-solid bridge remains, as shown in Figure 5.6c. After the sample fractured, the suction of the liquid phase from the hot tear surface back into the bulk occurred.

As shown in Figure 5.8, the sample can sustain considerable loads, even at low fraction solid. The continuous cooling test suggests that even at low fraction solid, semi-solids may have considerable resistance to deformation. However, it must be noted that industrial hot tears form within the casting, while the hot tear seen in this experiment formed on the surface of the sample. Hence, the role of liquid surface tension and surface wetting in the two cases may be quite different.

The radiographs shown in Figure 5.7 also contain a portion of the deforming sample, as well as the thermocouple. The same basic procedure as described above was used, although with slight modifications. Firstly, due to lack of a motion stage at the synchrotron x-ray source, the sample was notched to ensure that

Figure 5.7: X-ray radiography images of the tensile experiment in the synchrotron x-ray source at (a) $t = 70\,\mathrm{s}$, $T = 589\,^{\circ}\mathrm{C}$ and $f_\mathrm{s} = 0.6$; (b) $t = 90\,\mathrm{s}$, $T = 590\,^{\circ}\mathrm{C}$ and $f_\mathrm{s} = 0.62$; and (c) $t = 190\,\mathrm{s}$, $T = 601\,^{\circ}\mathrm{C}$ and $f_\mathrm{s} = 0.54$. A histogram is also overlaid on each micrograph, showing the variation of gray values along the specimen length.

the deformation localised within the detector's field of view. Secondly, the semi-solid tensile deformation was applied isothermally, at a temperature of 595±5 °C ($f_s \sim 0.55$).

As can be seen in Figure 5.7, this isothermal test was conducted at relatively low fraction solid. The initial semi-solid state of the material (Figure 5.7a), has considerable porosity, which is attributed to increased surface roughness of the boron nitride boat and provides more nucleation sites for the entrapped hydrogen. As with the previous test, the hot tear initiated at the thermocouple (Figure 5.7b). However, prior to final failure, the formation of a single very long necked region was observed (Figure 5.7c), and there was no splitting into multiple small bridges. This increased deformation as compared to the continuous cooling test, is clearly due to the lower fraction solid which allows for greater liquid flow to resist tensile deformation.

Based on these *in situ* observations of hot tearing, shown in Figure 5.6 and 5.7, a three-stage mechanism for hot tearing can be proposed:

Stage 1 - Hot tear Initiation - Once a crack initiates in the semi-solid, inter-dendritic liquid flows towards the location where the macroscopic crack will occur. These cracks may initiate due to the tensile stresses as a result of localised solidification shrinkage in combination with microporosity acting as a stress riser [131]. As can be seen from Figure 5.6a, the greyscale histogram contains a sharp minimum at the crack, providing evidence of Cu-rich interdendritic liquid at this location. As the liquid is displaced, due to tensile deformation, the likelihood of void formation in the region near the initiation site is greatly increased. The length of this stage is limited by the permeability of the solidifying structure, *i.e.* the evolution of fraction solid.

Stage 2 - Formation of Necked Region - The schematic shown in Figure 5.6b illustrates the start of this stage, which is characterised by the formation of a neck within the semi-solid. This necked region contains less solid due to the outward movement of grains. In the present tests, the liquid is on a free surface and is not

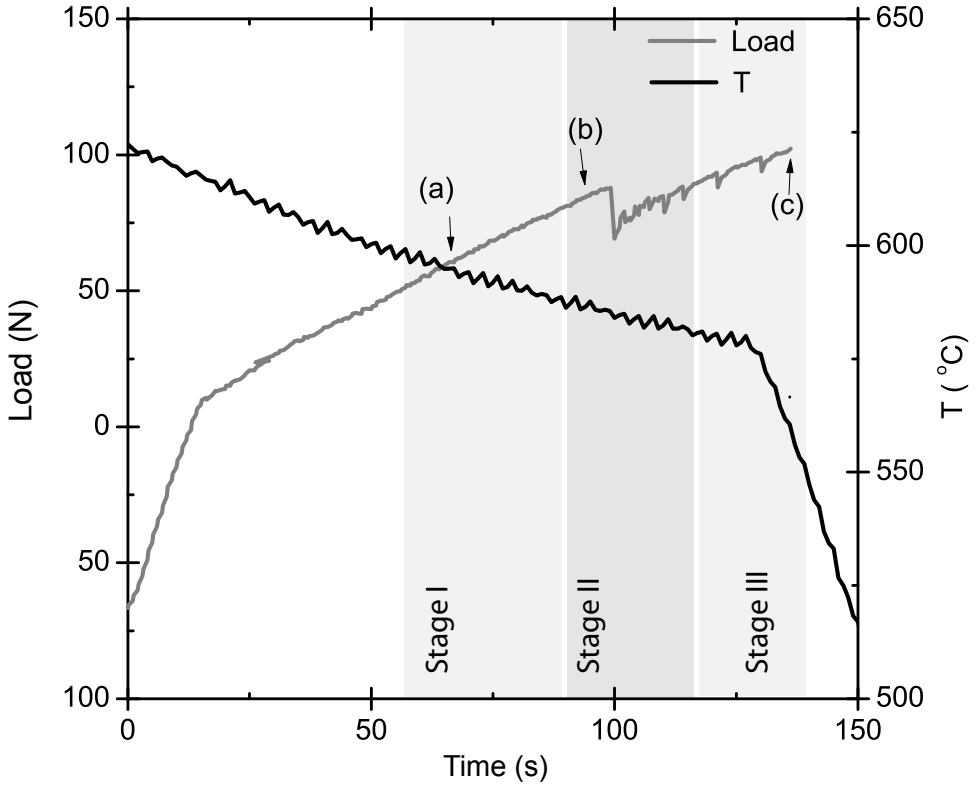


Figure 5.8: Load response and temperature variation as a function of time during the tensile test. The locations marked on the curve correspond to the respective images in Figure 5.6.

constrained. Hence, any increase in length can be compensated by extreme necking, *i.e.* thinning of the liquid at the neck and the formation of a larger gas-liquid interface without void formation. During actual castings, the liquid is constrained and the formation of a semi-solid neck must be accompanied by localised coalescence of as-cast porosity, as proposed by Phillion *et al.* [131] or by void formation.

Stage 3 - Final Fracture - This stage consists of the formation of multiple micro-necks, or grain bridges, followed by consecutive failure of each of these bridges. As shown in the schematic Figure 5.6c, the increase in fraction solid surrounding the crack restricts the flow of interdendritic liquid. This resulted in the formation of multiple voids and hence micro-necks. The coalescence of these

voids results in the final fracture. As soon as final fracture occurs, the pressure on the interdendritic liquid due to surface tension is released, and the liquid is sucked back into the intergranular region.

The mechanism outlined above is similar to the mechanism proposed by Phillion *et al.* [131], except that it is based on real-time measurements instead of post-deformation measurements. This mechanism can be applied equally to both the continuous cooling tests, such as Figure 5.6, and the isothermal tests, such as Figure 5.7. The difference between these two tests is the length of time spent in each hot tearing stage. In Figure 5.7, the low fraction solid and isothermal conditions allowed the semi-solid permeability to remain high. Hence, stage 1 was particularly exaggerated since there was considerable liquid feeding. Stage 2 was virtually non-existent, and stage 3 was short since only one micro-neck formed.

The newly-developed semi-solid deformation apparatus provides an excellent tool for conducting real-time *in situ* semi-solid deformation experiments. However, this apparatus has three important limitations with respect to hot tearing investigations. Firstly, the liquid is not fully constrained because the cracks appear on the surface of the sample. Secondly, hot tears usually form at very high fraction solid whereas the tests shown here were for moderate fraction solid. Thirdly, sample thickness is always small because of imaging / radiography requirements.

5.4 Summary

In this chapter, results of *in situ* synchrotron and x-ray tension / compression have been presented. The newly modified rig was successful in demonstrating the key strengths in semi-solid experimental capabilities by allowing control of solidification (temperature control) and deformation while recording images in real-time. The correlation of temperature / load information with local microstructural information is critical in bridging the gaps with numerical modelling. The most important conclusions from this chapter are listed below:

1. A new experimental apparatus has been designed which allows for real-time *in situ* observations of semi-solid deformation via x-ray radiography.

2. The experimental setup is ideal for quantification of semi-solid deformation in compression or tension.

3. A three-stage mechanism for hot tearing has been proposed-

   (a) Stage 1: Hot tear initiation and flow of liquid towards this location

   (b) Stage 2: Semi-solid necking in combination with limited permeability

   (c) Stage 3: Formation of micro-necks, and void coalescence

4. In semi-solids, the interdendritic liquid can sustain high tensile stress prior to failure.

Chapter 6

Conclusions and Future Work

6.1 Conclusions

The columnar dendritic structure of quenched Al-12 wt.%Cu samples was quantified using x-ray microtomography and then used as the geometry input to numerically determine first the permeability using a control volume code and second the flow stress behavior using a finite element code. The conclusions from this study were:

- The permeability tensor can be calculated using this technique and shows excellent correlation to experimental values.
- To calculate representative flow behavior, the RVE needs to have an edge length of at least two times the characteristic length scale (λ_2 in this case), but preferably 4 to 6 times.
- The flow stress of real dendrite structure can be calculated via this technique. The results indicate that the existing approximations used to characterise the flow stress in the semi-solid as a function of the monolithic properties deviate from the actual behavior by over 100%.
- An empirical relationship for the stress-strain behaviour for Al-1 wt.%Cu and Al-3 wt.%Cu was developed. The composition of the alloys was that of the columnar dendritic phase in Al-Cu alloys at semi-solid processing temperatures.

- A novel procedure for understanding the semi-solid deformation for Al-Cu alloys was presented in 3D using a combination of experimental methods (compression testing in the Gleeble), 3D microstructures (XMT) and FE simulations.

- A fraction solid dependency term in a constitutive equation which provides a simple way to estimate the flow stress of semi-solid from fully solid properties. This term is only geometry dependent, which means that it can be applied to different alloys with similar solidification structures if the flow stress behaviour of the fully solid material is known. This relationship holds true for a wider range of fraction solid (0.1 - 0.9).

- A new experimental apparatus has been designed which allows for real-time *in situ* observations of semi-solid compressive / tensile deformation via x-ray radiography.

- A three-stage mechanism for hot tearing has been proposed
  Stage 1: Hot tear initiation and flow of liquid towards this location
  Stage 2: Semi-solid necking in combination with limited permeability
  Stage 3: Formation of micro-necks, and void coalescence

- In semi-solids, the interdendritic liquid can sustain high tensile stress prior to failure.

6.2 Suggestion for further work

On the experimental side, an exisiting tension/compression rig was modified to test semi-solid alloys. Further experiments can be scheduled using this rig to observe the deformation of columnar structures. This could be achieved with improvements to the thermal control of the setup. A more complete study will yield a well-rounded result set which well help in understanding the semi-solid deformation mechanisms in Al-alloys as a function of varying alloy composition, temperature gradient or growth rates. Since, actual load-deformation data as

well as images of real time deformation are available, the process of semi-solid deformation can be better understood with emphasis on the inter-relation of the fluid flow (from the images) to the strength of the structure.

The DFEM technique used in the present work has provided a new and more accurate method of understanding the semi-solid behaviour in alloys. This technique allows for the actual geometry to be used in numerical simulations, but the quality of the meshes generated for FE models is contingent upon the image acquisition from a cast sample (or tomography capabilities). Further improvements in the FE models could be introduced with numerically modelled structures (through CA, phase-field, etc.) or with *in situ* experiments yielding 3D tomography results in a fast synchrotron source. These changes would also allow for the assessment of the deformation behaviour as a function of changing microstructure with time.

A constitutive semi-solid deformation model was developed in the present work. But this model is only based on FEM results on columnar structures. Equiaxed structures present difficulties during FEM as the grain contact problem does not converge to a solution within an implicit model. Firstly, equiaxed structures need to be modelled using the same technique to further improve the applicability of the equation. Secondly, higher strains need to be simulated to check the validity of the equation.

Using the methodologies presented in this dissertation, a complete macro-model of twin roll caster need to be developed. It should include heat flow considerations from the rolls to the solidifying metal and calculate stresses in the sheet at every computation step on the basis of micro-scale constitutive behaviour presented in chapter 4. An accurate stress distribution within the sheet would allow for the estimation of local interdendritic fluid flow. This information is critical in understanding the transport of solute and consequently, the formation of defects.

Appendix A

FEM simulation input parameters

1. A section of the ABAQUS input file used in simulations as presented in Chapter 3, highlighting the boundary conditions and step displacement applied. The initial section (nodes, elements, material properties, etc.) has not been shown here.

```
*Heading
simple compression test on dendrite tip (fs=0.2) in Al-12Cu.
Created 060927 by Devashish Fuloria.
**
** BOUNDARY CONDITIONS
** Bottom face
** Name:fixed in x, y, z Type: Displacement/Rotation
*Boundary
z_bot, 3, 3
z_bot, 2, 2
z_bot, 1, 1
**
*boundary
corner, pinned
** ----------------------------------------------------------
**
** STEP: Apply displacement in linear regime
**
*Step, name="Apply displacement 1"
displacement of 10 microns
```

```
*Static
0.1, 1., 1e-05, 1.
**
** BOUNDARY CONDITIONS
** Top Face
** Name: displacement in y Type: Displacement/Rotation
*Boundary
z_top, 3, 3, 10e-6
**
** OUTPUT REQUESTS
**
*Restart, write, frequency=1
**
** FIELD OUTPUT: F-Output-1
**
*Output, field
*Node Output
CF, RF, TF, U
*Node print, nset=z_top, totals=yes, frequency=1
U, RF
*Element Output
PE, PEEQ, PEMAG, S
*Contact Output
CDISP, CSTRESS
**
** HISTORY OUTPUT: H-Output-1
**
*Output, history, frequency=99999
*Node Output, nset=z_top, variable=PRESELECT
*Incrementation Output, variable=PRESELECT
*Contact Output, nset=z_top, variable=PRESELECT
*El Print, freq=999999
*Node Print, freq=999999
*End Step
**-----------------------------------------------------
```

2. A section of the ABAQUS input file used in 2D rolling example (Figure 4.11) simulations as presented in Chapter 4 (section 4.3.3), highlighting the boundary conditions and step displacement applied. The initial section (nodes, elements, material properties, etc.) has not been shown here.

```
** INTERACTION PROPERTIES
**
*Surface Interaction, name=FRICT-STEP-1
*Friction
 0.3,
**
** PREDEFINED FIELDS
**
** Name: Field-1   Type: Temperature
*Initial Conditions, type=TEMPERATURE
BAR, 625.
```

```
** Name: IC-1   Type: Velocity
*Initial Conditions, type=VELOCITY
BAR, 1, 1.0367
BAR, 2, 0.
** ----------------------------------------------------
**
** STEP: Step-1
**
*Step, name=Step-1
*Dynamic, Explicit
, 0.089286
*Bulk Viscosity
0.06, 1.2
**
** BOUNDARY CONDITIONS
**
** Name: Disp-BC-1 Type: Displacement/Rotation
*Boundary
BOTTOM, 2, 2
** Name: Disp-BC-2 Type: Displacement/Rotation
*Boundary
_M17, 1, 1
** Name: Disp-BC-3 Type: Displacement/Rotation
*Boundary
_M17, 2, 2
** Name: Vel-BC-1 Type: Velocity/Angular velocity
*Boundary, type=VELOCITY
_M16, 6, 6, 6.2832
**
** PREDEFINED FIELDS
**
** Name: Predefined Field-3   Type: Temperature
Using Analytical Field: TGRAD
*Temperature
**
** INTERACTIONS
**
** Interaction: FRICT-STEP-1-1-1-1-1-1
*Contact Pair, interaction=FRICT-STEP-1, mechanical
constraint=KINEMATIC, cpset=FRICT-STEP-1-1-1-1-1-1
SURF1, ROLLER-1.ROLLER-
1-ROLLER-1-ROLLER-1-ROLLER-1-ROLLER-1
-ROLLER
**
** OUTPUT REQUESTS
**
*Restart, write, number interval=10, time marks=NO
**
** FIELD OUTPUT: F-Output-1
**
*Output, field, number interval=1, time marks=YES
*Element Output, directions=YES
CTSHR, MISESMAX, PEEQ, PS, S, SVAVG, TEMP,
TRIAX, TSHR, VS
**
** FIELD OUTPUT: F-Output-2
**
*Node Output
U,
**
```

```
** FIELD OUTPUT: F-Output-3
**
*Element Output, elset=QA_TEST, directions=YES
CTSHR, MISESMAX, PEEQ, PS, S, SVAVG, TEMP,
TRIAX, TSHR, VS
**
** FIELD OUTPUT: F-Output-4
**
*Node Output, nset=QA_TEST
U,
**
** FIELD OUTPUT: F-Output-5
**
*Output, field
*Element Output, directions=YES
TEMP,
**
** HISTORY OUTPUT: H-Output-1
**
*Output, history, variable=PRESELECT, frequency=
9999
*End Step
**-------------------------------------------------
```

Appendix B

Compositional variation in dendritic microstructures

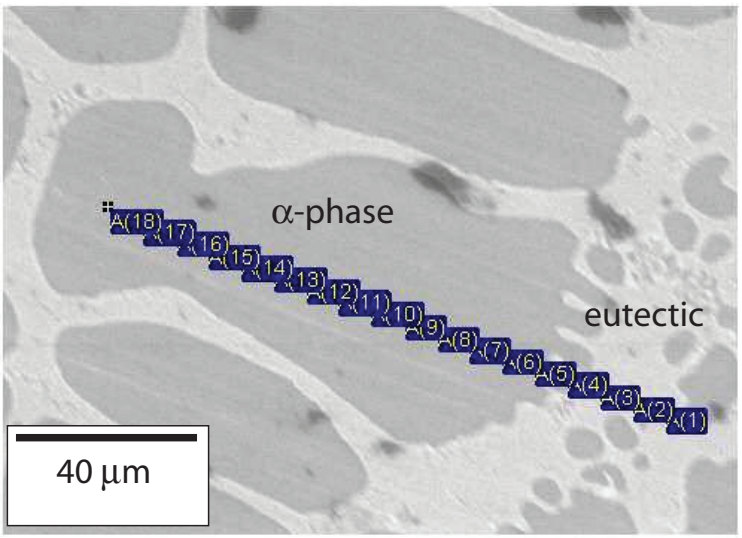


Figure B.1: SEM image of the columnar structure in directionally solidified Al-12 wt.%Cu alloy. EDX analysis points are marked in the image.

Table B.1: EDX analysis of an Al-12 wt.%Cu directionally solidified alloy in Figure B.1 (All elements normalised).

Spectrum	Al (wt. %)	Cu (wt. %)	Total (wt. %)
A(1)	64.49	35.51	100
A(2)	66.39	33.61	100
A(3)	64.91	35.09	100
A(4)	71.39	28.61	100
A(5)	95.62	4.38	100
A(6)	96.2	3.8	100
A(7)	96.46	3.54	100
A(8)	96.54	3.46	100
A(9)	96.58	3.42	100
A(10)	96.69	3.31	100
A(11)	96.75	3.25	100
A(12)	96.72	3.28	100
A(13)	96.57	3.43	100
A(14)	96.62	3.38	100
A(15)	96.72	3.28	100
A(16)	96.53	3.47	100
A(17)	96.63	3.37	100
A(18)	96.53	3.47	100
Mean	89.91	10.09	100
Std. deviation	12.78	12.78	
Max.	96.75	35.51	
Min.	64.49	3.25	

References

[1] J. R. Davis. *Aluminum and Aluminum Alloys*. ASM International, 1993. 21

[2] R. E. Sanders. Technology innovation in aluminium products. *JOM (USA)*, 53(2):21–25, 2001. 10, 21, 25, 26

[3] M. Yun, S. Lokyer, and J. D. Hunt. Twin roll casting of aluminium alloys. *Materials Science and Engineering A*, 280:116–123, 2000. 10, 22, 27, 28, 30

[4] C. Gras, M. Meredith, and J. D. Hunt. Microdefects formation during the twin-roll casting of al-mg-mn aluminium alloys. *Journal of Materials Processing Technology*, 167(1):62–72, 2005. 10, 22, 27, 28, 29, 31, 32

[5] C. Gras, M. Meredith, and J. D. Hunt. Microstructure and texture evolution after twin roll casting and subsequent cold rolling of al-mg-mn aluminium alloys. *Journal of Materials Processing Technology*, 169(2):156–163, 2005. 10, 22, 30, 31

[6] P. D. Lee. *The Formation of Hydrogen Porosity During the Solidification of Aluminium Alloys*. Ph.d., University of Oxford, 1994. 22, 61

[7] P. D. Lee and J. D. Hunt. Measuring the nucleation of hydrogen porosity during the solidification of aluminium-copper alloys. *Scripta Materialia*, 36(4):399–404, 1997.

[8] P. D. Lee and J. D. Hunt. Hydrogen porosity in directional solidified aluminium-copper alloys: in situ observation. *Acta Materialia*, 45(10):4155–4169, 1997. 61, 63, 66, 83, 109

[9] P. D. Lee and J. D. Hunt. Hydrogen porosity in directionally solidified aluminium-copper alloys: A mathematical model. *Acta Materialia*, 49:1383–1398, 2001. 22, 63

[10] D. Bernard, G. Damien, H. Jean-Marc, B. Sylvie, and E. Jean. First direct 3d visualisation of microstructural evolutions during sintering through x-ray computed microtomography. *Acta Materialia*, (53):121–128, 2005. 23, 50, 53, 58, 74, 109

[11] D. M. Lewis. The production of non-ferrous metal slab and bar by continuous-casting and rolling methods. *Metallurgical Reviews*, 6(22):143–192, 1961. 25

[12] E. F. Emley. Continuous casting of aluminium. *International Metallurgical Review*, 21:75–115, 1976. 25

[13] H. J. Lin. Modelling of flow and heat transfer in metal feeding system used in twin roll casting. *Modelling and Simulation in Materials Science and Engineering*, 12(2):255, 2004. 25, 32

[14] R. Cook, P. G. Grocock, P. M. Thomas, D. V. Edmonds, and J. D. Hunt. Development of the twin-roll casting process. *Materials Processing Technology*, 55:76–84, 1995. 25

[15] N. Sun, B. R. Patterson, J. P. Suni, E. A. Simielli, H. Weiland, and L. F. Allard. Microstructural evolution in twin roll cast aa3105 during homogenization. *Materials Science and Engineering: A*, 416(1-2):232–239, 2006. 10, 26, 29

[16] B. Forbord, B. Andersson, F. Ingvaldsen, O. Austevik, J. A. Horst, and I. Skauvik. The formation of surface segregates during twin roll casting of aluminium alloys. *Materials Science and Engineering A*, 415(1-2):12–20, 2006. 28, 31, 32

[17] S. Lokyer, M. Yun, J. D. Hunt, and D. V. Edmonds. Micro- and macrodefects in thin sheet twin-roll cast aluminium alloys. *Materials Characterization*, 37:301–310, 1996. 31

[18] M. A. Cruchaga, D. J. Celentano, and R. W. Lewis. Modelling of twin-roll strip casting processes. *Communications in Numerical Methods in Engineering*, 19(8):623–635, 2003. 10, 32, 33

[19] P. J. Bradbury and J. D. Hunt. A coupled fluid flow, deformation and heat transfer model for a twin roll caster. In M. Cross and J. Campbell, editors, *Modelling of Casting, Welding and Advanced Solidification Processes VII*, pages 739–746. The Minerals, Metals and Materials Society, 1995. 32, 104

[20] H. Bart-Smith, A. F. Bastawros, D. R. Mumm, A. G. Evans, D. J. Sypeck, and H. N. G. Wadley. Compressive deformation and yielding mechanisms in cellular al alloys determined using x-ray tomography and surface strain mapping. *Acta Materialia*, 46(10):3583–3592, 1998. 11, 34, 46, 47, 50, 53, 58

[21] Q. Han and J. D. Hunt. Numerical modelling of the growth of a cellular/dendritic array in multi-component alloys. *Materials Science and Engineering A*, 238(1):192–195, 1997.

[22] W. Kurz and D. J. Fisher. *Fundamentals of Solidification*. Trans Tech Publications, 4th edition, 1998. 34

[23] R. C. Atwood, S. Sridhar, W. Zhang, and P. D. Lee. Diffusion-controlled growth of hydrogen pores in aluminium-silicon castings: in situ observation and modelling. *Acta Materialia*, 48:405–417, 2000. 109

[24] W. Kurz, C. Bezencon, and M. Gaumann. Columnar to equiaxed transition in solidification processing. *Science and Technology of Advanced Materials*, 2:185–191, 2001.

[25] H. B. Dong and P. D. Lee. Simulation of the columnar-to-equiaxed transition in directionally solidified al-cu alloys. *Acta Materialia*, 53(3):659–668, 2005.

[26] R. Mendoza, K. Thornton, I. Savin, and P. W. Voorhees. The evolution of interfacial topology during coarsening. *Acta Materialia*, 54(3):743–750, 2006.

[27] O. Grong, A. K. Dahle, M. I. OnsOien, and L. Arnberg. Analytical modelling of equiaxed solidification. *Acta Materialia*, 46(14):5045–5052, 1998. 34

[28] H. Darcy. *Les Fontaines Publiques de la Ville de Dijon*, 1856. 34, 38

[29] J. Campbell. Feeding mechanisms in castings. *AFFFS Cast Metals Research Journal*, 5(1):1–8, 1969. 44

[30] R. Mehrabian, M. Keane, and M. C. Flemings. Interdendritic fluid flow and macrosegregation; influence of gravity. *Metallurgical and Materials Transactions B*, 1:1209–1220, 1970.

[31] M. C. Flemings. *Solidification Processing*. McGraw-Hill, Inc., New York, 1974. 44

[32] T. D. Papathanasiou. A structure-oriented micromechanical model for viscous flow through square arrays of fibre clusters. *Fibre Science and Technology*, 56(9):1055, 1996. 35

[33] T. D. Papathanasiou and P. D. Lee. Morphological effects on the transverse permeability of arrays of aligned fibers. *Polymer Composites*, 18(2):242–253, 1997. 34, 35, 37

[34] D. Bernard, O. Nielsen, L. Salvo, and P. Cloetens. Permeability assessment by 3d interdendritic flow simulations on microtomography mappings of al-cu alloys. *Materials Science and Engineering A*, 392(1-2):112–120, 2005. 11, 16, 34, 37, 41, 42, 43, 53, 58, 68, 76, 77, 90

[35] J. C. Ramirez and C. Beckermann. Evaluation of a rayleigh-number-based freckle criterion for pb-sn alloys and ni-base superalloys. *Metallurgical and Materials Transactions B-Process Metallurgy and Materials Processing Science*, 34(7):1525, 2003. 35

[36] E. L. Ritman. Micro-computed tomography-current status and developments. *Annual Review of Biomedical Engineering*, 6:185–208, 2004. 34, 55

[37] O. Nielsen, L. Arnberg, A. Mo, and H. Thevik. Experimental determination of mushy zone permeability in aluminium-copper alloys with equiaxed structures. *Metallurgical and Materials Transactions A*, 30A:2455–2462, 1999. 10, 16, 35, 36, 43, 58, 76, 77

[38] A. J. Duncan. Measurement of liquid permeability in the mushy zones of aluminum-copper alloys. *Metallurgical and Materials Transactions B-Process Metallurgy and Materials Processing Science*, 30(4):745, 1999. 58

[39] S. Ganesan, C. L. Chan, and D. R. Poirier. Permeability for flow parallel to primary dendritic arms. *Materials Science and Engineering A*, 151:97–105, 1992. 36, 38, 58

[40] O. Nielsen and L. Arnberg. Experimental difficulties associated with permeability measurements in aluminium alloys. *Metallurgical and Materials Transactions A*, 31A:3149–3153, 2000.

[41] K. Murakami, T. Fujiyama, A. Koike, and T. Okamoto. Influence of melt flow on the growth directions of columnar grains and columnar dendrites. *Acta Metallurgica*, 31:1425–1432, 1983.

[42] K. Murakami and T. Okamoto. Fluid flow in the mushy zone composed of granular grains. *Acta Metallurgica*, 32(10):1741–1744, 1984.

[43] K. Murakami, A. Shiraishi, and T. Okamoto. Interdendritic fluid flow normal to primary dendrite-arms in cubic alloys. *Acta Metallurgica*, 31(9):1417–1424, 1983.

[44] K. Murakami, A. Shiraishi, and T. Okamoto. Fluid flow in interdendritic space in cubic alloys. *Acta Metallurgica*, 32(9):1423–1428, 1984.

[45] N. Streat and F. Weinberg. Interdendritic fluid flow in a lead-tin alloy. *Metallurgical and Materials Transactions B*, 1976. 35, 58

[46] D. R. Poirier. Permeability for flow of interdendritic liquid in columnar-dendritic alloys. *Metallurgical Transactions B*, 18B(March):245–255, 1987. 10, 36, 38, 39, 58, 76, 77

[47] Q. Han. Permeability measurements of the flow of interdendritic liquid in equiaxed aluminum-silicon alloys. *Metallurgical and Materials Transactions B-Process Metallurgy and Materials Processing Science*, 34(1):25, 2003. 36, 58

[48] M. S. Bhat, D. R. Poirier, and J. C. Heinrich. Permeability for cross flow through columnar-dendritic alloys. *Metallurgical and Materials Transactions B*, 26(October):1049–1056, 1995. 37, 40

[49] S. G. R. Brown, J. A. Spittle, D. J. Jarvis, and R. Walden-Bevan. Numerical determination of liquid flow permeabilities for equiaxed dendritic structures. *Acta Materialia*, 50(6):1559–1569, 2002. 37, 38, 39

[50] F. Renard, D. Bernard, X. Thibault, and E. Boller. Synchrotron 3d microtomography of halite aggregates during experimental pressure solution creep and evolution of the permeability. *Geophysical Research Letters*, 31:L07607, 2004. 37, 53, 58

[51] R. G. Santos and M. L. N. M. Melo. Permeability of interdendritic channels. *Materials Science and Engineering A*, 391(1-2):151–158, 2005. 11, 40, 41

[52] P. Wisniewski and H. D. Brody. Microstructural characterization of interdendritic liquid channels. *Materials Science and Engineering A*, 165(1):45–49, 1993. 40

[53] L. Yuan, P. D. Lee, G. Djambazov, and K. Pericleous. Three dimensional simulation of the influence of convection on dendritic solidification. In *Submitted to Modelling of Casting, Welding and Solidification Processes*, 2009. 40

[54] Y. Anguy, D. Bernard, and R. Ehrlich. The local change of scale method for modelling flow in natural porous media (i): Numerical tools. *Advances in Water Resources*, 17(6):337–351, 1994. 41

[55] H.-J. Diepers, C. Beckermann, and I. Steinbach. Simulation of convection and ripening in a binary alloy mush using the phase-field method. *Acta Materialia*, 47(13):3663–3678, 1999. 43

[56] W. O. Dijkstra, C. Vuik, and L. Katgerman. Network model of fluid flow in semi-solid aluminum alloys. *Computational Materials Science*, 38(1):67–74, 2006. 43

[57] A. Daerr and S. Douady. Two types of avalanche behaviour in granular media. *Nature*, 399(6733):241–243, 1999. 11, 44, 45, 108

[58] M. S. Paterson. A granular flow theory for the deformation of partially molten rock. *Tectonophysics*, 335(1-2):51–61, 2001.

[59] C. Marone and B. Kilgore. Scaling of the critical slip distance for seismic faulting with shear strain in fault zones. *Nature*, 362(6421):618–621, 1993.

[60] P. A. Langston, U. Tüzün, and D. M. Heyes. Discrete element simulation of granular flow in 2d and 3d hoppers: Dependence of discharge rate and wall stress on particle interactions. *Chemical Engineering Science*, 50(6):967–987, 1995. 44

[61] D. R. Scott. Seismicity and stress rotation in a granular model of the brittle crust. *Nature*, 381(6583):592–595, 1996. 44

[62] C. L. Martin. Materials science: Alloys go with the grain. *Nature*, 445(7123):34–35, 2007. 44, 108

[63] C. M. Gourlay and A. K. Dahle. Dilatant shear bands in solidifying metals. *Nature*, 445(7123):70, 2007. 11, 44, 46

[64] M. C. Flemings. Behavior of metal alloys in the semisolid state. *Metallurgical and Materials Transactions B-Process Metallurgy and Materials Processing Science*, 22(3):269–293, 1991. 44, 100

[65] A. K. Dahle and L. Arnberg. Development of strength in solidifying aluminium alloys. *Acta Materialia*, 45(2):547–559, 1997. 44, 52, 98

[66] L. Arnberg, G. Chai, and L. Backerud. Determination of dendritic coherency in solidifying melts by rheological measurements. *Materials Science and Engineering A*, 173:101–103, 1993. 44

[67] J. Pilling. Mechanical deformation of dendrites by fluid flow. *Metallurgical and Materials Transactions B-Process Metallurgy and Materials Processing Science*, 27:229, 1996. 44, 49

[68] D. Fuloria, P. D. Lee, and D. Bernard. Microtomographic characterization of columnar al-cu dendrites for fluid flow and flow stress determination. *Materials Science and Engineering: A*, 494(1-2):3–9, 2008. 44, 90

[69] M. Rappaz. A new hot-tearing criterion. *Metallurgical and materials transactions. B, Process metallurgy and materials processing science*, 30(2):449, 1999. 44

[70] M. Ferrante and E. R. de Freitas. Rheological behaviour and deformation characteristics of a commercial and a laboratory-cast al-4%cu alloy in the semi-solid state. *Acta Materialia*, 49(18):3839–3847, 2001. 11, 16, 45, 48, 49, 51, 101, 102

[71] W. Wang. Personal communication: High temperature constitutive equation for deformation in trc, 2008. 45, 81

[72] G. E. Dieter. *Mechanical metallurgy*. McGraw-Hill, Singapore, 1988. 45, 103

[73] K. Dragnevski. Mechanical deformation of dendrites by fluid flow during the solidification of undercooled melts. *Acta Materialia*, 50(14):3743–3755, 2002. 48, 52

[74] C. P. Chen. Semi-solid deformation of non-dendritic structures–i. phenomenological behavior. *Acta Materialia*, 45(5):1955, 1997. 48

[75] E. A. Vieira and M. Ferrante. Prediction of rheological behaviour and segregation susceptibility of semi-solid aluminium-silicon alloys by a simple back extrusion test. *Acta Materialia*, 53(20):5379–5386, 2005. 49

[76] D. Raabe, M. Sachtleber, H. Weiland, G. Scheele, and Z. Zhao. Grain-scale micromechanics of polycrystal surfaces during plastic straining. *Acta Materialia*, 51(6):1539–1560, 2003. 50

[77] D. Rugg, M. Dixon, and F. P. E. Dunne. Effective structural unit size in titanium alloys. *Journal of Strain Analysis for Engineering Design*, 42(4):269–279, 2007. 50

[78] K. Gall, M. Horstemeyer, D. L. McDowell, and J. Fan. Finite element analysis of the stress distributions near damaged si particle clusters in cast al-si alloys. *Mechanics of materials*, 32(5):277, 2000. 50

[79] F. P. E. Dunne, R. Allen, and S. Godfrey. Consolidation of locally reinforced composite shafts using multiscale modelling. *Journal of Strain Analysis for Engineering Design*, 42(4):201–213, 2007. 50

[80] J. Carmai, K. H. Baik, F. P. E. Dunne, P. S. Grant, and B. Cantor. Interface effects during consolidation in titanium alloy components locally reinforced with matrix-coated fibre composite. *Acta Materialia*, 50(20):4981–4993, 2002. 50

[81] I. G. Watson, P. D. Lee, R. J. Dashwood, and P. G. Young. Simulation of the mechanical properties of an aluminum matrix composite using x-ray microtomography. *Metallurgical and Materials Transactions A*, 37A(March):551–558, 2006. 11, 12, 50, 51, 52, 70, 71

[82] R. C. Atwood and P. D. Lee. Simulation of the three-dimensional morphology of solidification porosity in an aluminiumsilicon alloy. *Acta Materialia*, (51):54475466, 2003. 53

[83] R. W. Hamilton, M. F. Forster, R. J. Dashwood, and P. D. Lee. Application of x-ray tomography to quantify the distribution of tib2 particulate in aluminium. *Scripta Materialia*, 46:25–29, 2002. 53, 58

[84] R. A. Ketcham and W. D. Carlson. Acquisition, optimization and interpretation of x-ray computed tomographic imagery: applications to the geosciences. *Computers and Geosciences*, 27(4):381–400, 2001. 55

[85] P. D. Alonso, A. C. Milner, R. A. Ketcham, M. J. Cookson, and T. B. Rowe. The avian nature of the brain and inner ear of archaeopteryx. *Nature*, 430(7000):666–9, 2004. 50

[86] K. T. Conlon and D. S. Wilkinson. Effect of particle distribution on deformation and damage of two-phase alloys. *Materials Science and Engineering A*, 317(1-2):108–114, 2001. 50, 53

[87] N. Chawla, V. V. Ganesh, and B. Wunsch. Three-dimensional (3d) microstructure visualization and finite element modeling of the mechanical behavior of sic particle reinforced aluminum composites. *Scripta Materialia*, 51(2):161–165, 2004. 52

[88] Y. X. Gao, J. Z. Yi, P. D. Lee, and T. C. Lindley. A micro-cell model of the effect of microstructure and defects on fatigue resistance in cast aluminum alloys. *Acta Materialia*, 52(19):5435–5449, 2004.

[89] S. Youssef, E. Maire, and R. Gaertner. Finite element modelling of the actual structure of cellular materials determined by x-ray tomography. *Acta Materialia*, 53(3):719–730, 2005. 50

[90] S. Ghosh. Voronoi cell finite elements. *Computers and Structures*, 50(1):33, 1994. 51

[91] S. Ghosh, K. Lee, and S. Moorthy. Multiple scale analysis of heterogeneous elastic structures using homogenization theory and voronoi cell finite element method. *International Journal of Solids and Structures*, 32(1):27–62, 1995.

[92] V. Mathier, A. Jacot, and M. Rappaz. Coalescence of equiaxed grains during solidification. *Modelling and Simulation in Materials Science and Engineering*, 12:479–490, 2004. 97

[93] S. Vernède and M. Rappaz. A simple and efficient model for mesoscale solidification simulation of globular grain structures. *Acta Materialia*, 55(5):1703–1710, 2007. 51, 52

[94] A. B. Phillion, S. L. Cockcroft, and P. D. Lee. A three-phase simulation of the effect of microstructural features on semi-solid tensile deformation. *Acta Materialia*, 56(16):4328–4338, 2008. 51, 108

[95] E. Tzimas and A. Zavaliangos. Mechanical behavior of alloys with equiaxed microstructure in the semisolid state at high solid content. *Acta Materialia*, 47(2):517–528, 1999. 16, 51, 101, 102

[96] T. G. Nguyen, D. Favier, and M. Suery. Theoretical and experimental study of the isothermal mechanical behaviour of alloys in the semi-solid state. *International Journal of Plasticity*, 10(6):663–693, 1994.

[97] A. Zavaliangos. Modeling of the mechanical behaviour of semisolid metallic alloys at high volume fractions of solid. *International Journal of Mechanical Sciences*, 40(10):1029–1041, 1998. 51

[98] O. Ludwig, J. M. Drezet, C. L. Martin, and M. Suéry. Rheological behavior of al-cu alloys during solidification constitutive modeling, experimental identification, and numerical study. *Metallurgical and Materials Transactions A*, 36(6):1525–1535, 2005. 52

[99] C. L. Martin, D. Favier, and M. Suéry. Viscoplastic behaviour of porous metallic materials saturated with liquid part i: Constitutive equations. *International Journal of Plasticity*, 13(3):215–235, 1997.

[100] C. L. Martin, D. Favier, and M. Suéry. Fracture behaviour in tension of viscoplastic porous metallic materials saturated with liquid. *International Journal of Plasticity*, 15(10):981–1008, 1999. 52

[101] O. Ludwig, J. M. Drezet, P. Ménésès, C. L. Martin, and M. Suéry. Rheological behavior of a commercial aa5182 aluminum alloy during solidification. *Materials Science and Engineering: A*, 413-414:174–179, 2005. 52

[102] M. MHamdi, A. Mo, and C. Martin. Two-phase modeling directed toward hot tearing formation in aluminum direct chill casting. *Metallurgical and Materials Transactions A*, 33(7):2081–2093, 2002. 52

[103] I. Farup and A. Mo. Two-phase modeling of mushy zone parameters associated with hot tearing. *Metallurgical and Materials Transactions A*, 31(5):1461–1472, 2000. 52

[104] Z. Gronostajski. The constitutive equations for fem analysis. *Journal of Materials Processing Technology*, 106(1-3):40–44, 2000. 52, 92

[105] E. R. de Freitas, E. Ferracini Jr, and M. Ferrante. Microstructure and rheology of an aa2024 aluminium alloy in the semi-solid state, and mechanical properties of a back-extruded part. *Journal of Materials Processing Technology*, 146(2):241–249, 2004. 52

[106] D. J. Lahaie and M. Bouchard. Physical modeling of the deformation mechanisms of semisolid bodies and a mechanical criterion for hot tearing. *Metallurgical and Materials Transactions B*, 32:697–705, 2001.

[107] D. Larouche, J. Langlais, W. Wu, and M. Bouchard. A constitutive model for the tensile deformation of a binary aluminum alloy at high fractions of solid. *Metallurgical and Materials Transactions B*, 37(3):431–443, 2006. 52, 97

[108] I. G. Watson, M. F. Forster, P. D. Lee, R. J. Dashwood, R. W. Hamilton, and A. Chirazi. Investigation of the clustering behaviour of titanium diboride particles in aluminium. *Composites: Part A*, 36:1177–1187, 2005. 52, 53

[109] E. W. J. Miller and J. Beech. In-situ radiographic observations of alloy solidification. *Metallography*, 5(3):298–300, 1972.

[110] J. Alkemper and P. W. Voorhees. Three-dimensional characterization of dendritic microstructures. *Acta Materialia*, 49(5):897–902, 2001.

[111] R. C. Atwood, J. R. Jones, P. D. Lee, and L. L. Hench. Analysis of pore interconnectivity in bioactive glass foams using x-ray microtomography. *Scripta Materialia*, 51(11):1029–1033, 2004. 58

[112] E. Maire, J. Y. Buffière, L. Salvo, J. J. Blandin, W. Ludwig, and J. M. Létang. On the application of x-ray microtomography in the field of materials science. *Advanced Engineering Materials*, 3(8):539–546, 2001.

[113] R. W. Hamilton, D. See, S. Butler, and P. D. Lee. Multiscale modeling for the prediction of casting defects in investment cast aluminum alloys. *Materials Science and Engineering A*, 343:290–300, 2003.

[114] L. Salvo, P. Cloetens, E. Maire, S. Zabler, J. J. Blandin, J. Y. Buffiere, W. Ludwig, E. Boller, D. Bellet, and C. Josserond. X-ray micro-tomography an attractive characterization technique in materials science. *Nuclear Instruments and Methods in Physics Research B*, 200:273–286, 2003. 53, 58, 109

[115] S. R. Stock. X-ray microtomography of materials. *International Materials Reviews*, 44:141–164, 1999. 11, 53, 54

[116] A. C. Kak and M. Slaney. *Principles of Computerized Tomographic Imaging*. Classics in Applied Mathematics. SIAM, New York, 2001. 54, 56

[117] C. M. Edwin. Photon attenuation in computed tomography. *Medical Physics*, 2(6):307–320, 1975. 54

[118] J. H. Hubbell and S. M. Seltzer. Tables of x-ray mass attenuation coefficients and mass energy-absorption coefficients (version 1.4), Mar 2006 2004. 11, 55

[119] D. R. Poirier and S. Ganesan. Permeabilities for flow of interdendritic liquid in equiaxial structures. *Materials Science and Engineering A*, 157:113–123, 1992. 58

[120] N. Iqbal, N. H. v. Dijk, S. E. Offerman, M. P. Moret, L. Katgerman, and G. J. Kearley. Real-time observation of grain nucleation and growth during solidification of aluminium alloys. *Acta Materialia*, 53:2875–2880, 2005. 61

[121] H. N. Thi, H. Jamgotchian, J. Gastaldi, J. Hartwig, T. Schenk, H. Klein, B. Billia, J. Baruchel, and Y. Dabo. Preliminary in situ and real-time study of directional solidification of metallic alloys by x-ray imaging techniques. *Journal of Physics D: Applied Physics*, 36:A83–A86, 2003. 61

[122] B. Goyeau, T. Benihaddadene, D. Gobin, and M. Quintard. Numerical calculation of the permeability in a dendritic mushy zone. *Metallurgical and Materials Transactions B*, 30B(August):613–622, 1999. 68

[123] J. C. Heinrich and D. R. Poirier. Convection modeling in directional solidification. *Comptes Rendus Mecanique*, 332(5-6):429–445, 2004. 74

[124] M. McLean. *Directionally solidified materials for high temperature service*. The Metals Society, London, 1983. 83

[125] N. D'Souza. Directional and single-crystal solidification of ni-base superalloys: Part i. the role of curved isotherms on grain selection. *Metallurgical and Materials Transactions B-Process Metallurgy and Materials Processing Science*, 31(11):2877, 2000. 83

[126] E. J. Garboczi. An algorithm for computing the effective linear elastic properties of heterogeneous materials: Three-dimensional results for composites with equal phase poisson ratios. *Journal of the Mechanics and Physics of Solids*, 43(9):1349, 1995. 84

[127] W. E. Lorensen and H. E. Cline. Marching cubes: A high resolution 3d surface construction algorithm. *Proceedings of the 14th annual conference on Computer graphics and interactive techniques*, pages 163–169, 1987. 85

[128] R. Fureder, T. B. West, V. Bui Xuan, I. Weber, and P. G. Young. On a new technique for generating finite element and rapid prototyped models based on 3d data. *Proceedings of The IASTED International Conference on Biomechanics, Acta Press*, 2003. 85

[129] J. A. Eady and D. M. Smith. The effect of porosity on the tensile propeties of aluminium castings. *Materials Forum*, 9(4):217–223, 1986. 90

[130] D. S. Fields and W. A. Bachofen. *ASTM*, 57:1259, 1957. 92

[131] A. B. Phillion, S. L. Cockcroft, and P. D. Lee. A new methodology for measurement of semi-solid constitutive behavior and its application to examination of as-cast porosity and hot tearing in aluminum alloys. *Materials Science and Engineering: A*, 491(1-2):237–247, 2008. 16, 95, 123, 124, 125

[132] A. B. Phillion. *Hot tearing and constitutive behaviour of semi-solid aluminium alloys*. PhD thesis, The University of British Columbia, 2007. 95

[133] S. Weyer. Automatic finite element meshing of planar voronoi tessellations. *Engineering fracture mechanics*, 69(8):945, 2002. 97

[134] S. Vernède, P. Jarry, and M. Rappaz. A granular model of equiaxed mushy zones: Formation of a coherent solid and localization of feeding. *Acta Materialia*, 54(15):4023–4034, 2006. 97

[135] M. Kiuchi, J. Yanagimoto, and H. Yokobayashi. Flow stress, yield criterion and constitutive equation of mushy/semi -solid alloys. *CIRP Annals - Manufacturing Technology*, 50(1):157–160, 2001. 14, 99, 100

[136] A. A. Tseng, J. Horský, M. Raudenský, and P. Kotrbácek. Deformation behavior of steels in mushy state. *Materials and Design*, 22(2):83–92, 2001. 14, 99, 100

[137] A. H. Clauer and B. A. Wilcox. *Metals Science*, 1:86–90, 1967. 103

[138] O. D. Sherby and P. M. Burke. *Progress in Materials Science*, 13:325–386, 1967. 103

[139] A. B. Phillion, S. L. Cockcroft, and P. D. Lee. X-ray micro-tomographic observations of hot tear damage in an al-mg commercial alloy. *Scripta Materialia*, 55(5):489–492, 2006. 108

[140] J. Campbell and T. W. Clyne. Hot tearing in al-cu alloys. *Cast Metals*, 3(4):224–226, 1991. 108

[141] W. S. Pellini. Strain theory of hot tearing. *Foundry*, pages 125–137, 1952. 109

[142] H. Fredriksson and B. Lehtinen. Continuous observations of hot crack-formation during deformation and heating in a scanning electron microscope. *International Conference of Solidification and Casting, Metals Society, London*, 2(31), 1977. 109

[143] D. Davidson, D. Viano, L. Liming, and D. St.John. Observation of crack initiation during hot tearing. In M. Tiryakioglu and P.N. Crepeau, editors, *Shape Casting: The John Campbell Symposium*, pages 175–182, San Francisco, CA, 2005. TMS. 109

[144] J. B. Mitchell, S. L. Cockcroft, D. Viano, C. J. Davidson, and D. St.John. Determination of strain during hot tearing by image correlation. *Metallurgical and Materials Transactions A*, 38:2503–2512, 2007. 109

[145] I. Farup, M. Rappaz, and J. M. Drezet. In-situ observation of hot tearing formation in succinonitrile-acetone. *Acta Materialia(USA)*, 49(7):1261–1269, 2001. 109

[146] D. Stegemann, W. Reimche, and J. Schmidbauer. Investigation of light metal casting processes by real time microfocus radioscopy. *European Journal of Nondestructive Testing*, 1(3):107–117, 1992. 109

[147] O. Ludwig, M. Dimichiel, L. Salvo, M. Suéry, and P. Falus. In-situ three-dimensional microstructural investigation of solidification of an al-cu alloy by ultrafast x-ray microtomography. *Metallurgical and Materials Transactions A*, 36(6):1515–1523, 2005.

[148] R. H. Mathiesen and L. Arnberg. X-ray radiography observations of columnar dendritic growth and constitutional undercooling in an al-30wt%cu alloy. *Acta Materialia*, 53(4):947–956, 2005. 109